Selectivity and competition between the anodic evolution of oxygen and chlorine

Vos, J.G.

9 SUPPORTING INFORMATION

This chapter contains all supplementary information for the work presented in this thesis. All subsections are numbered according to chapter numbers (i.e. the supporting information for Chapter 2 is found in section 9.2).

9.1. General experimental information

9.1.1. Synthesis of hydrated IrO_x nanoparticles

Hydrated IrO_x nanoparticles were prepared and used as a meta-stable IrO_x colloid suspension obtained from alkaline hydrolysis of $Ir[Cl]_6^{3-}$.[142,143,262,347] Briefly, $Na_2IrCl_6 \cdot 6H_2O$ was dissolved in 0.1 M NaOH to reach a nominal Ir concentration of 2 mM. Dissolution of the complex was followed by aqueous reduction of $Ir[Cl]_6^{2-}$ to $Ir[Cl]_6^{3-}$, coupled to momentary O_2 gas formation on the solid.[348] The light yellow solution was then heated in a water bath to either 70 °C or 95 °C and kept there for 20 minutes, under continuous stirring. The solution turned very light blue during this period. It was subsequently transferred to an ice bath and 60% $HClO_4$ was added under stirring, until the solution pH was approximately 1. The solution colour turned dark violet after acid addition. It was stirred in the ice bath for 1 h, allowing condensation of hydrated IrO_x colloids. The solution could then be used immediately for experiments. For long term storage, the solution was made alkaline (pH ≈ 13) by addition of 10.1 M NaOH, causing a subtle colour shift from violet to dark purple. It could be stored for up to 3 months at 4 °C.

9.1.2. Preparation of GC-supported hydrated IrO_x films (IrO_x/GC)

GC disks (Pine Research Instrumentation, surface area 0.196 cm²) were prepared to a mirror finish by hand polishing with either Al_2O_3 or diamond pastes down to 0.05 μm particle size, followed by rinsing and sonication of the electrode in water for 3 minutes.

To prepare the IrO_x/GC electrode, the IrO_x particles were electroflocculated on the GC surface under rotation. A 4 mL aliquot of the bulk alkaline solution was re-acidified with 60% $HClO_4$ down to pH ≈ 1.5. The removal of OH^- induced the deprotection of the IrO_x colloids, which manifested as a solution color change from purple to greyish violet. Care must be taken not to make the IrO_x solution too acidic, since competing CER at low pH may interfere with the reproducibility of the deposition. CER originates from the Cl^- which is present as byproduct from the $Ir[Cl]_6^{3-}$ hydrolysis. Deposition was then performed at a rotation rate of 600 RPM on a freshly prepared GC surface. The disk electrode was first scanned between 5-10 cycles at 250 mV s^{-1} in range of 0.16 - 1.36 V vs. Ag/AgCl, to observe the initial IrO_x deposition and the onset of the mixed OER and CER. Their activities increased with each scan as progressively more IrO_x deposited. The scans were followed by amperometry for 300 - 600 s (depending on the desired thickness) at a potential roughly 10-20 mV positive of the onset of the mixed OER and CER. Currents rising over time indicated further IrO_x deposition. After deposition, a reflective blue film was visible on the GC surface.

9.2. Supporting information for Chapter 2

9.2.1. Supplementary figures

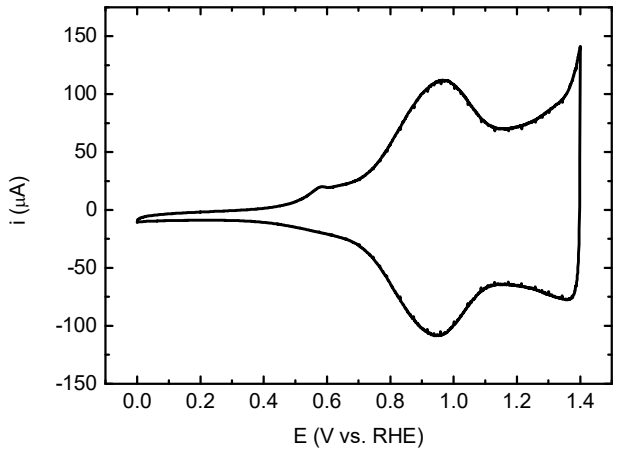

Figure A 9.2.1: Characterization CV of the electroflocculated IrO_x catalyst, in 0.5 M $KHSO_4$. Scan rate: 50 mV s^{-1}.

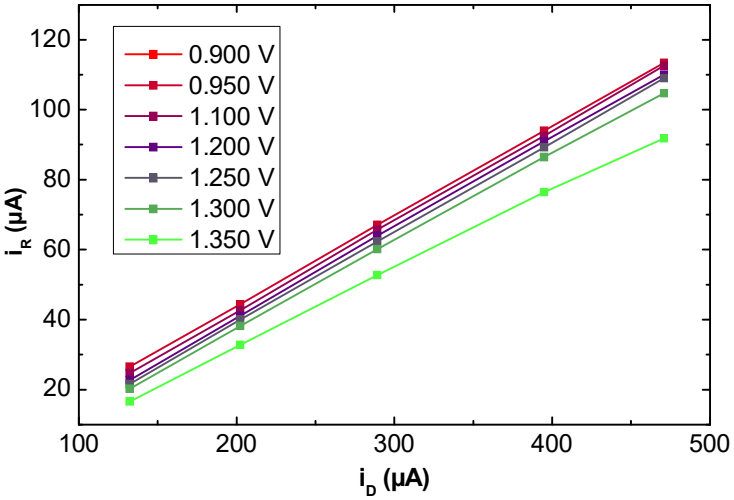

Figure A 9.2.2: Behavior of i_R vs. i_D at various ring potentials, data taken from Figure 2. Example plot for $[Cl^-] = 100$ mM used to find potential dependent slopes, which are equivalent to N_{Cl_2}.

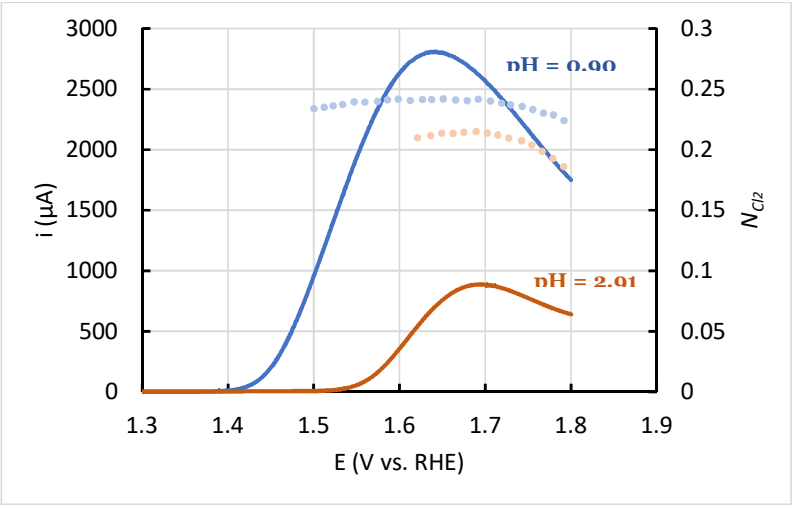

Figure A 9.2.3: Linear sweep voltammograms (10 mV/s) of the disk electrode in a Pt-Pt RRDE setup, in 0.5 M $KHSO_4$ solutions of pH = 0.90 (blue) and pH = 2.91 (orange). $[Cl^-]$ = 20 mM, rotation rate = 1500 RPM. Ring currents were collected at 0.95 V vs. RHE. Dotted symbols show corresponding values of the apparent chlorine collection factor N_{Cl_2}, equivalent to $|i_R/i_D|$. Since OER onsets around 1.65 V on Pt in acidic conditions, N_{Cl_2} should approach the liquid phase collection factor close before this onset, where approximately all current can be ascribed to CER.

Formation of PtO_x has a strong inhibitory effect on CER kinetics, as was previously reported by Conway and Novák (see ref. 19). The CER current rises but then decreases with increasing potentials despite hydrodynamic conditions. N_{Cl_2} reaches an approximately constant value as function of increasing E_D in both experiments. It decreases above $E_D \approx 1.65$ V, which can be ascribed to the onset of parallel OER.

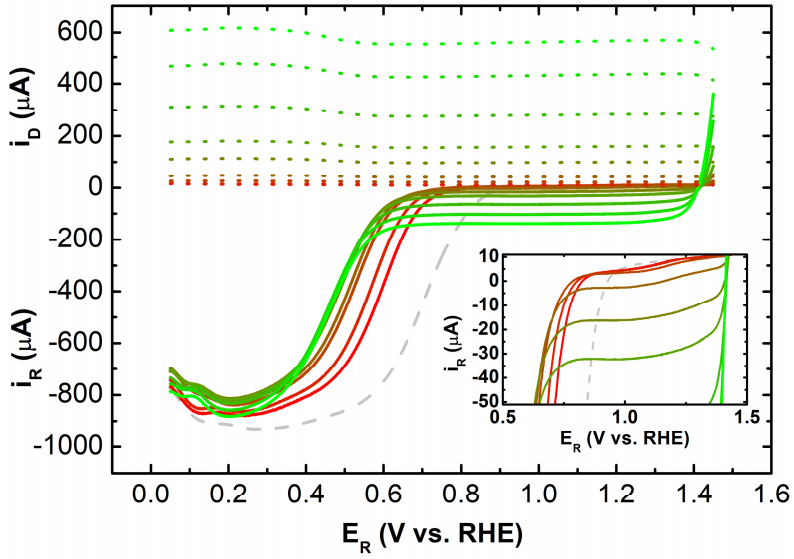

Figure A 9.2.4: LSV of the Pt ring electrode while keeping the IrO_x/GC disk electrode fixed at 1.475 V, in 0.5 M $KHSO_4$. $[Cl^-]$ (in the form of KCl) increasing from 1 (red) to 100 mM (green). Dotted curves with positive values correspond to disk currents, remaining curves correspond to ring currents. Inset shows enlarged CRR region at low $[Cl^-]$. The ring LSV sweeps were taken in the anodic direction. Scan rate 5 mV s^{-1}, rotation rate 1500 RPM, pH = 0.88, solution saturated with O_2.

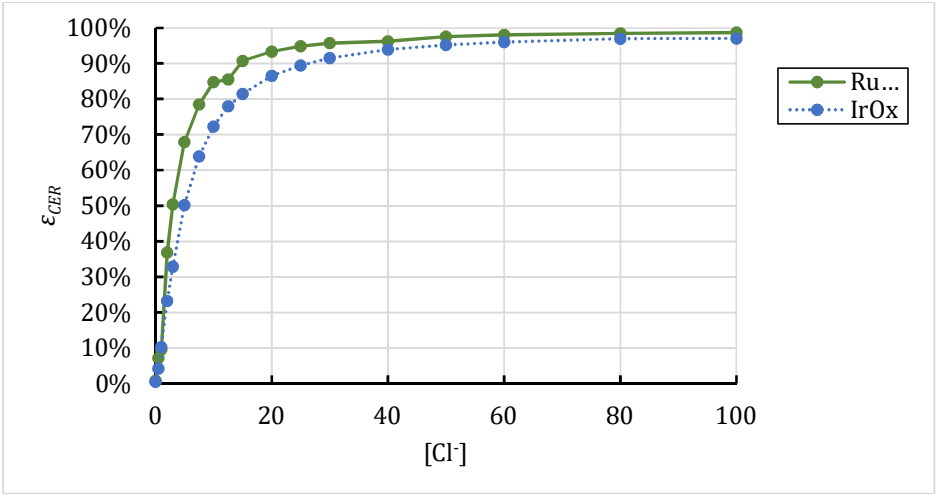

Figure A 9.2.5: ε_{CER} vs. $[Cl^-]$ curve at E_D = 1.530 V vs. RHE for dropcasted RuO_2 (Sigma-Aldrich) versus the electroflocculated IrO_x catalyst, in 0.5 M $KHSO_4$ and increasing amounts of KCl, at 1500 RPM. The RuO_2 was dropcasted on the GC support from a 1 mg/mL suspension in EtOH, and air dried while rotating at 200 RPM. Final catalyst loading ~ 100 µg * cm^{-2}.

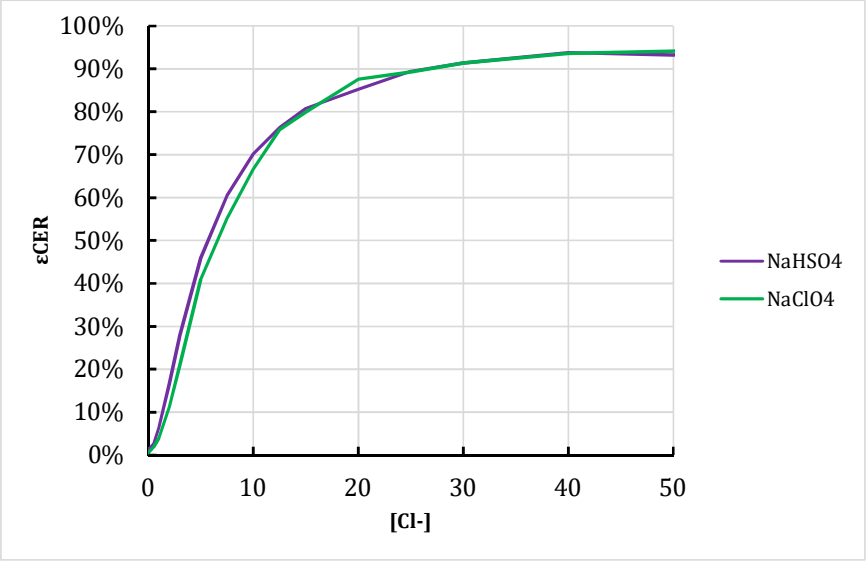

Figure A 9.2.6: ε_{CER} vs. $[Cl^-]$ on electroflocculated IrO_x, in a 0.5 M $NaHSO_4$ solution of pH 0.804 (purple curve) and a 0.5 M $NaClO_4$ + $HClO_4$ solution of pH 0.776 (green curve). Disk potential: ED = 1.530 V, 1500 RPM.

9.3. Supporting information for Chapter 3

9.3.1. Estimation of error due to Ir dissolution and redeposition during RRDE experiments

In the following, we will describe the estimation of error in the ring response caused by Ir-related dissolution during RRDE experiments. It is assumed that there are two sources of error:

- Stray ring currents due to the reduction of higher-oxidized, transiently dissolved Ir^{x+} species;
- Errors in Cl_2 detection due to a slowing-down of the chlorine reduction reaction (CRR) after the deposition of IrO_x on the ring.

It must be noted that the latter error may in fact be vanishingly small, since prior experiments (not shown) indicated that the CRR also progresses rapidly on IrO_x. The reaction, like its CER counterpart, seems kinetically quite facile on metal oxides.[135,349] Nonetheless, the possible error will be considered for the sake of completeness.

From ICP-MS data, we assume that during vigorous OER and/or CER, Ir dissolves at an average rate of 1 ng cm^{-2} s^{-1} (see Figure 3.1 in the main text). For stray reduction currents on the ring, we assume that Ir in the form of the unknown Ir^{x+} species has a valency of +6, such as in the case of gaseous IrO_3 or soluble IrO_4^{2-},[161] and that its primary reduction reaction at 0.95 V vs. RHE is 2-electron in nature. The stray reduction current density on the ring can then be estimated as:

$$j = 10^{-3}\ \mu g\ Ir\ cm^{-2}\ s^{-1} * \frac{2F}{M_{Ir}} * N \approx 0.25\ \mu A\ cm^{-2} \qquad \text{Eq. A 9.3.1}$$

where $M_{Ir} = 192.22\ \mu g\ Ir/\mu mol\ Ir$ is the molar mass of Ir, $N \approx 0.25$ is the collection factor, and $F = 96485\ \mu C/\mu mol\ Ir$. This current density is orders of magnitude lower than typical experimental results and can thus be safely neglected.

Concerning IrO_x deposition on the ring, we assume that Ir^{x+} species deposit as crystalline, rutile-type IrO_2, and determine the minimum time required to form a perfect monolayer of IrO_2 on an ideal, ring-sized flat surface. This minimum time is:

$$t = \frac{1}{N}\frac{A_R}{A_D} * \frac{\rho_{IrO_2,m} * d_{IrO_2}}{10^{-3}\ \mu g\ Ir\ cm^{-2}\ s^{-1}} * \frac{10^6\ \mu g}{1\ g} * M_{Ir} \approx 670\ s \qquad \text{Eq. A 9.3.2}$$

This equation represents the amount of mol IrO_2 in a perfect monolayer on the ring surface divided by the molar rate of Ir deposition per surface area, which is the Ir dissolution on the disk corrected by N. $A_R = \pi\left[\left(\frac{0.75\ cm}{2}\right)^2 - \left(\frac{0.65\ cm}{2}\right)^2\right] \approx 0.11\ cm^2$ is the ring geometric surface area, $A_D = 0.196\ cm^2$ is the disk surface area, $\rho_{IrO_2,m} = \frac{\rho_{IrO_2}}{M_{IrO_2}} = \frac{11.66\ g\ cm^{-3}}{224.22\ g\ mol^{-1}}$ is the molar density of rutile IrO_2, and $d_{IrO_2} \approx 3 * 10^{-8}$ cm is the estimated thickness of a monolayer rutile IrO_2, which was arbitrarily chosen as the c-direction (in the a-direction, $d_{IrO_2} \approx 5 * 10^{-8}$ cm, which would lead to even longer deposition times). This deposition time represents the absolute worst-case scenario for IrO_x, and is by itself at least an order of magnitude higher than the typical duration of a session of experiments. This suggests that interference with the CRR on the ring by stray IrO_x deposition is not an issue.

9.3.2. Supplementary ICP-MS data

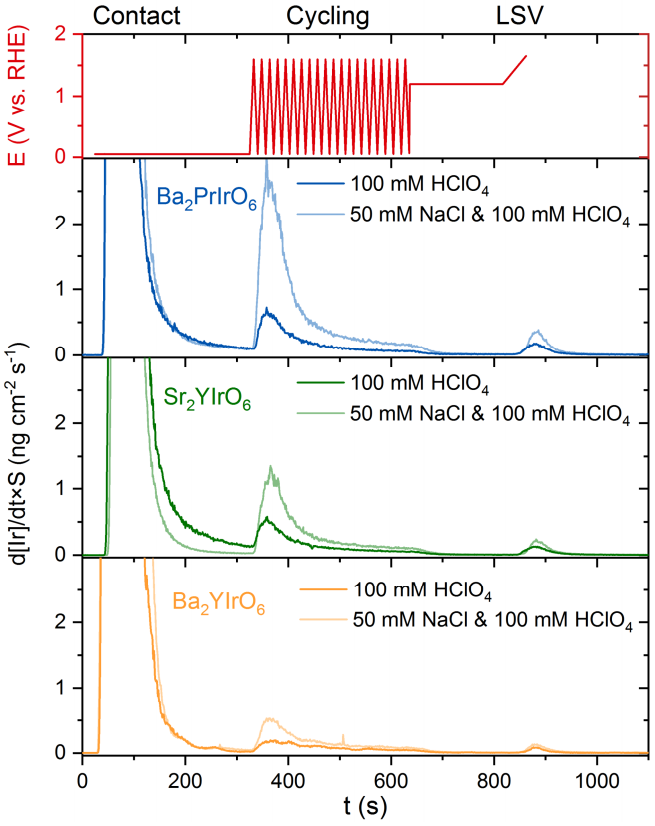

Figure A 9.3.1: ICP-MS measurements shown in Figure 3.1, including the initial contact peak.

Table A 9.3.1: Catalyst spot sizes (in cm^2) and loadings during ICP measurements.

	0.1 M $HClO_4$	0.1 M $HClO_4$ + 50 mM NaCl
Ba_2PrIrO_6	0.009 (9.00 µg/cm^2)	0.011 (7.36 µg/cm^2)
Ba_2PrIrO_6 with Nafion	0.015 (5.4 µg/cm^2)	0.010 (8.1 µg/cm^2)
Sr_2YIrO_6	0.012 (6.75 µg/cm^2)	0.013 (6.23 µg/cm^2)
Ba_2YIrO_6	0.010 (8.1 µg/cm^2)	0.013 (6.23 µg/cm^2)
Ba_2CeIrO_6	0.010 (8.1 µg/cm^2)	0.014 (8.79 µg/cm^2)

Table A 9.3.2: Total dissolved amounts (TDA) of all elements after the ICP-MS experiments (in ng cm^{-2}).

Perovskite (A_2BIrO_6)	**Electrolyte**	**Contact dissolution**			**Cycling dissolution**			**LSV dissolution**			**S-Number**
		A	**B**	**Ir**	**A**	**B**	**Ir**	**A**	**B**	**Ir**	**N_{gas}/N_{Ir}**
Ba_2PrIrO_6	0.1 M $HClO_4$	1681	1134	1612	0	0	43	2	0	8	2285
	0.1 M $HClO_4$ + 50 mM NaCl	1284	965	2036	0	1	196	0	0	16	1196
Ba_2PrIrO_6 (without Nafion)	0.1 M $HClO_4$	272	361	1263	0	1	17.6	0	0	1.5	4067
	0.1 M $HClO_4$ + 50 mM NaCl	719	662	2215	0	0	23.4	0	0	3.6	2142.5
Sr_2YIrO_6	0.1 M $HClO_4$	1102	950	1577	3	0	28	0	0	6	3782
	0.1 M $HClO_4$ + 50 mM NaCl	896	673	1189	1	0	102	0	0	9	1610
Ba_2YIrO_6	0.1 M $HClO_4$	454	473	1478	0	0	24.7	0	0	2.9	3528
	0.1 M $HClO_4$ + 50 mM NaCl	641	623	2252	0	0	49.7	0	0	5	1883
Ba_2CeIrO_6	0.1 M $HClO_4$	645	385	1840	0	0	0	0	0	0	n.a.
	0.1 M $HClO_4$ + 50 mM NaCl	1580	1408	4409	0	0	21.6	0	0	4	2115

$$S = \frac{n(\text{Gas})}{n(\text{Ir})} = \frac{n(O_2+Cl_2)}{n(\text{Ir})} = \frac{\left[\frac{\int I\,dt}{4 \times F}\right] \times Y_{O_2} + \left[\frac{\int I\,dt}{2 \times F}\right] \times Y_{Cl_2}}{\frac{m(\text{Ir})}{M(\text{Ir})}} \qquad \text{Eq. A 9.3.3}$$

Eq. A 9.3.3 was used for calculating the S-number. Here the moles of evolved gas, $n(\text{Gas})$, is comprised of $\int I\,dt$ as the charge passed during the LSV, F as Faraday's constant, Y_{O_2} and Y_{Cl_2} as the fractional yields of the OER and CER respectively, taken from RRDE experiments in presence of 50 mM NaCl. The dissolved moles of iridium, $n(\text{Ir})$, is calculated from the mass dissolved, $m(\text{Ir})$, and its molar weight $M(\text{Ir})$.

9.3.3. Supplementary XRD and RRDE data

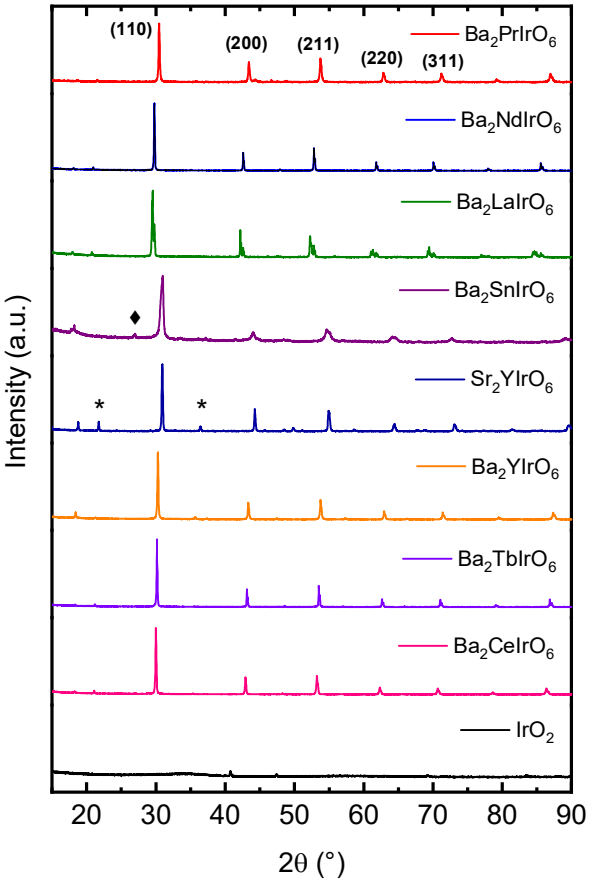

Figure A 9.3.2: X-ray powder diffraction patterns of the iridium-based double perovskites used in this study, together with the commercial IrO_2 reference. Strong lines are characteristic of the primitive perovskite and the indexing of some of these reflections is given. Some visible superlattice reflections are marked by *. Note that in Ba_2SnIrO_6, a small contamination from $BaIrO_3$ is also visible (marked by ♦).

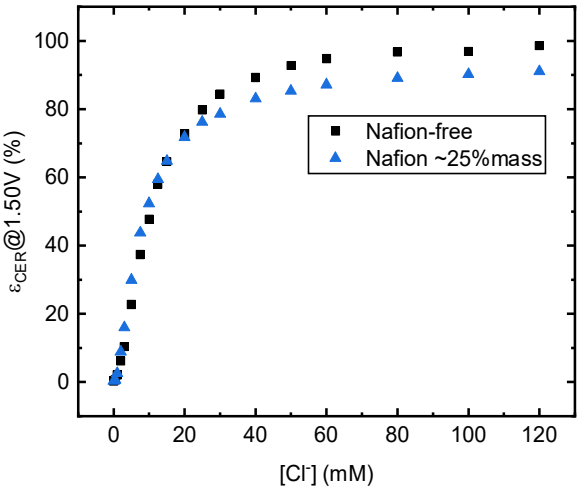

Figure A 9.3.3: The effect of Nafion binder on apparent CER selectivity. Shown is the CER selectivity ε_{CER} as a function of $[Cl^-]$ in a solution of 0.1 M $HClO_4$, for Ba_2PrIrO_6 dropcasted from an EtOH suspension (black) and Ba_2PrIrO_6 dropcasted from an EtOH suspension containing 0.23 mg Nafion copolymer per mg Ba_2PrIrO_6. Prior to mixing, the Nafion sulfonate groups were partially Na-exchanged by mixing commercial 5%wt stock solution (purchased from Sigma-Aldrich) with 0.1 M NaOH in a ratio of 2:1. Selectivity values shown at 1.50 V, obtained with the RRDE method as described in the main text.

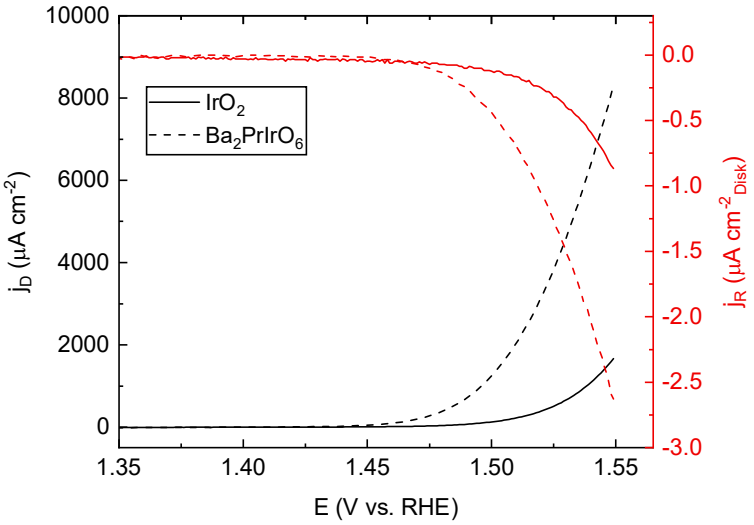

Figure A 9.3.4: The RRDE ring response at 0.95 V during OER in chloride-free conditions. Comparison of disk and ring current densities measured on IrO_2 (solid traces) and Ba_2PrIrO_6 (dotted traces) in 0.1 M $HClO_4$, with the ring fixed at 0.95 V.

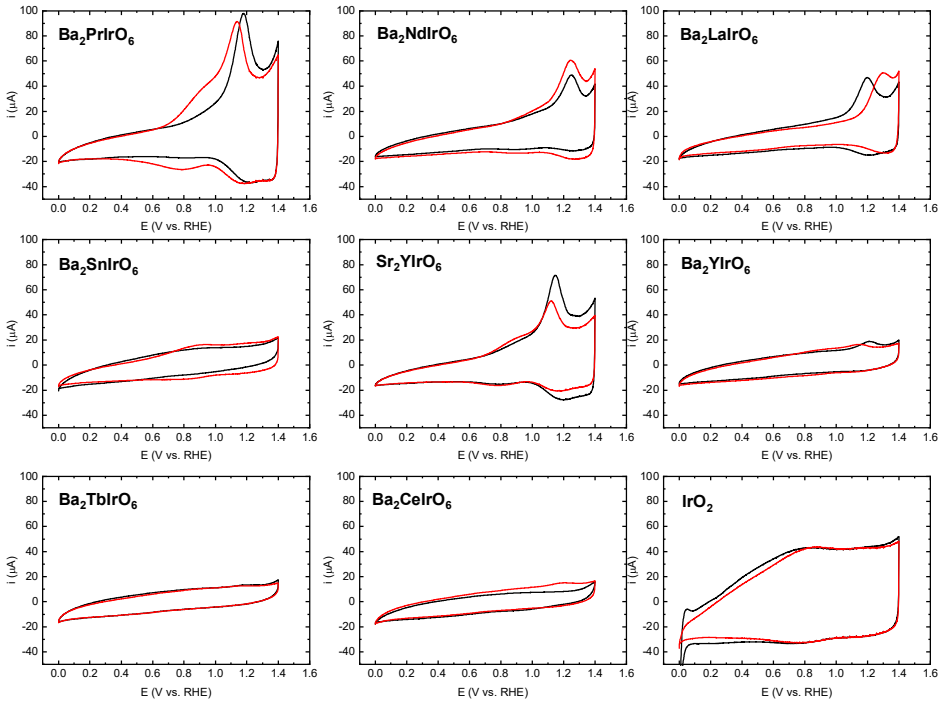

Figure A 9.3.5: The effect of repeated scanning on voltammetric characterizations. Shown are comparisons of blank voltammograms of the GC-supported materials in 0.1 M $HClO_4$. Black curves: 'pristine' state (after contact with the solution at 0.05 V for approximately 30 seconds). Red curves: surfaces after extensive scanning (at least 20 cycles) in the range of 1.30 – 1.55 V at 1500 RPM. Scan rate: 50 mV s^{-1}.

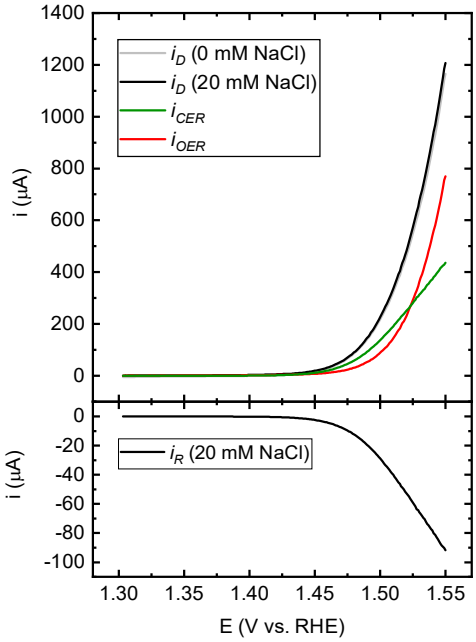

Figure A 9.3.6: Example curve of a RRDE experiment to illustrate the deconvolution of parallel evolution of oxygen and chlorine. Top panel displays disk currents (i_D) measured on a GC-supported Ba_2NdIrO_6 thin film, in a NaCl-free solution of 0.1 M $HClO_4$ (grey curve) and in a solution composed of 0.1 M $HClO_4$ and 20 mM NaCl (black curve). Rotation rate: 1500 RPM. Lower panel shows corresponding currents measured on the Pt ring (i_R) fixed at a potential of 0.95 V in presence of 20 mM NaCl. The calculation of i_{OER} and i_{CER} curves was performed using the ring currents and $N_{Cl_2} = 0.215$, see also Eq. 2.1 and Eq. 2.2.

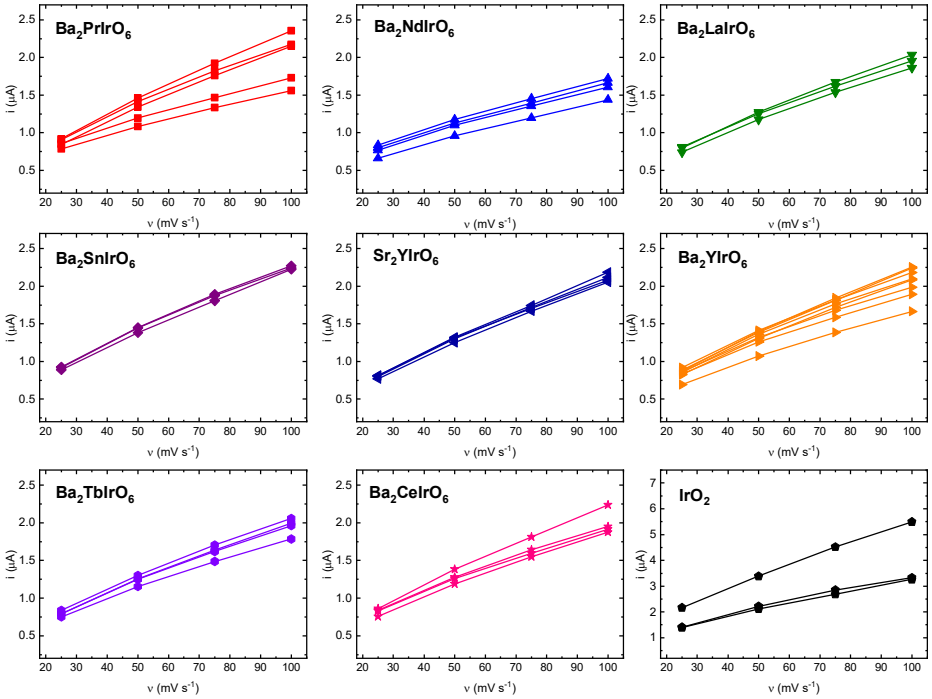

Figure A 9.3.7: Measured currents at 0.1 V as a function of scan rate in the potential region 0.05 – 0.15 V, for all performed RRDE activity experiments. Lines correspond to individual experiments for each material. Note the difference in scale for the IrO_2 experiments.

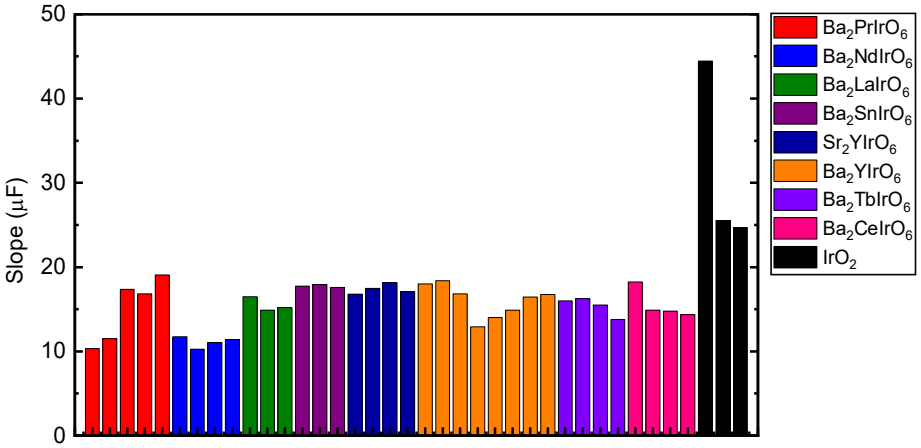

Figure A 9.3.8: Measured values of $(C_{dl})_{0.1\,V}$ for performed RRDE activity experiments on the basis of Figure A 9.3.7. Bars correspond to individual experiments.

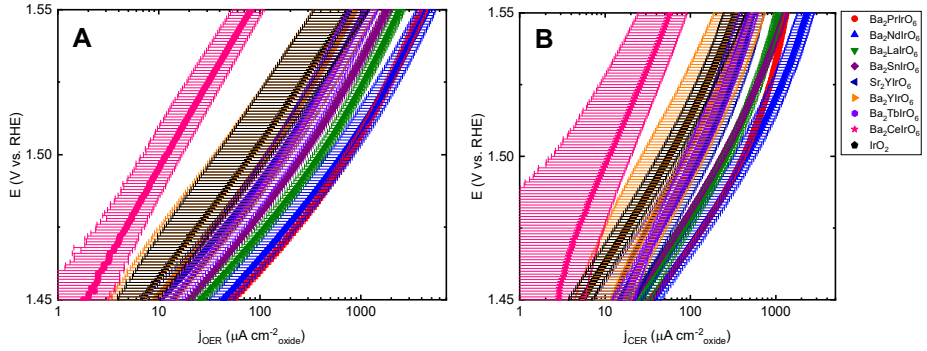

Figure A 9.3.9: Standard deviations in RRDE activity experiments. Shown are OER (A) and CER (B) Tafel curves as in Figure 3.3, including standard deviations around the average values.

Table A 9.3.3: Measured average linear Tafel slopes for OER (in Cl^--free electrolyte and in presence of 20 mM Cl^-) and CER, in potential ranges 1.45 – 1.50 V and 1.50 – 1.55 V. Standard errors of at least three independent measurements (using freshly prepared catalyst films) are indicated. Color scale (bottom) indicates the correlation coefficient, expressing the degree of linearity of each segment; green corresponds to R^2 = 1.000, red corresponds to R^2 = 0.980.

	CER (mV/dec)		OER, [Cl^-] = 0 mM (mV/dec)		OER, [Cl^-] = 20 mM (mV/dec)	
	1.45-1.50 V	1.50-1.55 V	1.45-1.50 V	1.50-1.55 V	1.45-1.50 V	1.50-1.55 V
Ba_2PrIrO_6	45 ± 0.8	90 ± 10	43 ± 0.7	67 ± 1.7	46 ± 2.1	55 ± 1.4
Ba_2NdIrO_6	46 ± 2.8	69 ± 2.1	42 ± 0.4	60 ± 2.1	53 ± 2.0	49 ± 1.2
Ba_2LaIrO_6	49 ± 3.0	82 ± 1.3	42 ± 0.4	64 ± 0.5	47 ± 1.4	53 ± 0.3
Sr_2YIrO_6	52 ± 2.5	80 ± 3.6	42 ± 2.4	59 ± 1.9	50 ± 17	51 ± 2.7
Ba_2SnIrO_6	47 ± 1.2	67 ± 0.4	44 ± 0.4	60 ± 0.4	65 ± 1.0	54 ± 0.3
Ba_2YdIrO_6	59 ± 9.0	66 ± 3.8	46 ± 2.0	56 ± 2.4	80 ± 25	53 ± 2.9
Ba_2TbIrO_6	60 ± 14	77 ± 1.0	45 ± 1.9	63 ± 1.0	46 ± 6.3	55 ± 1.9
Ba_2CeIrO_6	70 ± 10	67 ± 5.4	60 ± 5.7	59 ± 1.7	230 ± 22	89 ± 5.4
IrO_2	49 ± 1.0	68 ± 0.4	46 ± 0.8	52 ± 0.5	60 ± 2.0	53 ± 1.0

R^2				
0.980	0.985	0.990	0.995	1.000

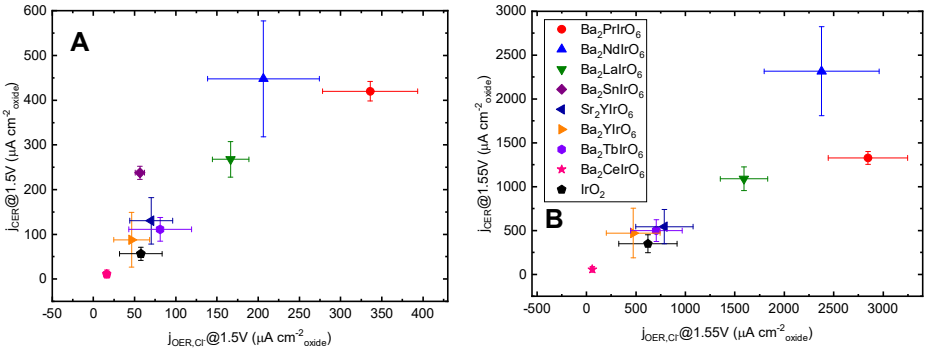

Figure A 9.3.10: Correlations between OER and CER activities, similar to Figure 3.4, but now comparing OER activity in the presence of 20 mM NaCl, at 1.50 V (A) and 1.55 V (B). Data derived from Figure 3.3B and Figure 3.6A, error bar show the standard deviation from at least three independent measurements.

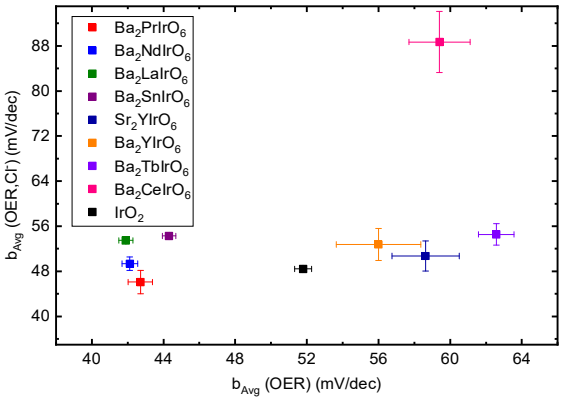

Figure A 9.3.11: Comparison of linear Tafel slope values for the OER, before and after NaCl addition (data from Table A 9.3.3).

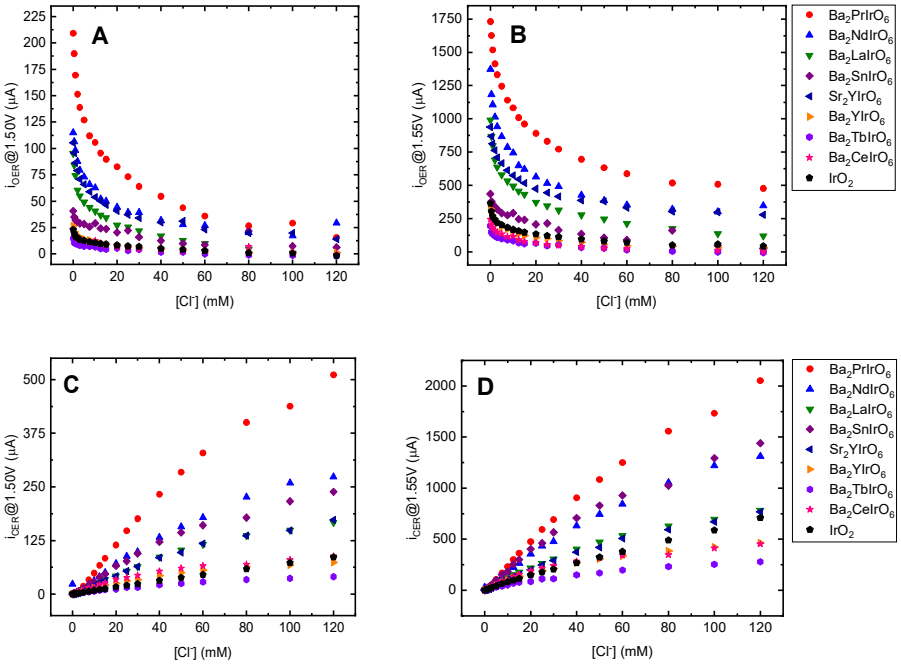

Figure A 9.3.12: Absolute OER currents (A and B) and CER currents (C and D) for all measured materials as function of increasing chloride concentration, at 1.50 V (A and C) and 1.55 V (B and D).

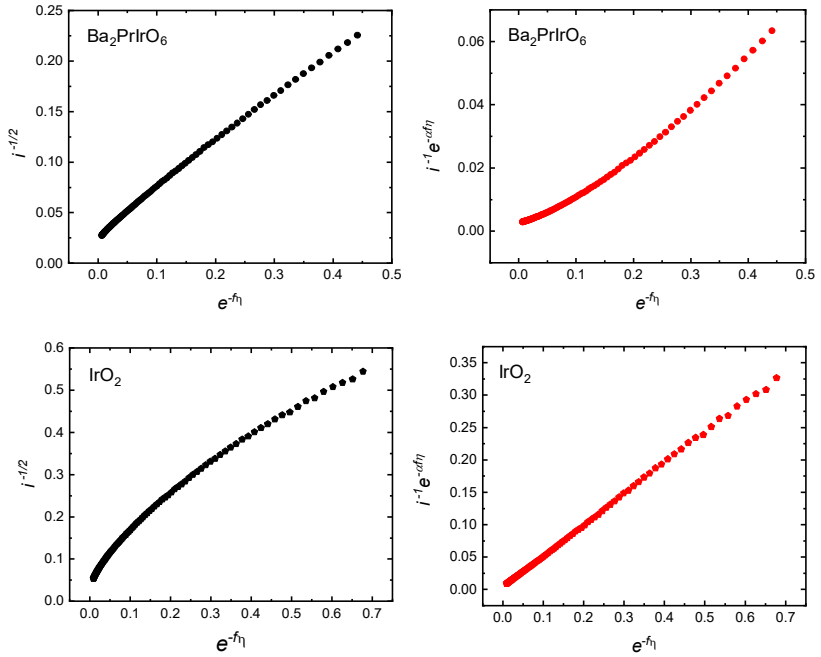

Figure A 9.3.13: Conway-Novák test plots (black) and Ferro-de Battisti test plots (red) for Ba_2PrIrO_6 and IrO_2. Conway and Novák proposed[118] that a straight line in a plot of $i^{-1/2}$ vs. $e^{-f\eta}$ is evidence of a Tafel-limited recombination mechanism with a Volmer pre-equilibrium. Extending this, Ferro *et al.*[113] proposed plotting $i^{-1}e^{\alpha f\eta}$ vs. $e^{-f\eta}$, where a straight line would instead suggest a Heyrovský (or Krishtalik) controlled mechanism. As in the main text, $\eta = E - E_0$ is the overpotential for CER, and $f = {}^{F}/_{(RT)}$. In the method by Ferro *et al.* α is not known beforehand. It can be estimated by observing the unique value of α (besides possibly α = 1) which results in a straight line, if any. E_0 was estimated by observing the onset of linearity in E vs. $\log|i_R|$ plots. In the case of IrO_2, α was chosen such that the resulting theoretical Tafel slope was 47 mV/dec, in accordance with data from Table A 9.3.3.

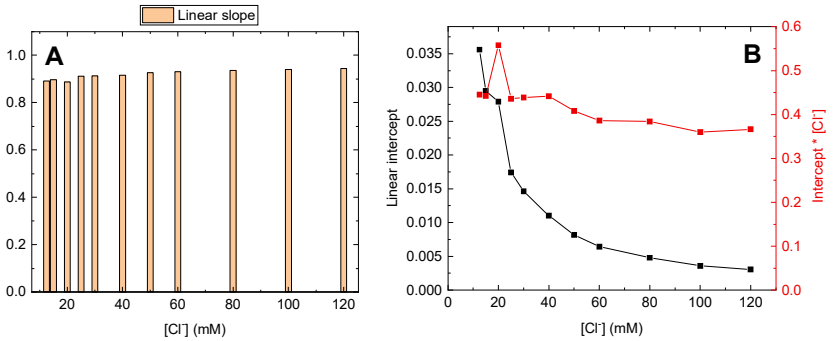

Figure A 9.3.14: Extracted values of the slope (A) and intercept (B) in the linear region as function of $[Cl^-]$, using data from Ferro-de Battisti plots as shown in Figure A 9.3.13, for IrO_2. Red trace in B shows the value of the intercept multiplied by the chloride concentration.

The appearance of a straight line in a Ferro-de Battisti plot does not discern between the V-H and the V-K mechanism. However, the method does lead to alternating predictions of the slope and intercept dependence. For the V-H pathway, these are given by $(2Fk_H^0K_V'[\mathrm{Cl}^-]^2)^{-1}$ and $(2Fk_H^0[\mathrm{Cl}^-])^{-1}$, respectively; In case the V-K mechanism dominates, it predicts $(2Fk_K^0K_V'[\mathrm{Cl}^-])^{-1}$ and $(2Fk_K^0)^{-1}$. One can observe that the intercept in B shows a marked dependence on $[\mathrm{Cl}^-]^{-1}$, which fits better with the V-H mechanism.

We further have to note that the chloride dependence of the slope remains quite constant versus $[\mathrm{Cl}^-]$. Although this contradicts both the V-H and V-K predictions at first glance, it must be noted that the slope value is affected as well by the pseudo-equilibrium constant K_V', the value of which depends strongly on $[\mathrm{Cl}^-]$.[118] Interpretation of the slopes is thus not straightforward.

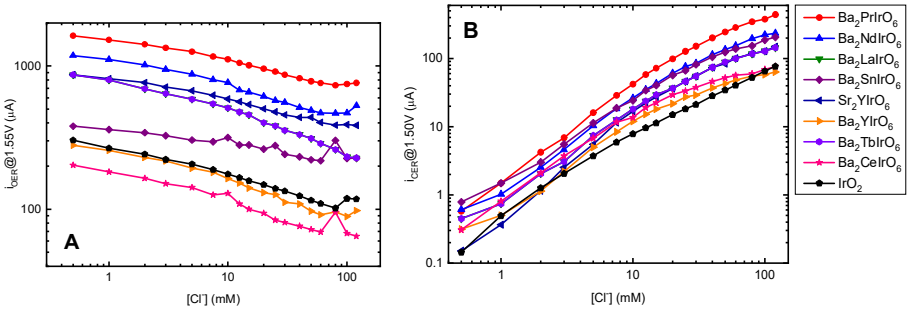

Figure A 9.3.15: Log-log plots of Figure A 9.3.12B (A) Figure A 9.3.12C (B).

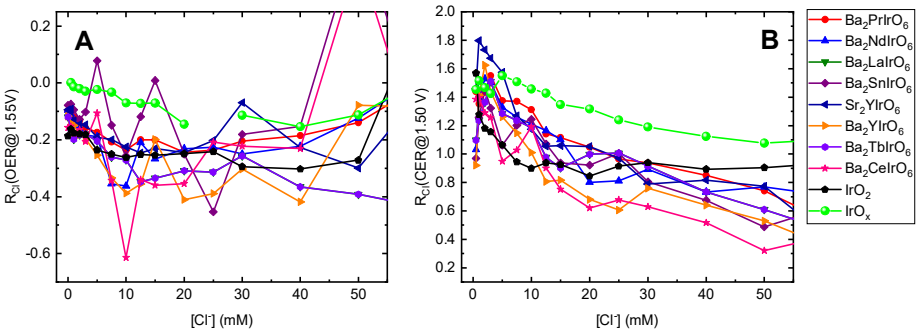

Figure A 9.3.16: Zoom of data in the 0-50 mM concentration range shown in Figure 3.7.

9.4. Supporting information for Chapter 4

9.4.1. Thermodynamic data of (inter)halogen species

Table A 9.4.1: Reactions of interhalogen compounds involving Cl and Br between formal oxidation states -1 and 0, in aqueous acidic conditions (pH < 1). Values as reported by Wang *et al.*[210] Additionally shown are standard redox potentials of equivalent electrochemical reactions. Participation of the species Cl_3^-, whose concentration is generally small, is ignored. Also included are standard literature values for the BER, CER, and OER. Note that the OER is pH-dependent on the NHE scale.

[a] The value of K_1 was determined from literature values and standard redox potentials.

Reaction	Equilibrium constant	Electrochemical reaction	Standard potential
$2\,BrCl \rightleftharpoons Cl_2 + Br_2$	$K_D = 5 * 10^{-3}$	$BrCl + 2\,e^- \rightleftharpoons Br^- + Cl^-$	$E^0_{BrCl} = 1.19$ V vs. NHE
$Cl_2 + Br^- \rightleftharpoons BrCl_2^-$	$K_1 = 4.6 * 10^6\ M^{-1}$ [a]	$BrCl_2^- + 2\,e^- \rightleftharpoons Br^- + 2\,Cl^-$	$E^0_{BrCl_2^-} = 1.16$ V vs. NHE
$BrCl + Cl^- \rightleftharpoons BrCl_2^-$	$K_2 = 6.0\ M^{-1}$		
$BrCl + Br^- \rightleftharpoons Br_2Cl^-$	$K_3 = 1.8 * 10^4\ M^{-1}$	$Br_2Cl^- + 2\,e^- \rightleftharpoons 2\,Br^- + Cl^-$	$E^0_{Br_2Cl^-} = 1.08$ V vs. NHE
$Br_2 + Cl^- \rightleftharpoons Br_2Cl^-$	$K_4 = 1.3\ M^{-1}$		
$Br_2 + Br^- \rightleftharpoons Br_3^-$	$K_{Br} = 16.1\ M^{-1}$	$Br_3^- + 2\,e^- \rightleftharpoons 3\,Br^-$	$E^0_{Br_3^-/Br^-} = 1.04$ V vs. NHE

9.4.2. Theoretical Tafel slopes and reaction orders for elementary kinetic mechanisms involving competitive adsorption

We will first regard the BER as the main reaction, with Cl^- as a competitive inhibitor for Br^- adsorption. As also shown in the main text, the fractional coverage of bromide θ_{Br} can be written using the mean-field Langmuir isotherm according to:

$$\theta_{Br} = \frac{K_{Br}[Br^-]e^{f\eta}}{K_{Br}[Br^-]e^{f\eta} + K_{Cl}[Cl^-]e^{f\eta} + 1} \qquad \text{Eq. A 9.4.1}$$

The theoretical BER j–η relationships for the Volmer-Tafel and Volmer-Heyrovský mechanisms can be written as:

$$j_{VT} = 2Fk_T(\theta_{Br})^2 = 2Fk_T\left(\frac{K_{Br}[Br^-]e^{f\eta}}{K_{Br}[Br^-]e^{f\eta} + K_{Cl}[Cl^-]e^{f\eta} + 1}\right)^2 \qquad \text{Eq. A 9.4.2}$$

$$j_{VH} = Fk_H e^{\alpha_H f\eta}[\mathrm{Br}^-]\theta_{Br} = Fk_H \frac{K_{Br}[\mathrm{Br}^-]^2 e^{(\alpha_H+1)f\eta}}{K_{Br}[\mathrm{Br}^-]e^{f\eta} + K_{Cl}[\mathrm{Cl}^-]e^{f\eta} + 1} \qquad \text{Eq. A 9.4.3}$$

The Br^- reaction order $\mathcal{R}_{\mathrm{Br}^-}$ of the overall reaction always contains a contribution from the surface-bound intermediate;[112] in case of the Langmuir isotherm, this 'surface reaction order' can be written as:

$$\mathcal{R}^S_{\mathrm{Br}^-} = \frac{\partial \ln \theta_{Br}}{\partial \ln[\mathrm{Br}^-]} = 1 - \theta_{Br} \qquad \text{Eq. A 9.4.4}$$

This relationship is valid regardless of whether competitive adsorption of Cl^- takes place. The effect of inhibition is implicitly included in θ_{Br} (see Eq. A 9.4.1). In case of a Volmer-Tafel mechanism, $\mathcal{R}_{\mathrm{Br}^-}$ is then always positive and dependent on the surface coverage θ_{Br}. It can be written as:[112]

$$\mathcal{R}_{\mathrm{Br}^-} = \frac{\partial \ln j}{\partial \ln[\theta_{Br}]} * \frac{\partial \ln \theta_{Br}}{\partial \ln[\mathrm{Br}^-]} = 2(1 - \theta_{Br}) \qquad \text{Eq. A 9.4.5}$$

Since it is assumed that the Cl^- competitor does not react further after adsorbing, it affects the overall reaction order only through the surface reaction order. Its reaction order $\mathcal{R}_{\mathrm{Cl}^-}$ can therefore be written as:

$$\mathcal{R}_{\mathrm{Cl}^-} = \frac{\partial \ln \theta_{Br}}{\partial \ln[\mathrm{Cl}^-]} = -\theta_{Cl} \qquad \text{Eq. A 9.4.6}$$

The values are always negative, as can be expected for a competitively adsorbing species. The BER dependence on Br^- and Cl^- predicted by the V-T, V-H and V-K mechanisms can then be expressed as shown below in Table A 9.4.2, along with some general limiting cases (Table A 9.4.3). In general, competitive adsorption does not change the *possible* limiting values of $\mathcal{R}_{\mathrm{Br}^-}$, but it may change the 'width' of the Br^- isotherm. It affects the range of values of $[\mathrm{Br}^-]$ or η within which b and $\mathcal{R}_{\mathrm{Br}^-}$ can vary. Whereas reaction orders should always approach their lower limit at high overpotentials (0, 1 and 0 for the V-T, V-H and V-K mechanisms, respectively), competitive adsorption may lead to other limiting values for high η, depending on the values of $K_{Br}[\mathrm{Br}^-]$ and $K_{Cl}[\mathrm{Cl}^-]$ (see Table A 9.4.3).

Table A 9.4.2: Theoretical Tafel slopes and reaction orders for Cl^- and Br^- in case of two step Volmer-Tafel or Volmer-Heyrovský BER reaction mechanisms, where Cl^- is a competitive electrochemical adsorbate. Relations for competition-free cases are obtained by setting $[Cl^-] = 0$.

	Volmer-Heyrovský	**Volmer-Krishtalik**
Tafel slope $b = \left(\frac{\partial \log j}{\partial \eta}\right)^{-1}$	$\frac{\ln(10)}{f}\left(\frac{K_{Br}[Br^-]e^{f\eta} + K_{Cl}[Cl^-]e^{f\eta} + 1}{\alpha_H(K_{Br}[Br^-]e^{f\eta} + K_{Cl}[Cl^-]e^{f\eta} + 1) + 1}\right)$	Same as Volmer-Heyrovský
Br^- reaction order $\mathcal{R}_{Br^-} = \frac{\partial \ln j}{\partial \ln[Br^-]}$	$2 - \theta_{Br}$ $= \frac{K_{Br}[Br^-]e^{f\eta} + 2K_{Cl}[Cl^-]e^{f\eta} + 2}{K_{Br}[Br^-]e^{f\eta} + K_{Cl}[Cl^-]e^{f\eta} + 1}$	$1 - \theta_{Br}$ $= \frac{K_{Cl}[Cl^-]e^{f\eta} + 1}{K_{Br}[Br^-]e^{f\eta} + K_{Cl}[Cl^-]e^{f\eta} + 1}$
Cl^- reaction order $\mathcal{R}_{Cl^-} = \frac{\partial \ln j}{\partial \ln[Cl^-]}$	$-\theta_{Cl}$ $= -\left(\frac{K_{Cl}[Cl^-]e^{f\eta}}{K_{Br}[Br^-]e^{f\eta} + K_{Cl}[Cl^-]e^{f\eta} + 1}\right)$	Same as Volmer-Heyrovský
	Volmer-Tafel	
Tafel slope $b = \left(\frac{\partial \log j}{\partial \eta}\right)^{-1}$	$\frac{\ln(10)}{2f}\frac{1}{(1 - \theta_{Br} - \theta_{Cl})}$ $= \frac{\ln(10)}{2f}(K_{Br}[Br^-]e^{f\eta} + K_{Cl}[Cl^-]e^{f\eta} + 1)$	
Br^- reaction order $\mathcal{R}_{Br^-} = \frac{\partial \ln j}{\partial \ln[Br^-]}$	$2(1 - \theta_{Br})$ $= 2\left(\frac{K_{Cl}[Cl^-]e^{f\eta} + 1}{K_{Br}[Br^-]e^{f\eta} + K_{Cl}[Cl^-]e^{f\eta} + 1}\right)$	
Cl^- reaction order $\mathcal{R}_{Cl^-} = \frac{\partial \ln j}{\partial \ln[Cl^-]}$	$-2\theta_{Cl}$ $= -2\left(\frac{K_{Cl}[Cl^-]e^{f\eta}}{K_{Br}[Br^-]e^{f\eta} + K_{Cl}[Cl^-]e^{f\eta} + 1}\right)$	

Table A 9.4.3: Cases of limiting behavior for two-step reaction BER mechanisms involving Cl^- as competitively adsorbing (but otherwise unreactive) species. Values are shown for the overpotential η and 'adsorption strength' $K_i[i^-]$ of the various species. It was assumed that $\alpha_H = 0.5$.

Limiting case		**Volmer-Heyrovský**	**Volmer-Krishtalik**
Tafel slope b	$\eta \to 0$	$b \approx 40$ mV dec^{-1} if $K_{Br}[\mathrm{Br}^-] = K_{Cl}[\mathrm{Cl}^-] \approx 0$ $b \to 120$ mV dec^{-1} for either $K_{Br}[\mathrm{Br}^-] \to \infty$ or $K_{Cl}[\mathrm{Cl}^-] \to \infty$	Same as Volmer-Heyrovský
	$\eta \to \infty$	$b \to 120$ mV dec^{-1}	
Br^- reaction order $\mathcal{R}_{\mathrm{Br}^-}$	$\eta \to 0$	$\mathcal{R}_{\mathrm{Br}^-} \approx 2$ if $K_{Br}[\mathrm{Br}^-] \approx 0$ $1 \leq \mathcal{R}_{\mathrm{Br}^-} \leq 2$ if $K_{Cl}[\mathrm{Cl}^-] \approx 0$	$\mathcal{R}_{\mathrm{Br}^-} \approx 1$ if $K_{Br}[\mathrm{Cl}^-] \approx 0$ $0 \leq \mathcal{R}_{\mathrm{Br}^-} \leq 1$ if $K_{Cl}[\mathrm{Cl}^-] \approx 0$
	$\eta \to \infty$	$\frac{K_{Br}[\mathrm{Br}^-] + 2K_{Cl}[\mathrm{Cl}^-]}{K_{Br}[\mathrm{Br}^-] + K_{Cl}[\mathrm{Cl}^-]}$	$\frac{K_{Cl}[\mathrm{Cl}^-]}{K_{Br}[\mathrm{Br}^-] + K_{Cl}[\mathrm{Cl}^-]}$
Cl^- reaction order $\mathcal{R}_{\mathrm{Cl}^-}$	$\eta \to 0$	$\mathcal{R}_{\mathrm{Cl}^-} \approx 0$ if $K_{Cl}[\mathrm{Cl}^-] \approx 0$ $-1 \leq \mathcal{R}_{\mathrm{Cl}^-} \leq 0$ if $K_{Br}[\mathrm{Br}^-] \approx 0$	Same as Volmer-Heyrovský
	$\eta \to \infty$	$-\left(\frac{K_{Cl}[\mathrm{Cl}^-]}{K_{Br}[\mathrm{Br}^-] + K_{Cl}[\mathrm{Cl}^-]}\right)$	
Limiting case		**Volmer-Tafel**	
Tafel slope b	$\eta \to 0$	$b \approx 30$ mV dec^{-1} if $K_{Br}[\mathrm{Br}^-] = K_{Cl}[\mathrm{Cl}^-] \approx 0$ $b \to \infty$ for either $K_{Br}[\mathrm{Br}^-] \to \infty$ or $K_{Cl}[\mathrm{Cl}^-] \to \infty$	
	$\eta \to \infty$	$b \to \infty$	
Br^- reaction order $\mathcal{R}_{\mathrm{Br}^-}$	$\eta \to 0$	$\mathcal{R}_{\mathrm{Br}^-} \approx 2$ if $K_{Br}[\mathrm{Br}^-] \approx 0$ $0 \leq \mathcal{R}_{\mathrm{Br}^-} \leq 2$ if $K_{Cl}[\mathrm{Cl}^-] \approx 0$	
	$\eta \to \infty$	$2\left(\frac{K_{Cl}[\mathrm{Cl}^-]}{K_{Br}[\mathrm{Br}^-] + K_{Cl}[\mathrm{Cl}^-]}\right)$	
Cl^- reaction order $\mathcal{R}_{\mathrm{Cl}^-}$	$\eta \to 0$	$\mathcal{R}_{\mathrm{Cl}^-} \approx 0$ if $K_{Cl}[\mathrm{Cl}^-] \approx 0$ $-2 \leq \mathcal{R}_{\mathrm{Cl}^-} \leq 0$ if $K_{Br}[\mathrm{Br}^-] \approx 0$	
	$\eta \to \infty$	$-2\left(\frac{K_{Cl}[\mathrm{Cl}^-]}{K_{Br}[\mathrm{Br}^-] + K_{Cl}[\mathrm{Cl}^-]}\right)$	

Besides exerting a simple blocking effect, chloride could also become involved in follow-up reactions when Br is co-adsorbed on the surface, such as BrCl formation. The corresponding reaction pathway would be similar to Volmer-Tafel, reminiscent of a Langmuir-Hinshelwood mechanism in heterogeneous gas-phase catalysis:

$$Br^- + * \rightleftarrows Br^* + e^- \qquad \text{Eq. A 9.4.7}$$

$$Cl^- + * \rightleftarrows Cl^* + e^- \qquad \text{Eq. A 9.4.8}$$

$$Br^* + Cl^* \rightleftarrows BrCl + 2* \qquad \text{Eq. A 9.4.9}$$

We apply the same assumptions regarding the Cl and Br adsorption isotherms as discussed previously. Neglecting the backward reaction, the current-potential relation then becomes:

$$j_3 = 2Fk_3\theta_{Br}\theta_{Cl} = 2Fk_3\left(\frac{(K_{Br}K_{Cl}[Br^-][Cl^-])^{\frac{1}{2}}e^{f\eta}}{K_{Br}[Br^-]e^{f\eta} + K_{Cl}[Cl^-]e^{f\eta} + 1}\right)^2 \qquad \text{Eq. A 9.4.10}$$

where k_3 is the chemical forward rate constant for recombination in Eq. A 9.4.9. Eq. A 9.4.10 predicts Tafel slopes identical to the V-T mechanism of either the BER or CER, under the effect of competitive adsorption between Br^- and Cl^- (see Table A 9.4.2).

Although less likely on Pt, one can also consider a Volmer-Heyrovský mechanism for BrCl formation, via two analogous pathways:

$$Br^- + * \rightleftarrows Br^* + e^- \qquad \text{Eq. A 9.4.11}$$

$$Br^* + Cl^- \rightleftarrows BrCl + e^- + * \qquad \text{Eq. A 9.4.12}$$

$$Cl^- + * \rightleftarrows Cl^* + e^- \qquad \text{Eq. A 9.4.13}$$

$$Cl^* + Br^- \rightleftarrows BrCl + e^- \qquad \text{Eq. A 9.4.14}$$

On the potential scale of the second step, which concerns electrochemical desorption with two different atom types, both mechanisms have a forward reaction that (under the assumption that α_H is identical for both) is proportional to:

$$j \propto \frac{[Br^-][Cl^-]e^{(\alpha_H+1)f\eta}}{K_{Cl}[Cl^-]e^{f\eta} + K_{Br}[Br^-]e^{f\eta} + 1} \qquad \text{Eq. A 9.4.15}$$

The Tafel slopes predicted by Eq. A 9.4.15 are the same as predicted by the V-H mechanism for the BER or CER under the effect of Br^- and Cl^- competitive adsorption (Table A 9.4.2).

Finally, BrCl formation mechanisms can be written for a pathway analogous to the Volmer-Krishtalik mechanism. In the V-K pathway, the order of adsorption does matter. The reactant that adsorbs first (which is likely Br^-, due to its higher adsorption strength[218]) has a reaction order according to $\mathcal{R} = 1 - \theta$, whereas the second reactant (which is not involved in the rate-determining step or preceding steps) behaves purely competitive, such that $\mathcal{R} = -\theta$, even though it is necessary for the reaction to occur.

The theoretical Tafel slopes for the formation of BrCl from a V-T, V-H or V-K type mechanism are the same as shown in Table A 9.4.2. The reaction orders are shown in Table A 9.4.4 below. For the V-T mechanism, $\mathcal{R}_{Cl^-}$ and $\mathcal{R}_{Br^-}$ can now vary between -1 and 1.

Table A 9.4.4: Theoretical reaction orders for Cl^- and Br^- in case of BrCl reaction mechanisms.

	Volmer-Tafel	**Volmer-Heyrovský**
Br^- reaction order $\mathcal{R}_{Br^-}$	$1-2\theta_{Br}$ $=\frac{K'_{Cl}[Cl^-]e^{f\eta_1}-K_{Br}[Br^-]e^{f\eta_1}+1}{K'_{Br}[Br^-]e^{f\eta_1}+K_{Cl}[Cl^-]e^{f\eta_1}+1}$	$1-\theta_{Br}$ $=\frac{K''_{Cl}[Cl^-]e^{f\eta_2}+1}{K'_{Cl}[Cl^-]e^{f\eta_2}+K''_{Br}[Br^-]e^{f\eta_2}+1}$
Cl^- reaction order $\mathcal{R}_{Cl^-}$	$1-2\theta_{Cl}$ $=\frac{K'_{Br}[Br^-]e^{f\eta_1}-K_{Cl}[Cl^-]e^{f\eta_1}+1}{K'_{Br}[Br^-]e^{f\eta_1}+K_{Cl}[Cl^-]e^{f\eta_1}+1}$	$1-\theta_{Cl}$ $=\frac{K''_{Br}[Br^-]e^{f\eta_2}+1}{K'_{Cl}[Cl^-]e^{f\eta_2}+K''_{Br}[Br^-]e^{f\eta_2}+1}$
	Volmer-Krishtalik	
Br^- reaction order $\mathcal{R}_{Br^-}$	$1-\theta_{Br}$ if $\mathcal{R}_{Cl^-}=-\theta_{Cl}$ $-\theta_{Br}$ if $\mathcal{R}_{Cl^-}=1-\theta_{Cl}$	
Cl^- reaction order $\mathcal{R}_{Cl^-}$	$1-\theta_{Cl}$ if $\mathcal{R}_{Br^-}=-\theta_{Br}$ $-\theta_{Cl}$ if $\mathcal{R}_{Br^-}=1-\theta_{Br}$	

9.4.3. Reaction orders measured versus constant overpotential

Instead of referencing the applied potential to a fixed point according to $\eta = E - E^0$, it can be convenient to experimentally measure reaction orders versus constant overpotential, $\eta^* = E - E_{eq}$, where E_{eq} is the equilibrium potential of the reaction of interest under the corresponding experimental conditions.[118,350] Taking the CER as example, η and η^* are related through the Nernst equation:

$$e^{f\eta} = \frac{[Cl_2]^{\frac{1}{2}}}{[Cl^-]} e^{f\eta^*} \qquad \text{Eq. A 9.4.16}$$

When re-writing the Volmer pre-equilibrium (Eq. 1.12 in Chapter 0) according to η^*:

$$\theta_{Cl}(\eta^*) = \frac{K_1[Cl_2]^{\frac{1}{2}} e^{f\eta^*}}{1 + K_1[Cl_2]^{\frac{1}{2}} e^{f\eta^*}} \qquad \text{Eq. A 9.4.17}$$

From Eq. A 9.4.17, is it clear that $\theta_{Cl}(\eta^*)$ is no longer dependent on $[Cl^-]$. The surface reaction order of chloride is therefore always zero versus constant overpotential:

$$\mathcal{R}^{S}_{\mathrm{Cl^-}}(\eta^*) = \frac{\partial \ln \theta_{Cl}(\eta^*)}{\partial \ln[\mathrm{Cl^-}]} = 0 \qquad \text{Eq. A 9.4.18}$$

Eq. A 9.4.18 implies that for the V-T mechanism, the overall chloride reaction order measured versus constant overpotential $\mathcal{R}_{\mathrm{Cl^-}}(\eta^*)$ is always zero. In case of the V-H and V-K mechanism, it can be shown that $\mathcal{R}_{\mathrm{Cl^-}}(\eta^*)$ corresponds to $1-\alpha_H$ and $-\alpha_K$, respectively; the expected reaction orders are non-zero (and negative in the case of V-K), but independent of $[\mathrm{Cl^-}]$ or η^*.

9.4.4. <u>Various supplementary RRDE data</u>

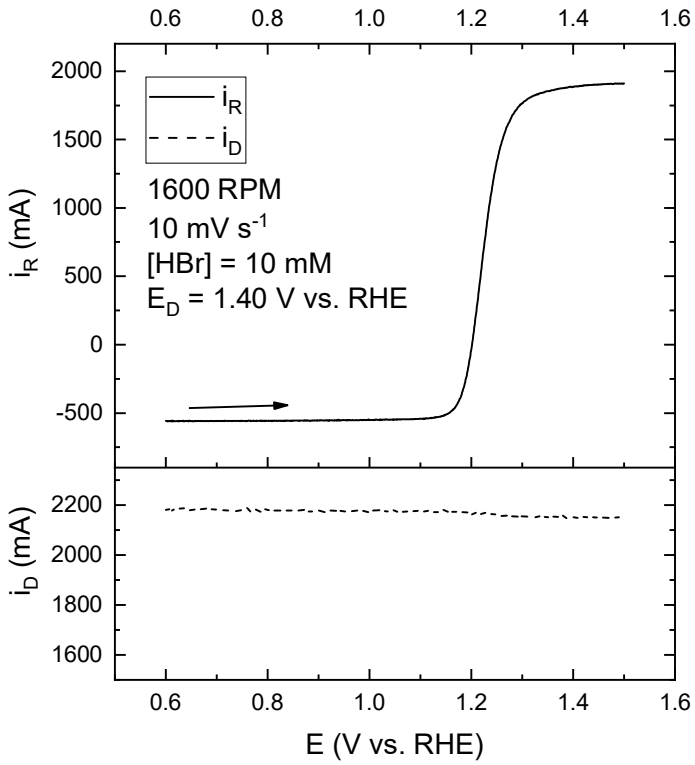

Figure A 9.4.1: Test of the bromine reduction reaction (BRR) diffusion limitation. Figure shows an LSV of a Pt-Pt RRDE electrode in a 0.1 M $HClO_4$ solution containing 10 mM HBr. The ring electrode was scanned (top) while keeping the disk at a fixed potential of 1.45 V vs. RHE (bottom), to provide a significant concentration of Br_2/Br_3^- near the ring electrode surface. Diffusion limitation of the BRR sets in at roughly 1.05 V vs. RHE ($\eta \approx 150$ mV). Arrow indicates scan direction.

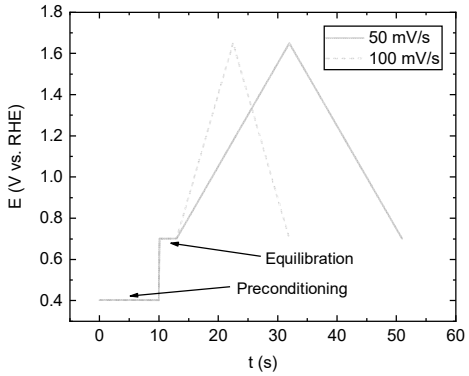

Figure A 9.4.2: Illustration of potential versus time program used during RRDE experiments, showing the preconditioning and equilibration steps during pre-treatment.

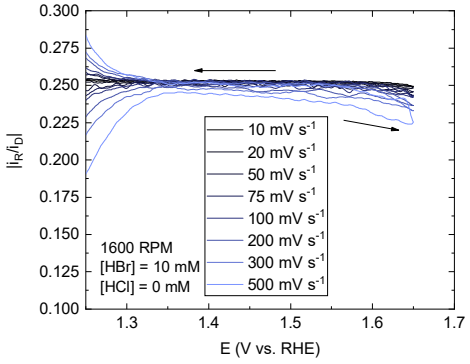

Figure A 9.4.3: Absolute values of ring/disk current ratios from Figure 4.1A. Arrows indicate scan direction.

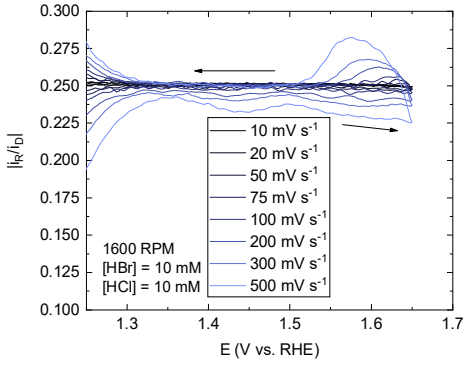

Figure A 9.4.4: Absolute values of ring/disk current ratios from Figure 4.1C. Arrows indicate scan direction.

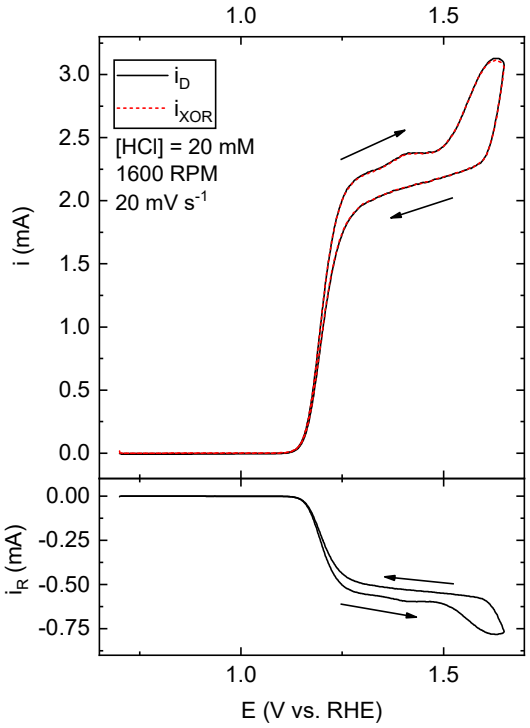

Figure A 9.4.5: Comparison of ring currents measured during an RRDE experiment. Data shown is a cyclic voltammogram of the Pt-Pt RRDE in a solution of 0.1 M $HClO_4$ + 10 mM HBr + 20 mM HCl, recorded at 20 mV s^{-1} at a fixed rotation rate of 1600 RPM. Black traces show disk (top panel) and ring (lower panel) currents. Red dashed trace shows the absolute value for the ring currents corrected for the RRDE collection factor, corresponding to currents from 'halogen oxidation reactions', i_{XOR}. Arrows indicate scan direction.

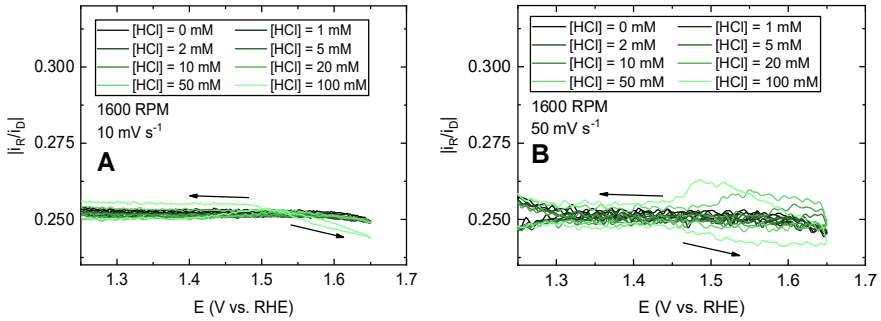

Figure A 9.4.6: Absolute values of ring/disk current ratios from Figure 4.2A (A) and Figure 4.2B (B). Arrows indicate scan direction.

9.4.5. Supplementary bromide oxidation data

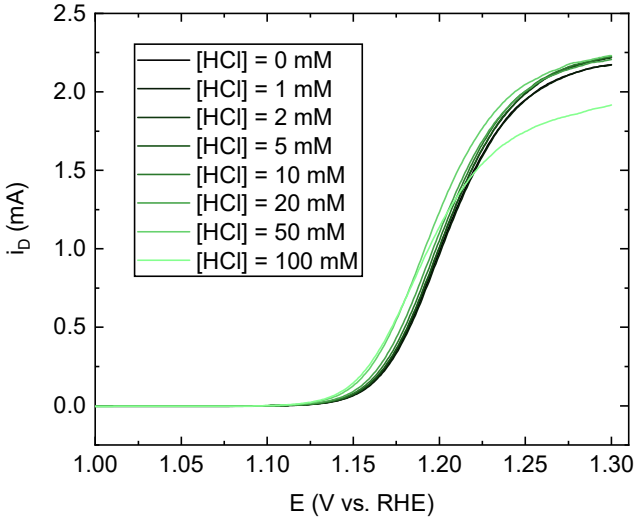

Figure A 9.4.7: Zoom of Figure 4.2A, centered around the onset of bromide oxidation as recorded on the RHE potential scale.

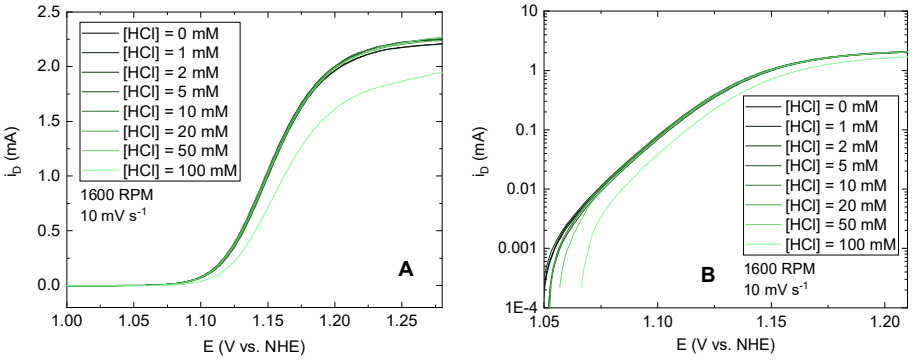

Figure A 9.4.8: Data from Figure A 9.4.7 converted to the NHE potential scale (A). B shows corresponding semilogarithmic plots of $\log(i_D)$ versus E.

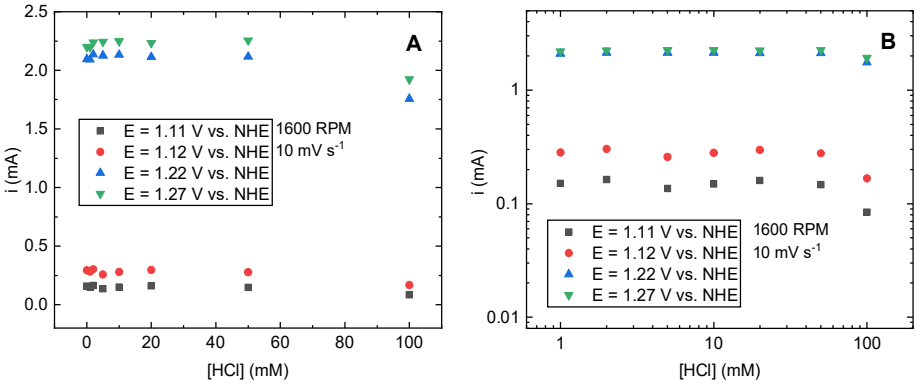

Figure A 9.4.9: Currents at constant potential values as function of HCl concentration (A), using data shown in Figure A 9.4.9. B: Corresponding log-log plots.

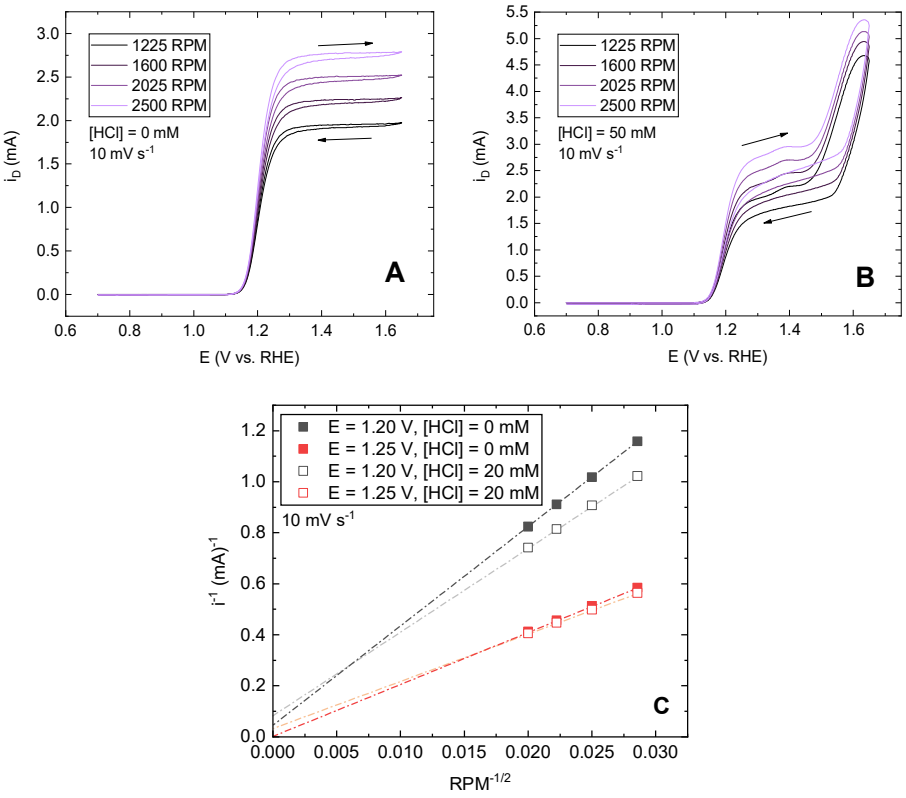

Figure A 9.4.10: Cyclic voltammograms of a Pt-Pt RRDE in a solution of 0.1 M $HClO_4$ + 10 mM HBr. A shows the effect of changing rotation rate, recorded at a scan rate of 10 mV s^{-1}. B shows the same experiment in the additional presence of 50 mM HCl. Arrows indicate scan direction. In C, typical examples of Koutecký-Levich plots are shown obtained from the forward scans of CVs such as shown in A and B.

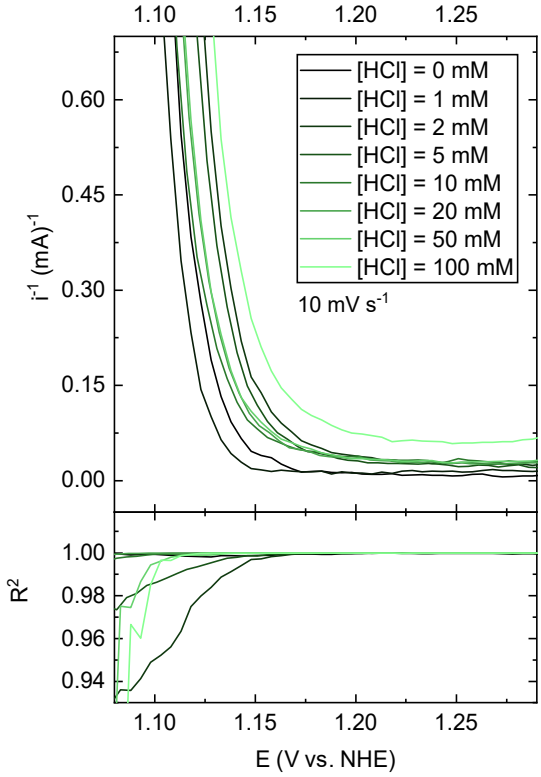

Figure A 9.4.11: Values of the y-intercept in Koutecký-Levich plots (see Figure A 9.4.10) across the bromide oxidation wave, as function of potential and chloride concentration. Lower panel shows the associated error in linearity of the underlying KL-plots.

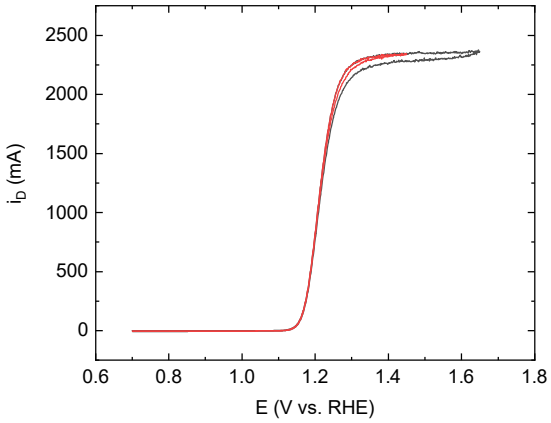

Figure A 9.4.12: Cyclic voltammogram of a Pt-Pt RRDE in a solution of 0.1 M $HClO_4$ + 10 mM HBr at a scan rate of 10 mV s^{-1} and rotation rate of 1600 RPM, showing the effect of the upper potential limit. Shown are potential cycles up to 1.65 V (black trace) and 1.45 V (red trace). Formation of PtO_x is apparent from increased hysteresis in the scan up to 1.65 V.

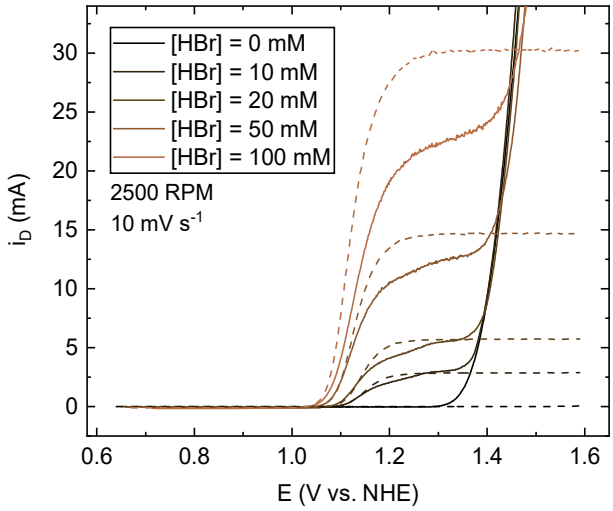

Figure A 9.4.13: Bromide oxidation currents measured under varying [HBr], in the presence of 0.1 M $HClO_4$ and 1 M HCl, measured at a fixed scan rate of 10 mV s^{-1} and rotation rate of 2500 RPM. Only forward scans are shown. Dashed lines correspond to BER data measured in absence of HCl under otherwise identical conditions.

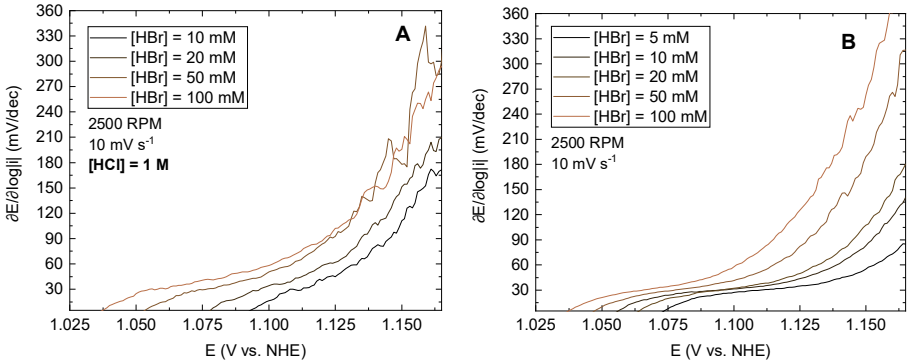

Figure A 9.4.14: Tafel slope values in activation-controlled bromide oxidation region of curves shown in Figure A 9.4.13. Only forward scans are shown. A: bromide oxidation for various [HBr] in presence of 1 M HCl (data from Figure A 9.4.13, solid lines). B: bromide oxidation for various [HBr] in absence of HCl (data from Figure A 9.4.13, dashed lines).

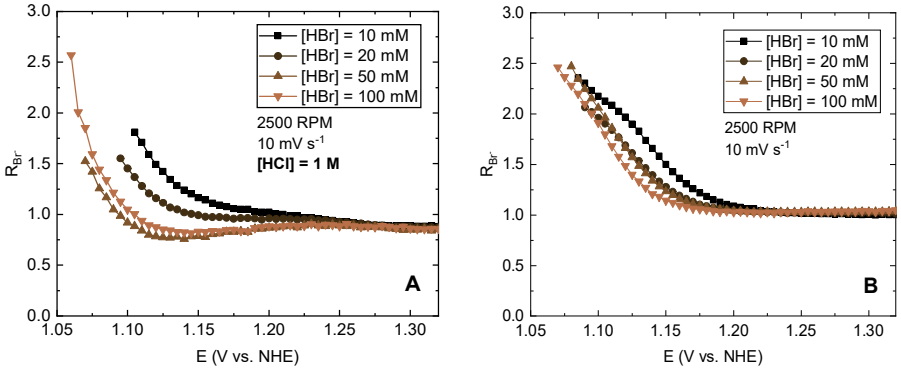

Figure A 9.4.15: Bromide reaction order $\mathcal{R}_{Br^-}$ in the bromide oxidation potential region, in presence (A) and absence (B) of 1 M HCl, based on data shown in Figure A 9.4.13. Values shown versus potential.

9.4.6. Supplementary chloride oxidation data

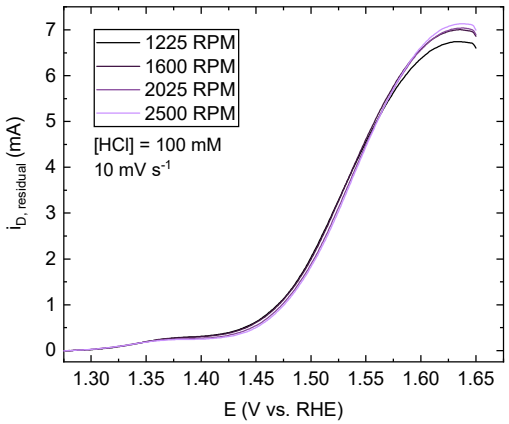

Figure A 9.4.16: Rotation rate dependence of the residual chloride oxidation currents after BER, such as in Figure 4.4, at a higher chloride concentration of 100 mM.

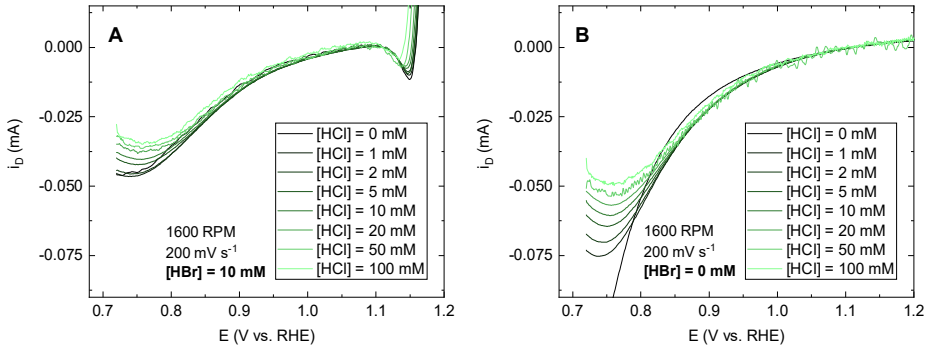

Figure A 9.4.17: PtO_x reduction peaks in the backward scans of RRDE experiments, as function of chloride concentration. Data with a relatively high scan rate (200 mV s^{-1}) were chosen where the reduction peaks are clearly visible. Shown are the reduction peaks in presence (A) and absence (B) of Br^-.

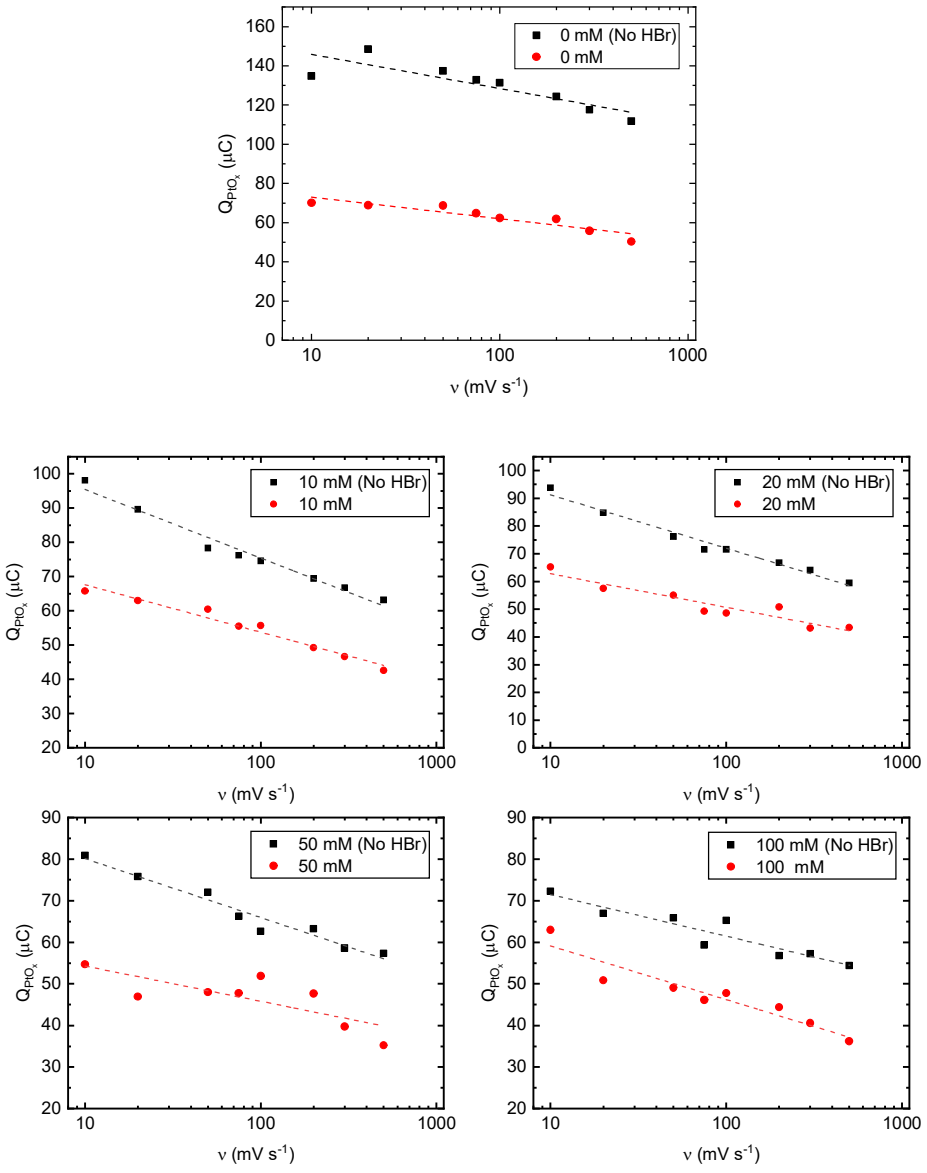

Figure A 9.4.18: Charges of the PtO_x reduction peak (Q_{PtO_x}) as a function of scan rate, for varying [Cl^-] concentrations. Data is shown in presence (red) and absence (black) of 10 mM HBr. Top figure has data in absence of chloride ([HCl] = 0 mM). Data were determined from backward CV scans such as those in Figure A 9.4.17, by measuring the peak charge up until the potential of peak current and multiplying by two. This was made possible by the generally symmetric shape of reduction peaks.

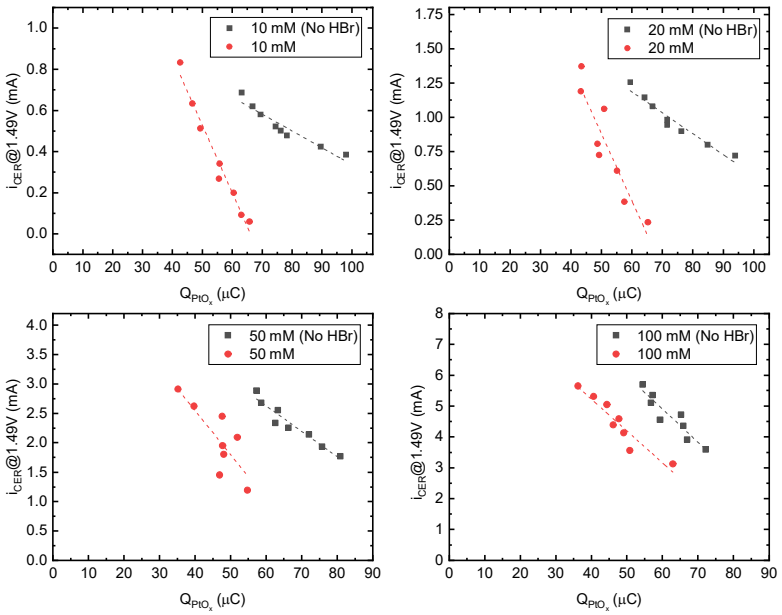

Figure A 9.4.19: CER currents obtained at 1600 RPM at 1.49 V vs. NHE, versus charges of the PtO_x reduction peak (Q_{PtO_x}), for varying $[Cl^-]/[Br^-]$ ratios (see also Figure A 9.4.18).

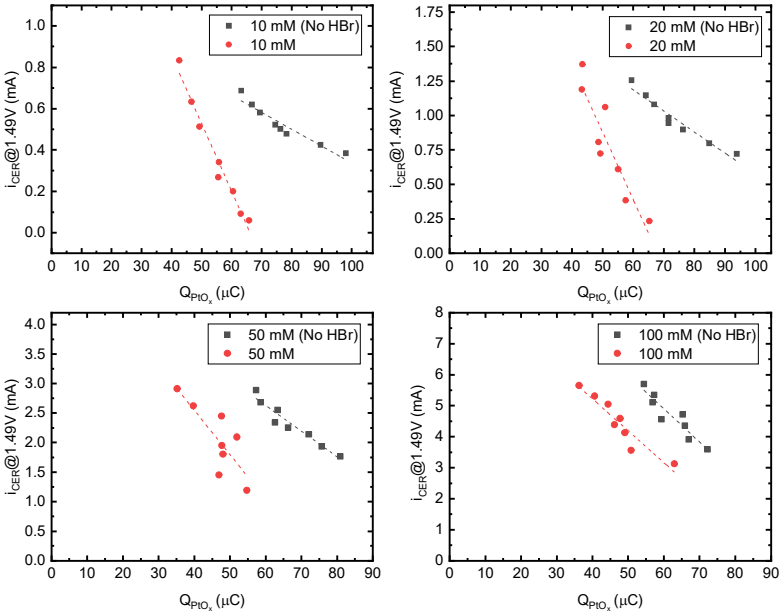

Figure A 9.4.20: Similar to Figure A 9.4.19, but showing CER currents obtained at 1.57 V vs. NHE.

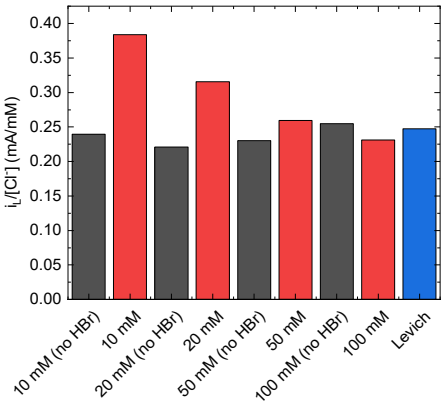

Figure A 9.4.21: Currents recorded at 1.57 V (Figure A 9.4.20) extrapolated to $Q_{PtO_x} = 0$ (a 'PtO_x-free' surface), along with diffusion-limited currents predicted by the Levich equation (blue). All values are shown normalized to the chloride concentration.

9.4.7. <u>Supplementary pre-peak data</u>

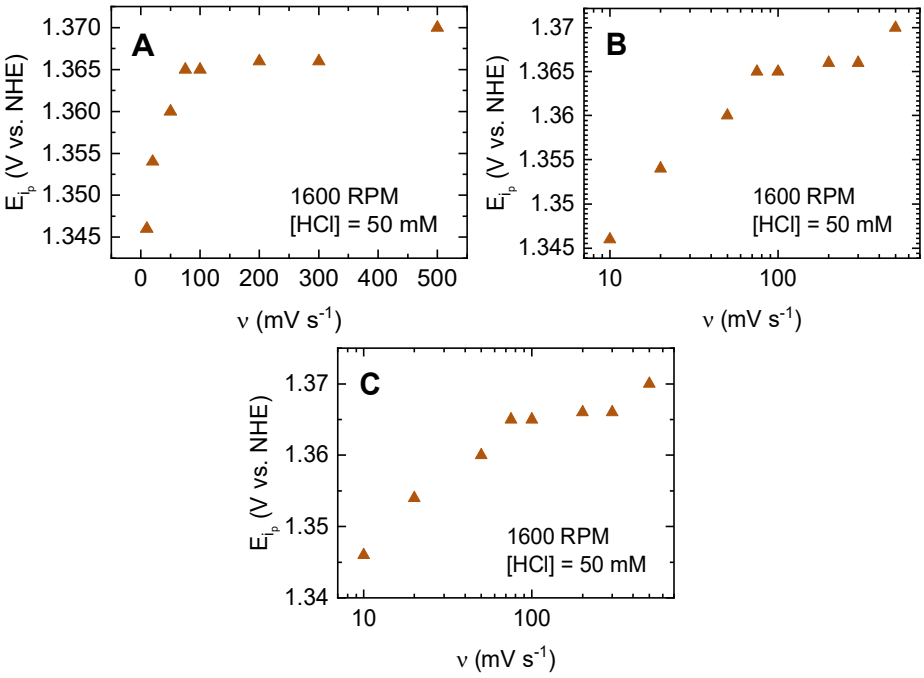

Figure A 9.4.22: Dependency of the pre-peak peak potential on the scan rate for the CER pre-peak, in linear (A), log-log (B), and semi-log plots (C). Figures B and C have nearly identical y-axes due to their y-values all being very close to 1.

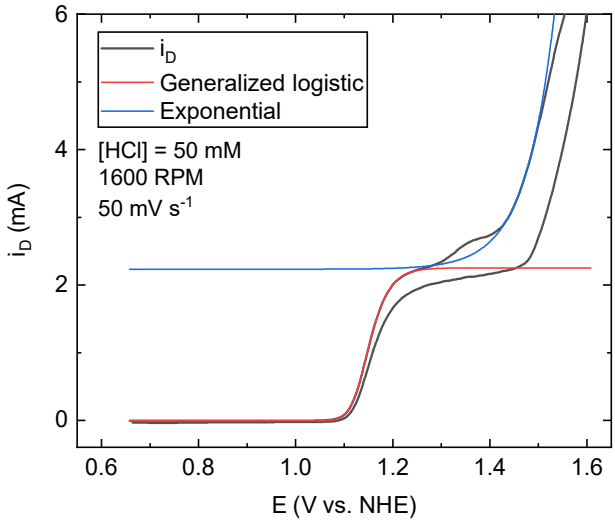

Figure A 9.4.23: Illustration of the fitting procedure to deconvolute BER currents and to isolate the chloride oxidation pre-peak.

The used generalized logistic function (blue curve) and exponential fitting functions (red curve) are given by:

$$\mathrm{i_D} = i_{L,BOR}^{min} + \frac{i_{L,BOR}^{max} - i_{L,BOR}^{min}}{\left[1 + \left(\frac{E}{x_0}\right)^{-h}\right]^{s}} \qquad \text{Eq. A 9.4.19}$$

$$\mathrm{i_D} = i_{L,BOR}^{max} + A_1 \exp\left(\frac{(E - E_0)}{t_0}\right) \qquad \text{Eq. A 9.4.20}$$

In these equations, $i_{L,BOR}^{min}$ and $i_{L,BOR}^{max}$ are the fitted limiting currents for the bromide oxidation wave in the low and high potential limit, respectively (where $i_{L,BOR}^{min} \approx 0$). E_0, x_0, h, s, A_1 and t_0 were parameters to be optimized.

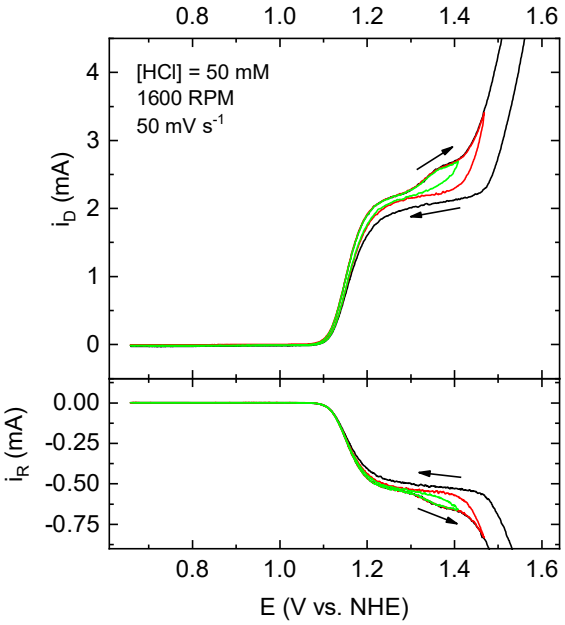

Figure A 9.4.24: CVs comparable to those measured in the main text in a solution of 0.1 M $HClO_4$ + 10 mM HBr + 50 mM HCl, but with varying upper potential windows.

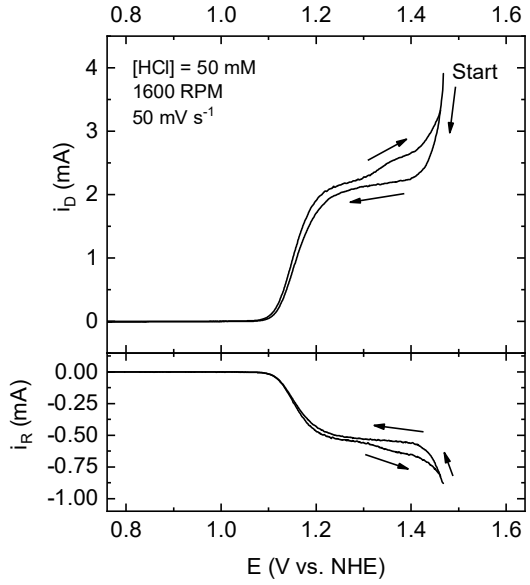

Figure A 9.4.25: CV comparable to those measured in the main text in a solution of 0.1 M $HClO_4$ + 10 mM HBr + 50 mM HCl, but with the start and end potentials reversed. The forward sweep was started at 1.51 V, and reversed at 0.7 V.

9.4.8. Supplementary UV-Vis data

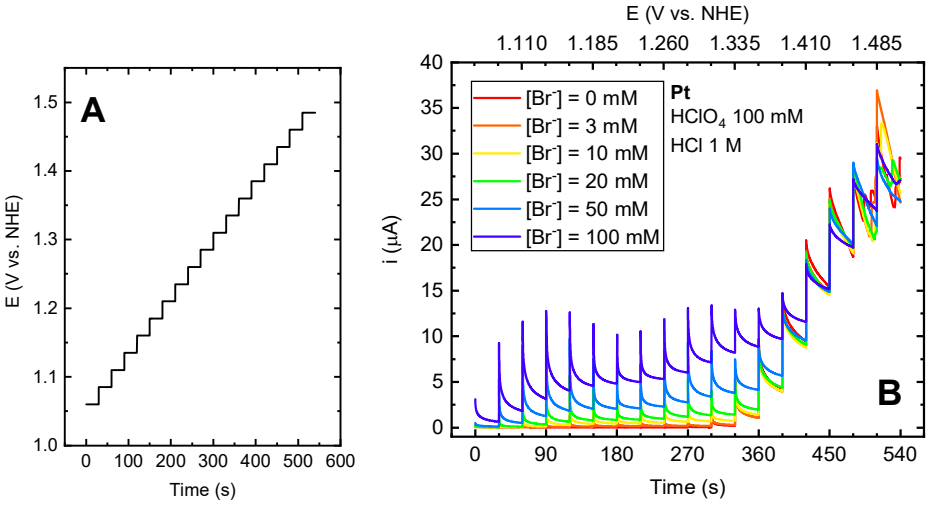

Figure A 9.4.26: E vs. t program used during the UV-Vis experiments in 1 M HCl (A). Panel B shows full data of the currents recorded during UV-Vis experiments in Figure 4.9.

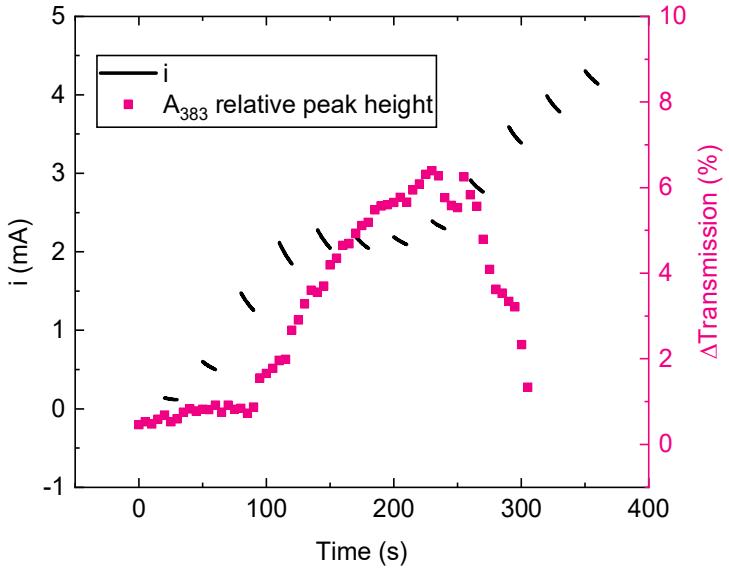

Figure A 9.4.27: Comparison of currents recorded during the BER wave belonging to data in Figure 4.10, and relative peak heights in the UV-Vis data, which can be ascribed to the extent of Br_2Cl^- formation. UV-Vis peak data were determined by calculating the difference between the local minimum and local maximum within 340 – 380 nm in Figure 4.10.

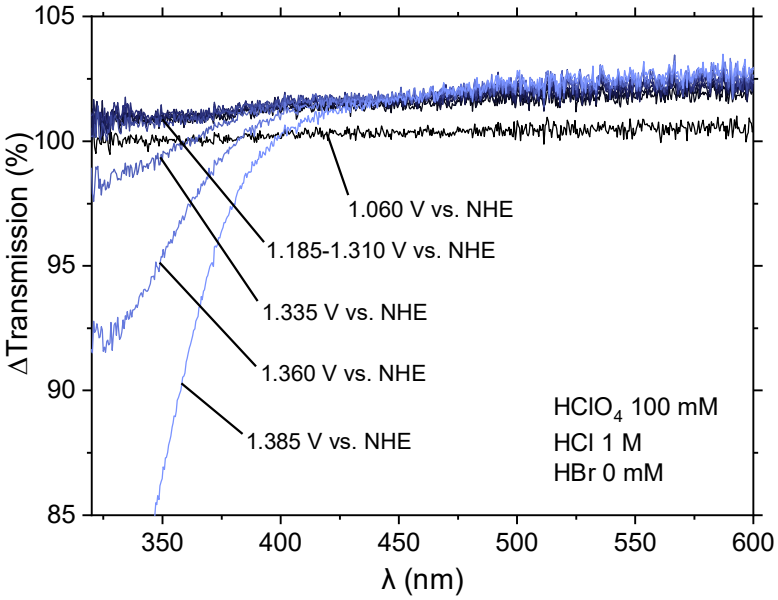

Figure A 9.4.28: UV-Vis data belonging to the experiment in Figure A 9.4.26 where [HBr] = 0 mM, such that all changes in transmission can be ascribed to the appearance of Cl_2.

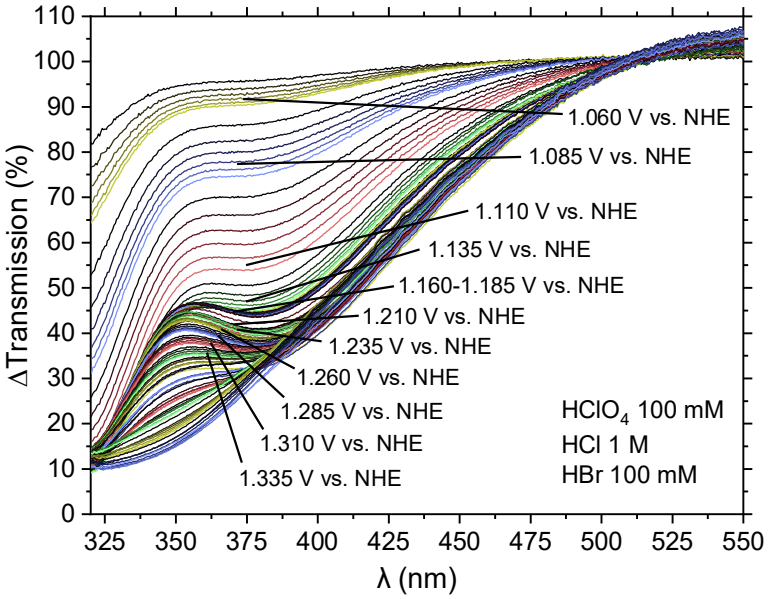

Figure A 9.4.29: Complete set of UV-Vis experiments for parallel bromide and chloride oxidation in 1 M HCl and 100 mM HBr, similar to Figure 4.10.

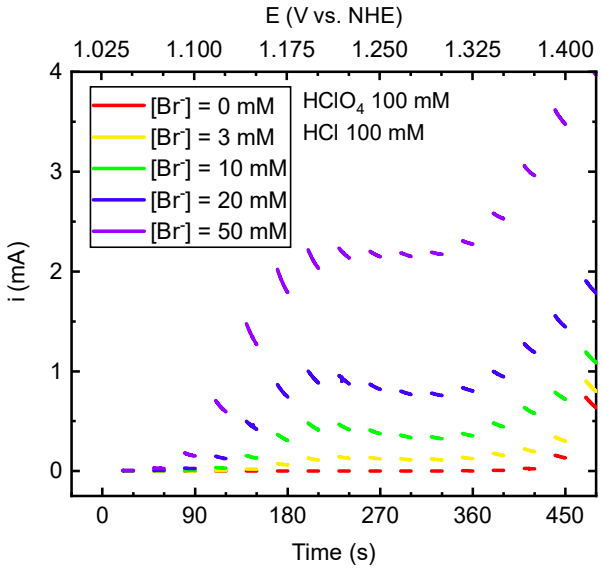

Figure A 9.4.30: Recorded currents during UV-Vis measurements such as in Figure 4.9, involving a stationary Pt/FTO electrode in a solution of 0.1 M $HClO_4$ + 0.1 M HCl, in presence of various [HBr].

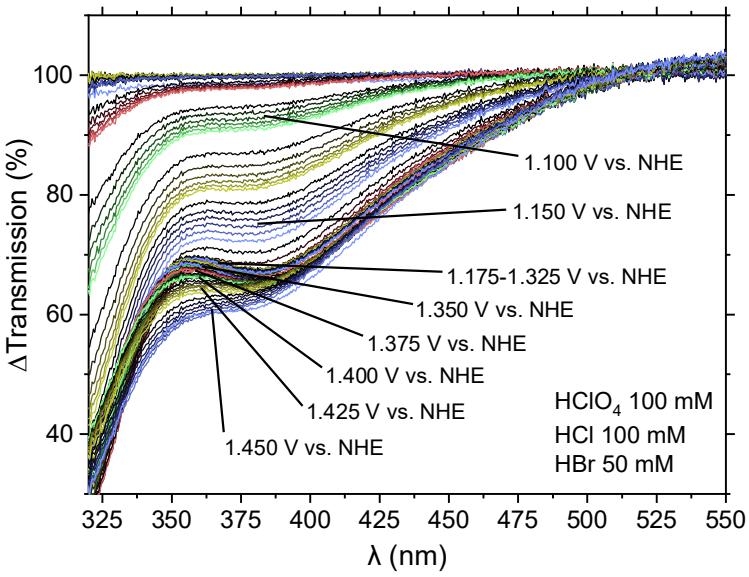

Figure A 9.4.31: Complete set of UV-Vis experiments for parallel bromide and chloride oxidation such as in Figure 4.10 and Figure A 9.4.29, corresponding to one of the experiments in Figure A 9.4.30 ([HBr] = 50 mM). The potential where the local maximum at 350 nm starts decreasing can be estimated at 1.375 V.

9.5. Supporting information for Chapter 5

9.5.1. Supplementary RRDE data

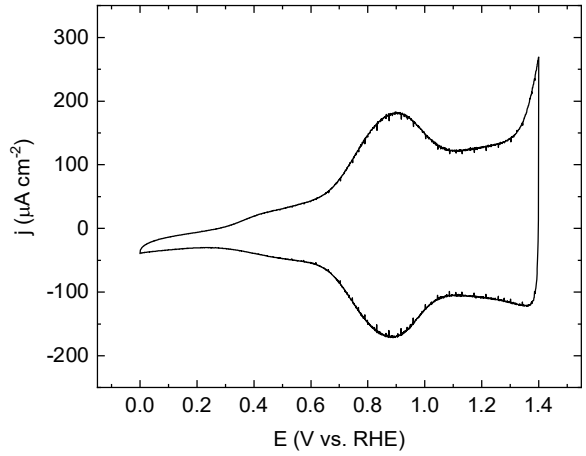

Figure A 9.5.1: Voltammetric characterization of the IrO_x/GC catalyst, in 0.1 M $HClO_4$. Scan rate: 50 mV s^{-1}.

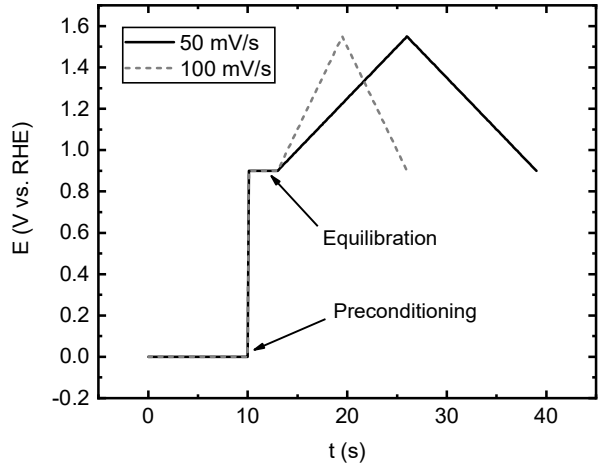

Figure A 9.5.2: Potential versus time program used during RRDE experiments, illustrating the preconditioning and equilibration steps preceding every experiment.

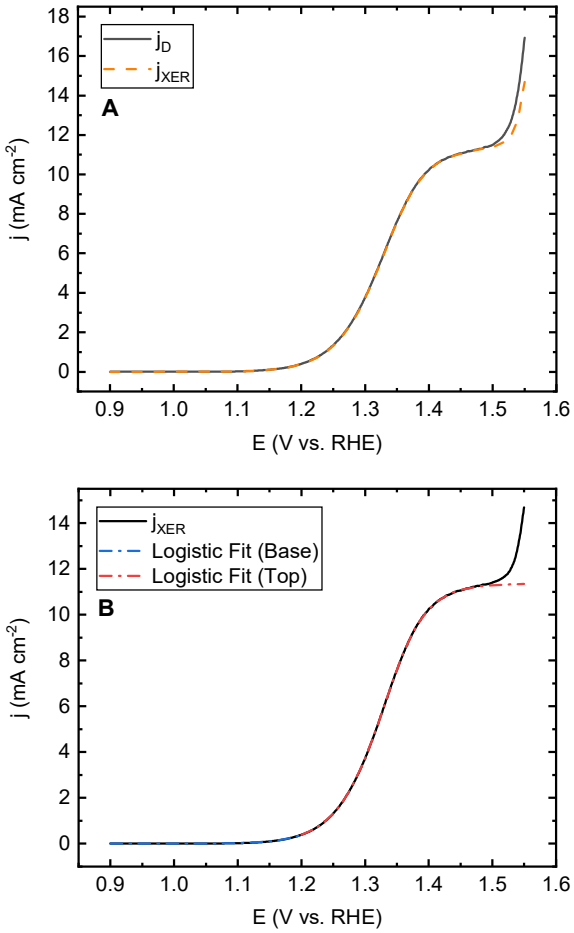

Figure A 9.5.3: Illustration of the method for separating BER, CER and OER currents. A: Comparison of experimental disk current densities (j_D, black solid trace) with halogen evolution currents (j_{XER}, orange dashed trace) which were derived as described in the main text. B: Fits of bromide oxidation in the foot and top of j_{XER} (red and blue dashed traces).

The generalized logistic function was used for both fits, as given by:

$$i_D = i_{L,BOR}^{min} + \frac{i_{L,BOR}^{max} - i_{L,BOR}^{min}}{\left[1 + \left(\frac{E}{x_0}\right)^{-h}\right]^s} \qquad \text{Eq. A 9.5.1}$$

See Figure A 9.4.23 for more information.

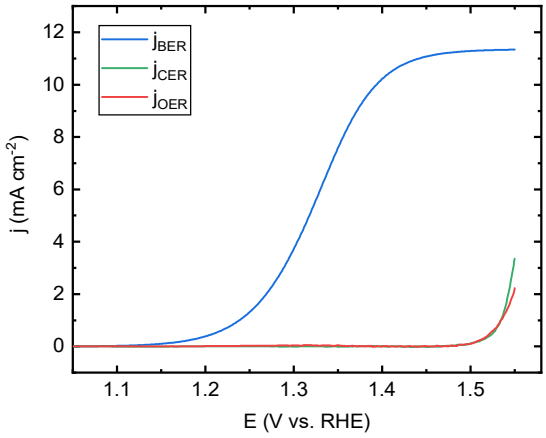

Figure A 9.5.4: Individual BER, CER and OER current densities derived from Figure A 9.5.3.

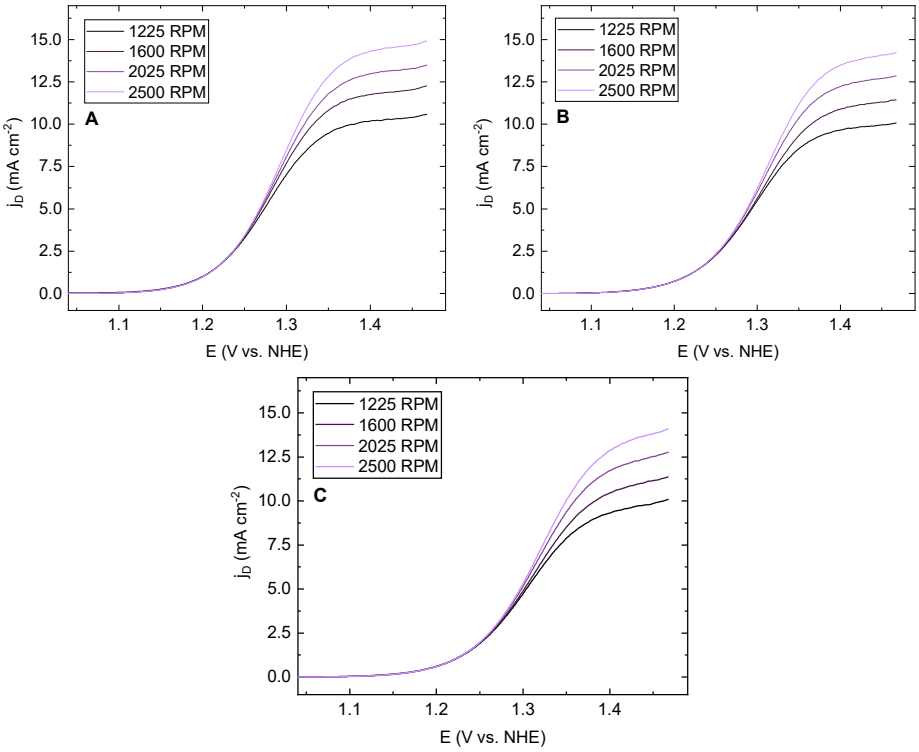

Figure A 9.5.5: Rotation rate dependence of the bromide oxidation region, in 0.5 M $HClO_4$ + 10 mM HBr + (A) 0 mM HCl, (B) 10 mM HCl, (C) 50 mM HCl.

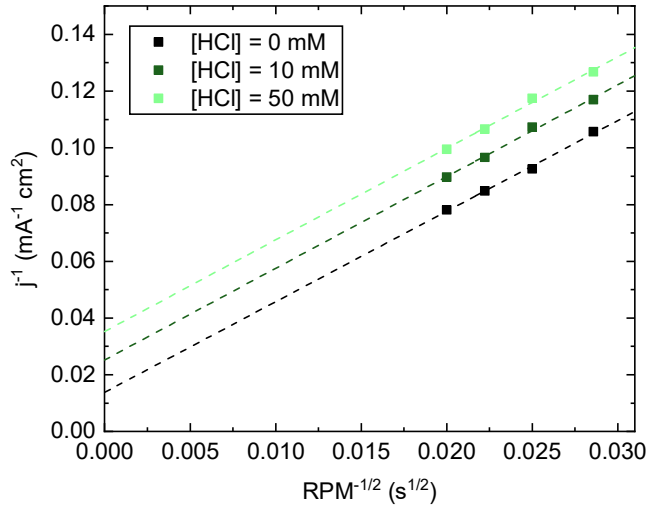

Figure A 9.5.6: Typical examples of Koutecký-Levich plots on the basis of data in Figure A 9.5.5. Shown are data from 1.35 V vs. NHE.

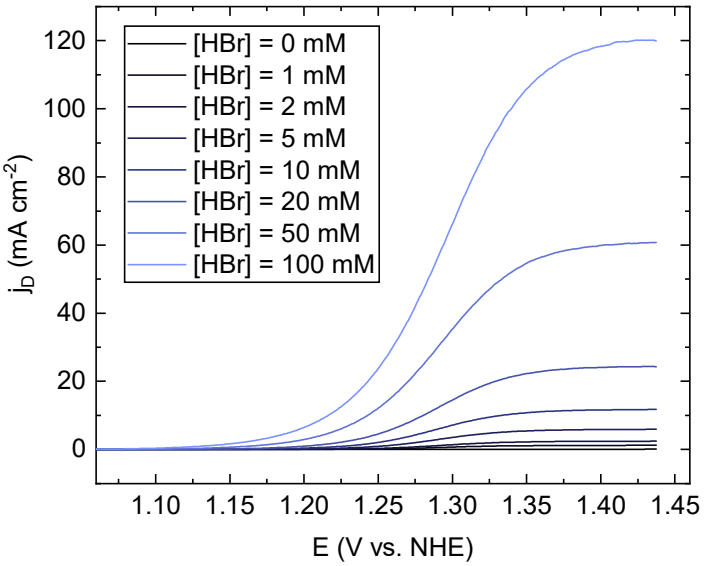

Figure A 9.5.7: Bromine evolution measured under varying [HBr], in 0.5 M $HClO_4$, at 10 mV s^{-1} and 1600 RPM. Only forward scans are shown.

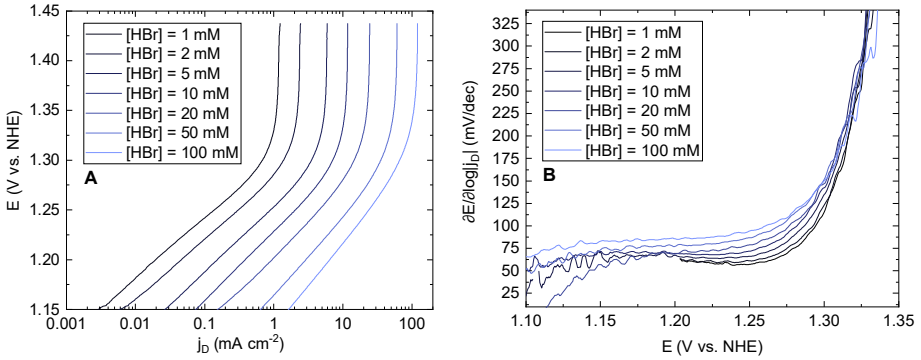

Figure A 9.5.8: Determination of Tafel slopes for bromine evolution. A: Semi-logarithmic plot of Figure A 9.5.7. B: Tafel slopes derived from A, as a function of potential.

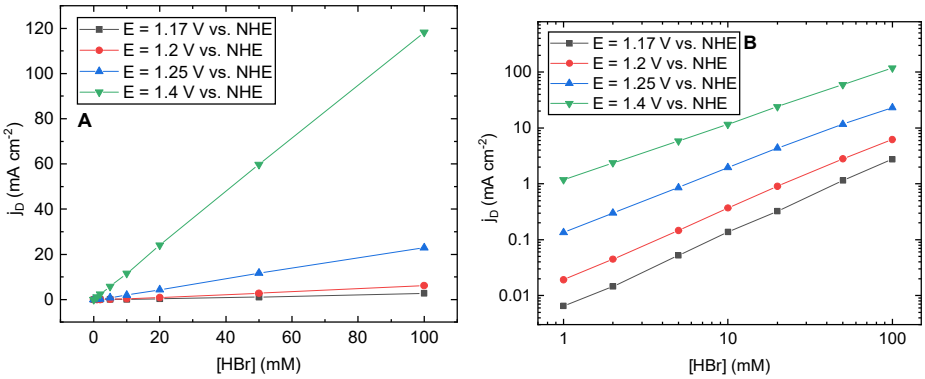

Figure A 9.5.9: Current densities at constant potential values as function of HBr concentration (A), using data shown in Figure A 9.5.7, and corresponding log-log plots (B).

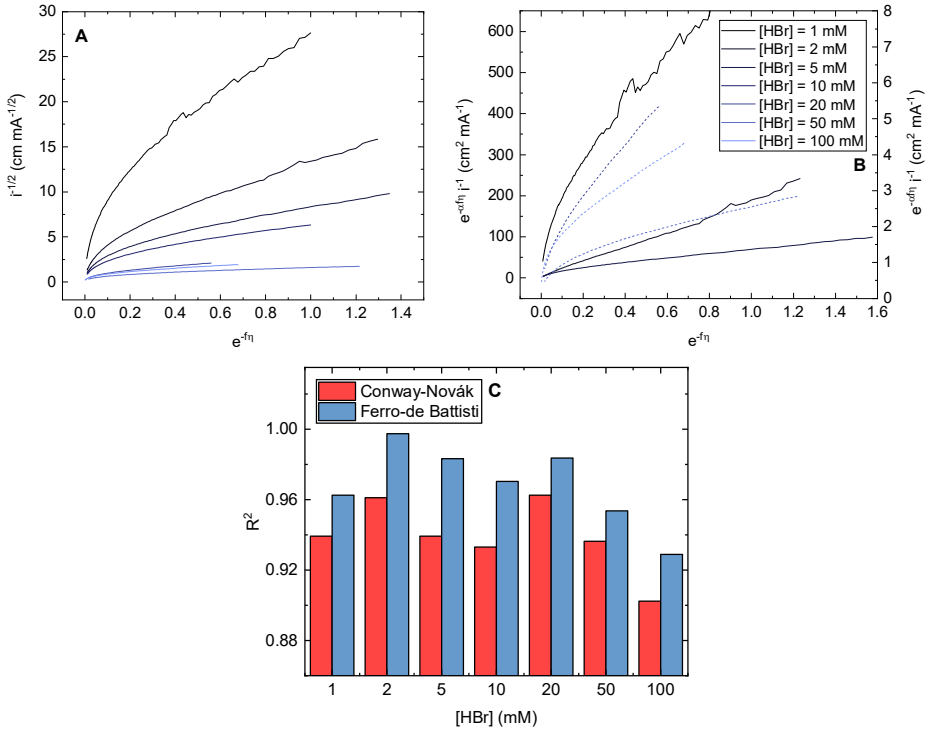

Figure A 9.5.10: Test plots using the methods proposed by Conway and Novák[118] (A) and Ferro *et al.*[113] (B), for the BER. As described in the main text, $\eta = E - E_0$ is the potential relative to a convenient reference, and $f = {}^{F}/_{(RT)}$. In the Ferro-de Battisti plots, α was estimated by observing the unique, non-unitary which results in the most straight line, if any. E_0 was estimated by observing the onset of linearity in E vs. $\log|i|$ plots. C shows the R^2 values obtained from these plots to discern the highest linearity. Values for the three highest [HBr] plots in panel B (dotted traces) are drawn on the right-side y-axis.

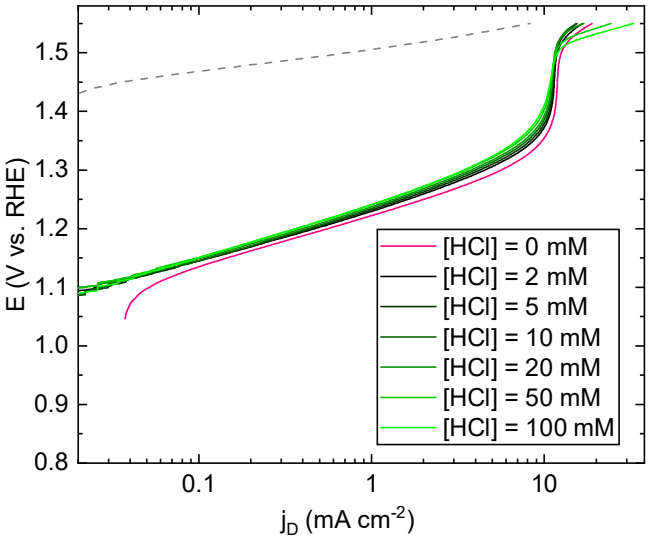

Figure A 9.5.11: Semi-logarithmic plot of Figure 5.1, top panel.

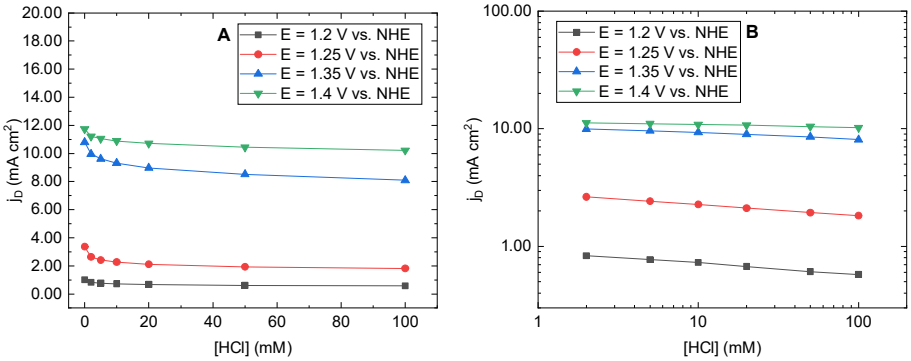

Figure A 9.5.12: Current densities of bromide oxidation at constant potential values as function of HCl concentration (A), using data shown in Figure 5.1, top panel. B: Corresponding log-log plots.

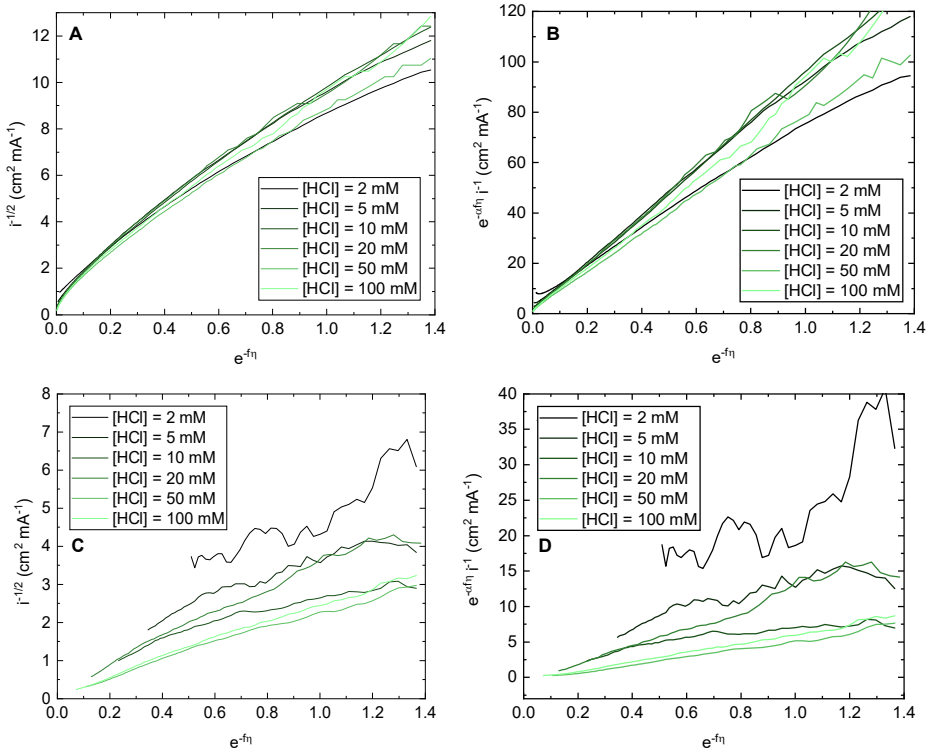

Figure A 9.5.13: Conway-Novák (A, C) and Ferro-de Battisti (B, D) test plots for the CER, as in Figure A 9.5.10. A and B show data for the CER, C and D show data of the CER in presence of 10 mM HBr.

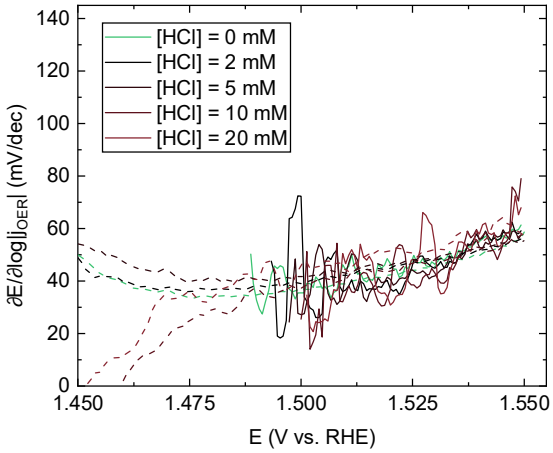

Figure A 9.5.14: OER Tafel slopes measured as function of HCl concentration, in presence of 10 mM HBr (solid traces), and in bromide-free conditions (dotted traces). Data for chloride concentrations higher than 20 mM had insufficient signal to noise ratio and were omitted Green traces show data measured in absence of Cl^- (solid) and in absence of both Cl^- and Br^- (dashed).

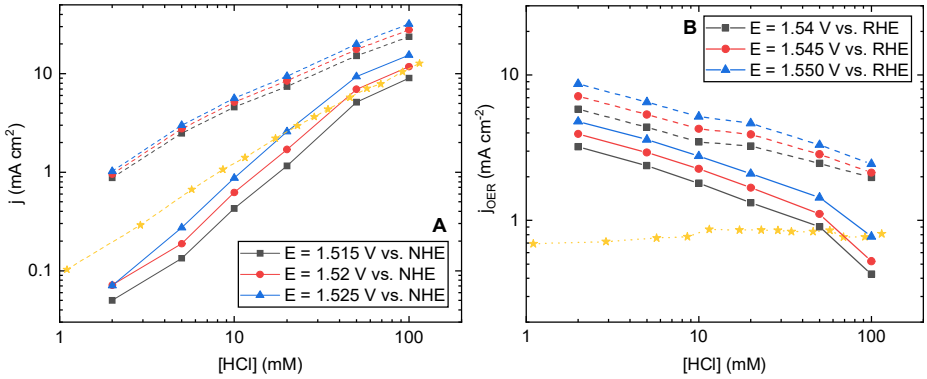

Figure A 9.5.15: Log-Log plots of CER (A) and OER (B) activities measured as function of HCl concentration in 0.5 M $HClO_4$, in presence of 10 mM HBr (solid traces), and in bromide-free conditions (dotted traces). Yellow, dashed trace shows data measured on IrO_x in absence of HBr, in a 0.5 M $KHSO_4$ electrolyte, where $[Cl^-]$ was increased by adding KCl.

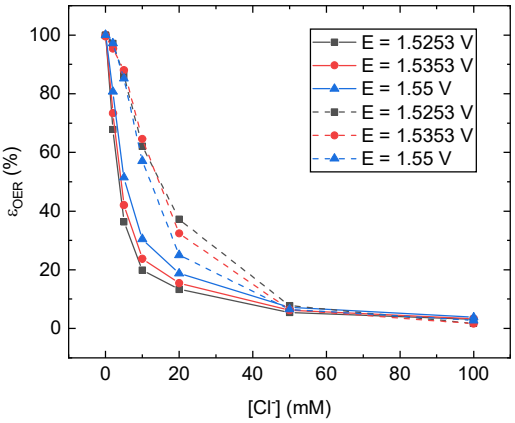

Figure A 9.5.16: Molar selectivities of the OER relative to the CER as function of chloride concentration, in presence (dashed traces) and absence (solid traces) of 10 mM HBr.

9.5.2. Supplementary UV-Vis data

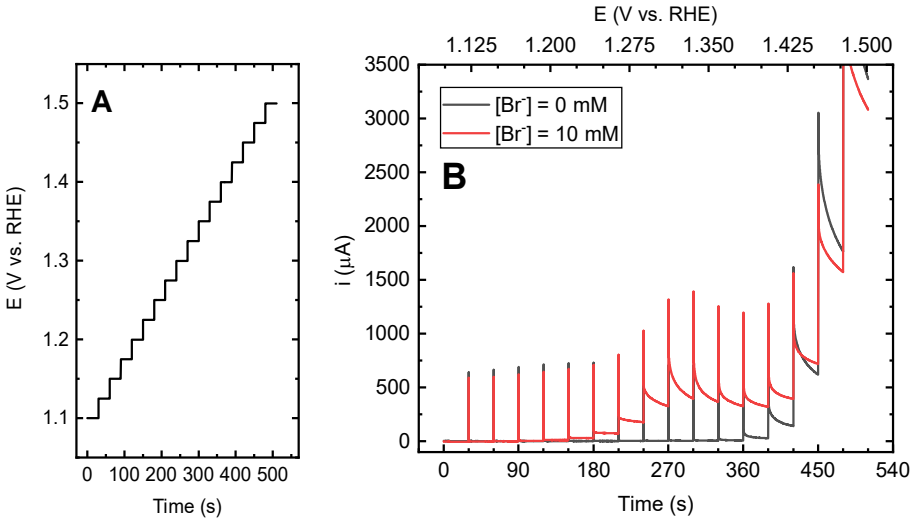

Figure A 9.5.17: E vs. t program used during the UV-Vis experiments (A). Panel B shows full data of Figure 5.4A.

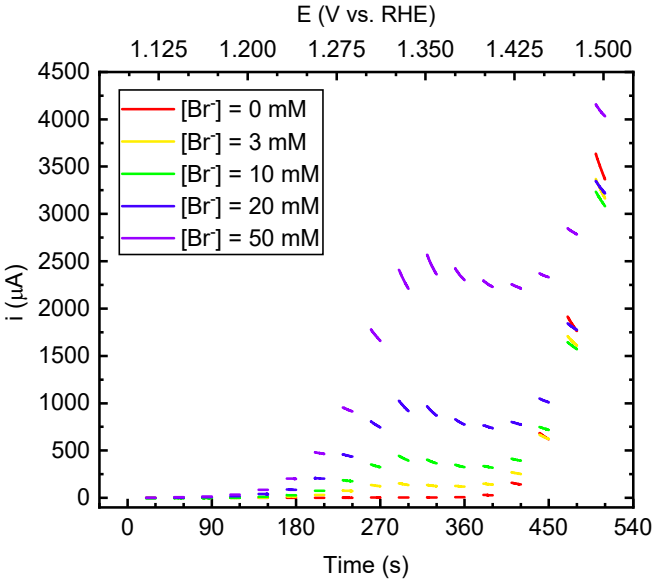

Figure A 9.5.18: Currents measured during UV-Vis experiments in a solution of 0.1 M $HClO_4$ + 0.1 M HCl with [HBr] ranging between 0 and 50 mM. The final 10 s of each potential step are shown.

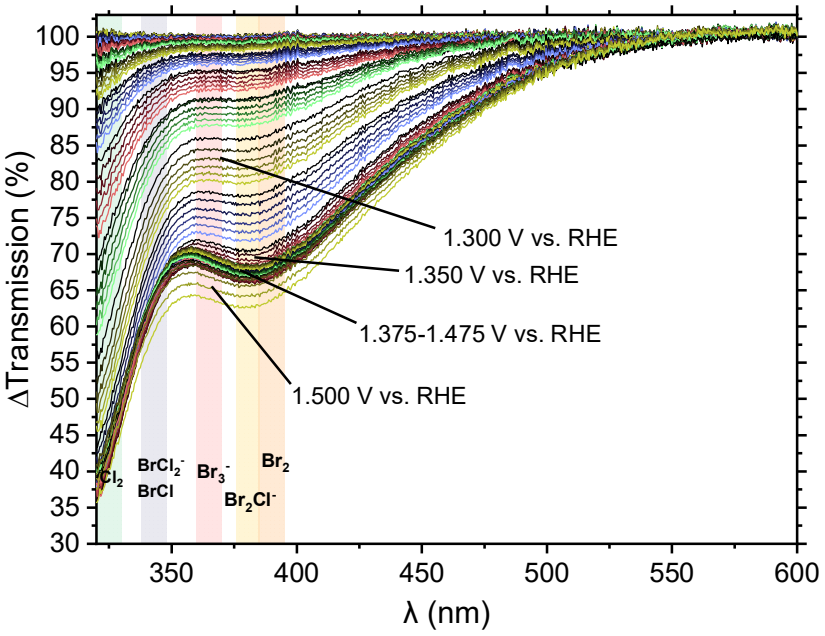

Figure A 9.5.19: Full UV-Vis transmission data similar to Figure 5.4A. Here, [HBr] = 50 mM (corresponding to the purple trace in Figure A 9.5.18).

9.6. Supporting information for Chapter 6

9.6.1. Estimation of the diffusion limiting current of MnO_x deposition

The diffusion limited current of MnO_x deposition at 1500 RPM was determined by means of the equation for the diffusion-limited current:

$$i^L_{MnO_x} = nFA\frac{D_{Mn^{2+}}}{\delta_{Mn^{2+}}}C_{Mn^{2+}} \qquad \text{Eq. A 9.6.1}$$

where $n = 2$ is the number of electrons transferred in the reaction, F is Faraday's constant (96485 C/mol), $D_{Mn^{2+}}$ is the diffusion constant of Mn^{2+} in water ($7.12 \cdot 10^{-10}$ m^2 s^{-1}·), $C_{Mn^{2+}}$ is the species concentration ($[Mn^{2+}] = 0.6$ mol m^{-3}), and $\delta_{Mn^{2+}}$ is the diffusion layer thickness, which is dependent on the rotation rate ω (157.08 rad/s). The latter can be determined via the Levich equation:

$$\delta_{Mn^{2+}} = 1.61\,\nu^{1/6}\,D^{1/3}_{Mn^{2+}}\,\omega^{-1/2} \qquad \text{Eq. A 9.6.2}$$

The value of ν, the kinematic viscosity of the solution, can be estimated at $1.0 \cdot 10^{-6}$ m^2 s^{-1} for dilute ($C < 1$ M) aqueous salt solutions, yielding $i^L_{MnO_x} \approx 140$ µA.

9.6.2. Supplementary electrochemical data

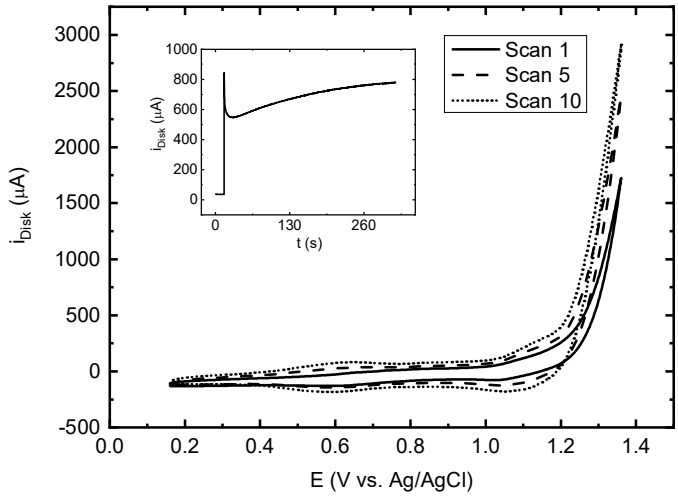

Figure A 9.6.1: Representative CVs of the trends seen during IrO_x electroflocculation, using a IrO_x colloid solution of pH ~ 1 with nominal [Ir] = 2 mM, containing approximately 0.4 M ClO_4^-, 0.3 M Na^+, and 0.012 M Cl^-. The bare GC was initially scanned ten times at 250 mV s^{-1}, during which gradual IrO_x deposition can be observed in the form of increasing CER/OER activity and appearance of IrO_x-related pseudo-capacitance. Amperometry was then performed for 300 s (see inset) at a potential targeted 10 mV more positive than the potential of mixed OER + CER onset (1.255 V vs. Ag/AgCl).

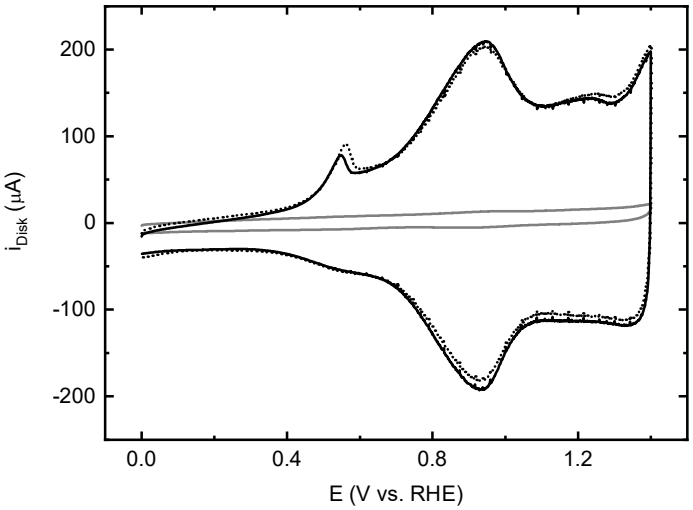

Figure A 9.6.2: Voltammetric characterization of the electroflocculated hydrous IrO_x catalyst (IrO_x/GC), in 0.5 M $KHSO_4$. Electrode is shown in the initial state (solid trace) and after experiments involving mixed OER, CER and MnO_x deposition (dotted trace). Grey trace shows the blank GC support before IrO_x electroflocculation. Scan rate: 50 mV s^{-1}, solution saturated with Ar.

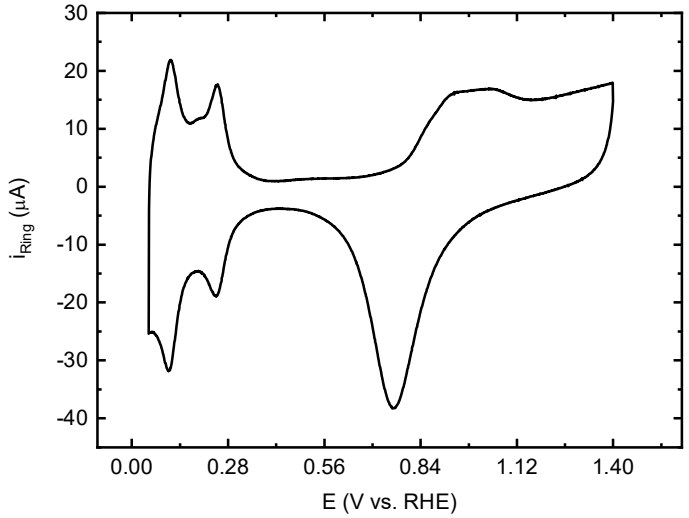

Figure A 9.6.3: Voltammetric characterization of the Pt ring used for chlorine detection, in 0.5 M $KHSO_4$. Scan rate: 50 mV s^{-1}, solution saturated with Ar.

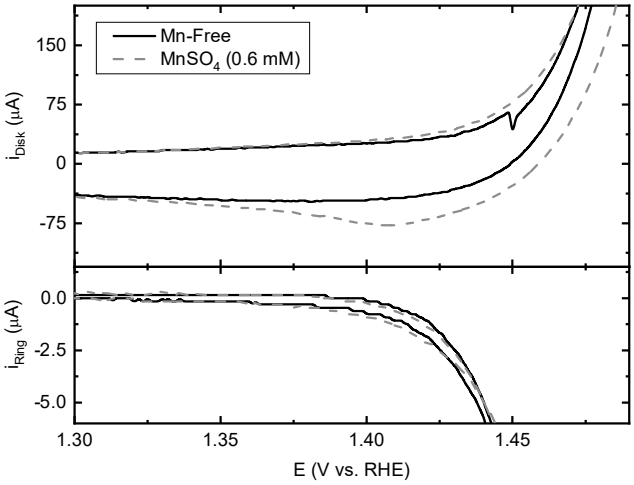

Figure A 9.6.4: Zoom of an IrO_x/GC rotating disk electrode (top) in 0.5 M $KHSO_4$, 30 mM KCl (pH = 0.88), and 0.6 mM $MnSO_4$, showing the electrode behavior (grey dashed trace) compared to a Mn^{2+}-free solution (black trace). The lower figure shows corresponding i_R (E_R = 0.95 V). The slow onset of MnO_x deposition is visible near 1.37 V, and is coupled to the onset of superimposed reduction current on the ring, at a potential lower than the onset of chlorine reduction. Rotation rate 1500 RPM, solution saturated with Ar, i_R was corrected for collection delay.

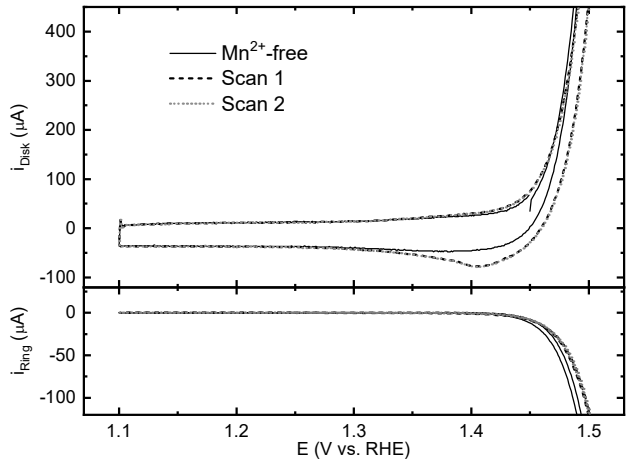

Figure A 9.6.5: CVs of an IrO_x/GC rotating disk electrode (top) in 0.5 M $KHSO_4$, 30 mM KCl (pH = 0.89), and 0.6 mM $MnSO_4$. The electrode was cycled multiple times between 1.1 V and 1.55 V, two successive scans are shown (black and grey dashed thick traces). Strong overlapping of the scans show reproducibility of MnO_x deposition-dissolution behavior during scans. Minor MnO_x reduction current can be seen as a broad peak near 1.42 V in the backward scans. The thin black trace shows the IrO_x/GC electrode in a Mn^{2+}-free solution. The lower figure shows corresponding i_R (E_R = 0.95 V). Rotation rate 1500 RPM, solution saturated with Ar, i_R was corrected for collection delay.

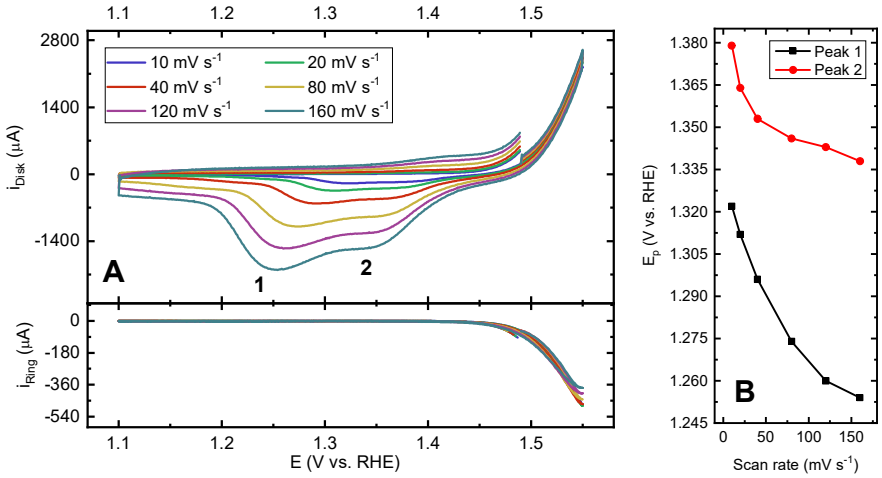

Figure A 9.6.6: (A) CVs of an IrO_x/GC rotating disk electrode (top) in 0.5 M $KHSO_4$, 30 mM KCl (pH = 0.91), and 0.6 mM $MnSO_4$. MnO_x films were preconditioned for 300 s at 1.49 V before initiating the forward scan at 1.49 V, with variable scan rate. Charges obtained during preconditioning (and hence the corresponding Q_{MnO_x}) showed a maximum variance of approximately 10%. The lower figure shows corresponding i_R (E_R = 0.95 V). Rotation rate 1500 RPM, solution saturated with Ar, i_R was corrected for collection delay. (B) Scan rate vs. peak reduction potentials of peak 1 and peak 2, in the MnO_x films of panel A.

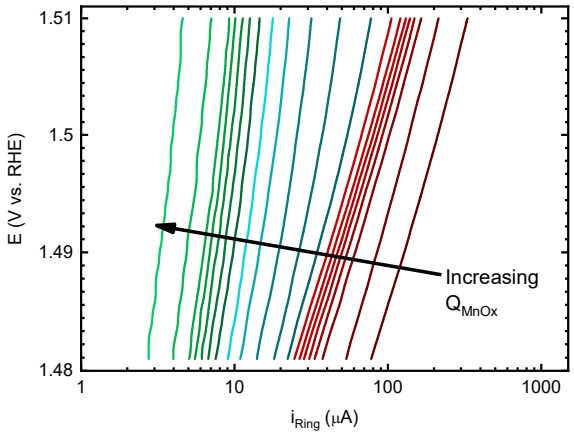

Figure A 9.6.7: Full Tafel plots for CER on the disk electrode, constructed from ring currents. No correction for N_l was applied as in Figure 6.3 in the main text. Data were measured on the Pt ring (E_R = 0.95 V) in combination with an IrO_x/GC rotating disk electrode in 0.5 M $KHSO_4$, 30 mM KCl (pH = 0.88), and 0.6 mM $MnSO_4$ (except for the Mn^{2+}-free experiment). MnO_x films were preconditioned at various times at 1.48 V before initiating the forward scan at 1.48 V. Plots are drawn in three color regimes, with increasing MnO_x reductive charge within each regime: 0 mC < Q_{MnO_x} < 2 mC (red), : 2 mC < Q_{MnO_x} < 4 mC (blue) and Q_{MnO_x} > 4 mC (green). Disk scan rate: 10 mV s^{-1}, rotation rate 1500 RPM, solution saturated with Ar, i_R was corrected for collection delay.

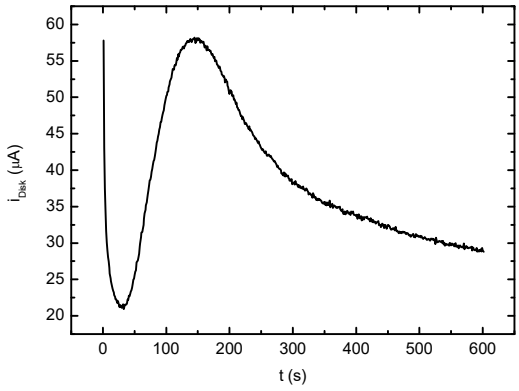

Figure A 9.6.8: Representative deposition curve of MnO_x in an acidic ClO_4^- solution. Data shown of amperometry of an IrO_x/GC electrode at 1.45 V, in a solution containing 0.5 M $Na/HClO_4$ (pH = 0.85) and 0.6 mM $Mn(ClO_4)_2$. Rotation rate 1500 RPM, solution saturated with Ar. The curve shows behavior strongly reminiscent of a progressive nucleation and growth mechanism. A non-adsorbing ClO_4^- solution was used instead of HSO_4^-, as this allowed observation of MnO_x deposition at intermediate rates at lower potentials, without the complication of superimposed OER.

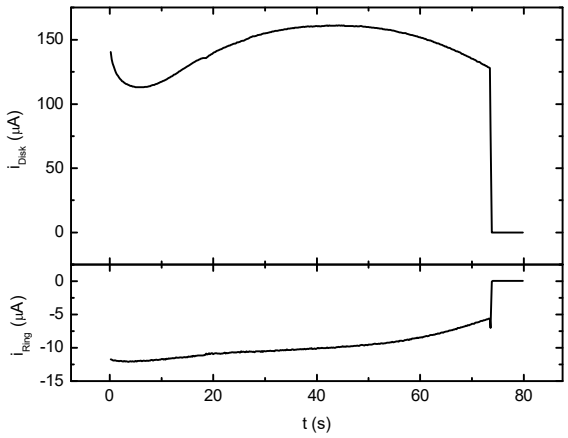

Figure A 9.6.9: Amperometry of an IrO_x/GC electrode (top) at 1.21 V vs. Ag/AgCl, in 0.1 M $HClO_4$ (pH ≈ 0.85) and 0.6 mM $Mn(ClO_4)_2$, representative of sample preparation for structural studies. The lower figure shows corresponding i_R (E_R = 0.71 V vs. Ag/AgCl). The deposition cut-off point can be seen at t = 73 s, where the electrode contact with the solution was interrupted. At that point, CER rates (as determined from i_R) were approximately 50% of their original value, and approaching the dramatic activity drop. Rotation rate 1500 RPM, solution saturated with Ar.

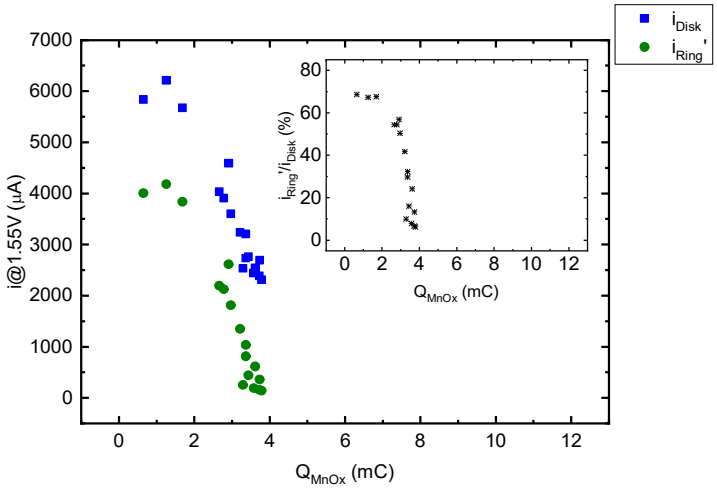

Figure A 9.6.10: Plot of disk currents (blue), ring currents (green), and ratio between i_R' and i_D (inset) measured at E_D = 1.55 V as function of Q_{MnO_x}, the reductive charge measured for the corresponding MnO_x film during the backward scan. Values determined in a 0.15 M $HClO_4$ + 0.35 M $NaClO_4$ solution (pH = 0.88).

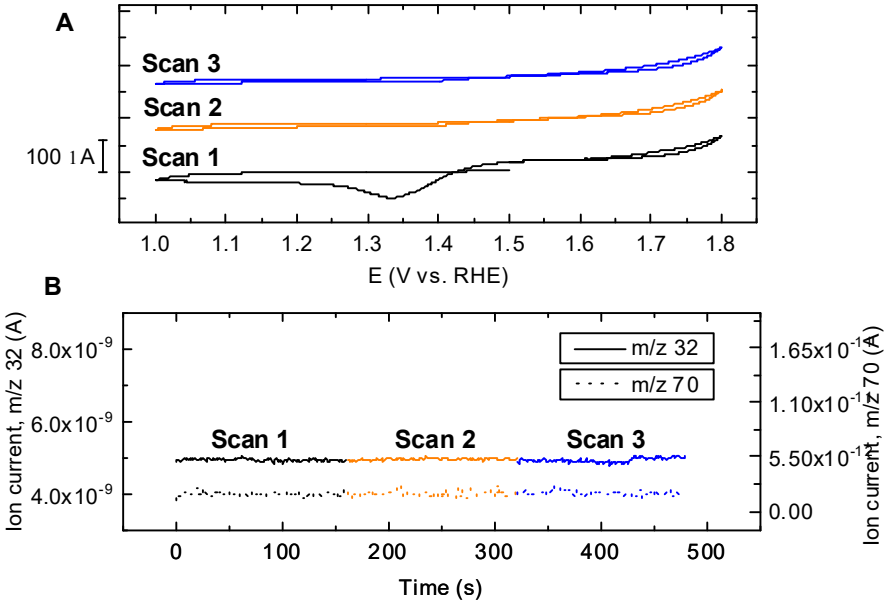

Figure A 9.6.11: OLEMS measurements of a MnO_x/GC electrode in 0.5 M $KHSO_4$, 20 mM KCl, and 1.2 mM $MnSO_4$ (pH = 0.84). A: CVs of the electrode after preconditioning for 900 s at 1.50 V, followed by three scans. Scan rate: 5 mV s^{-1}. C shows corresponding OLEMS mass signals over time. Solution saturated with Ar.

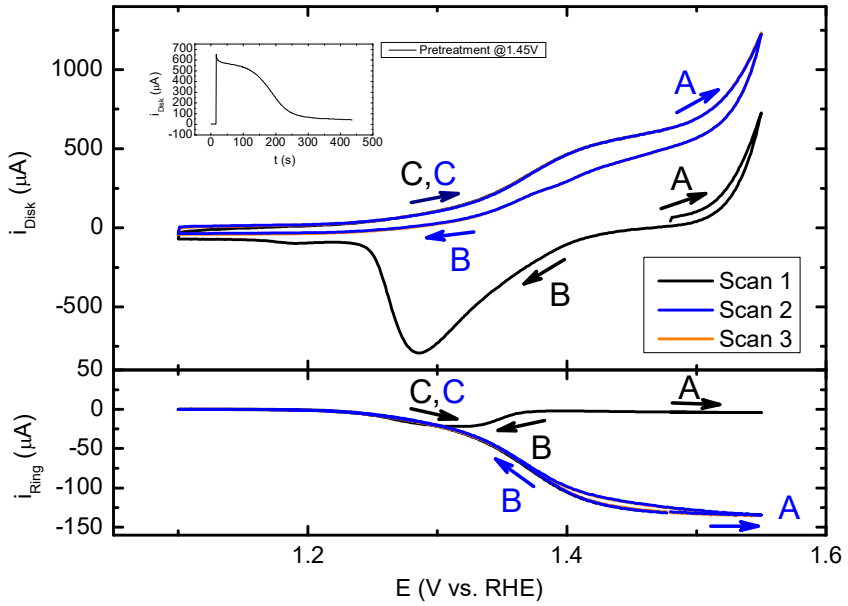

Figure A 9.6.12: CVs of an IrO_x/GC rotating disk electrode (top) in 0.5 M $KHSO_4$, 3 mM KBr (pH = 1.15), and 0.6 mM $MnSO_4$. The lower figure shows corresponding i_R (E_R = 0.90 V). Fixing the ring potential at 0.90 V allowed measurement of BER rates via selective reduction of Br_2 and Br_3^- back to Br^-. A MnO_x film was grown for 420 s at 1.45 V (see inset for current profile) before initiating the forward scan (black trace) at 1.45 V. Scan rate 10 mV s^{-1}, rotation rate 1500 RPM.

Several MnO_x-related shifts in behavior are visible, marked A, B and C. At the beginning of the first scan at 1.45 V (A, black) a MnO_x film is present, resulting in mainly OER-related current on the disk (onset near 1.45 V) and almost no ring current related to bromine reduction. In the backward scan, the MnO_x film starts dissolving near 1.45 V (B, black), coinciding with a rise in ring current as BER rates increase. Due to the backward scanning potential, BER rates on the ring decrease quickly after their rise. Resuming the forward direction after crossing the 1.10 V lower potential limit, the IrO_x/GC electrode is MnO_x-free, which is apparent from a rise in current near 1.20 V (C, black), corresponding to onset of BER. As the potential is scanned higher than 1.45 V, crossing into the second scan (A, blue), the disk current is composed of bromine evolution and the onset of OER. The ring shows significant bromine reduction current, approaching near diffusion limited BER rates on the disk. There is also minor hysteresis in the ring current during scan reversal, currents decrease over time due to transient MnO_x growth. In absence of an integral MnO_x film, the remainder of the second scan (B and C, blue) shows simply the decrease in OER and BER. Scan 3 (orange trace) overlapped strongly with scan 2.

A more elaborate study of the effect of MnO_x on BER selectivity was not pursued, since it is outside the scope of this thesis. The nature of bromine evolution is substantially different from CER,[196] and a more detailed study would require a different experimental approach.

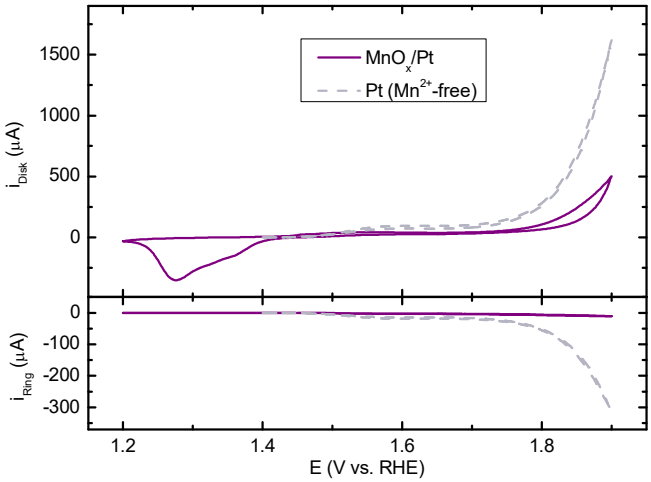

Figure A 9.6.13: CVs of a Pt rotating disk electrode (top) in 0.5 M $KHSO_4$, 100 mM KCl (pH = 1.37), and 0.6 mM $MnSO_4$. A MnO_x film was preconditioned for 300 s at 1.45 V before initiating the forward scan at 1.45 V (purple trace). Grey dashed trace shows Pt in Mn^{2+}-free conditions for comparison. The lower figure shows corresponding i_R (E_R = 0.95 V). Scan rate: 10 mV s^{-1}, Rotation rate 1500 RPM.

9.6.3. XRD data

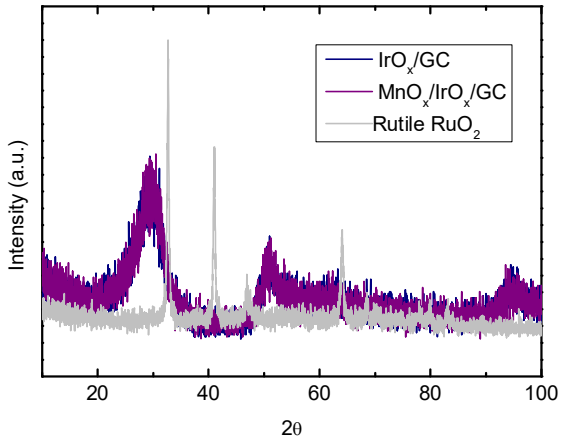

Figure A 9.6.14: XRD data of IrO_x/GC and MnO_x/IrO_x/GC samples. Data of highly crystalline commercial rutile-RuO_2 was added for comparison, using a small mass loading of similar magnitude as the metal oxides on the GC disk samples (rutile-RuO_2 has lattice parameters almost identical to rutile-IrO_2). The broad amorphous peaks near 2θ ≈ 30, 50 and 94 may originate from the GC substrate.

9.6.4. Supplementary microscopy data

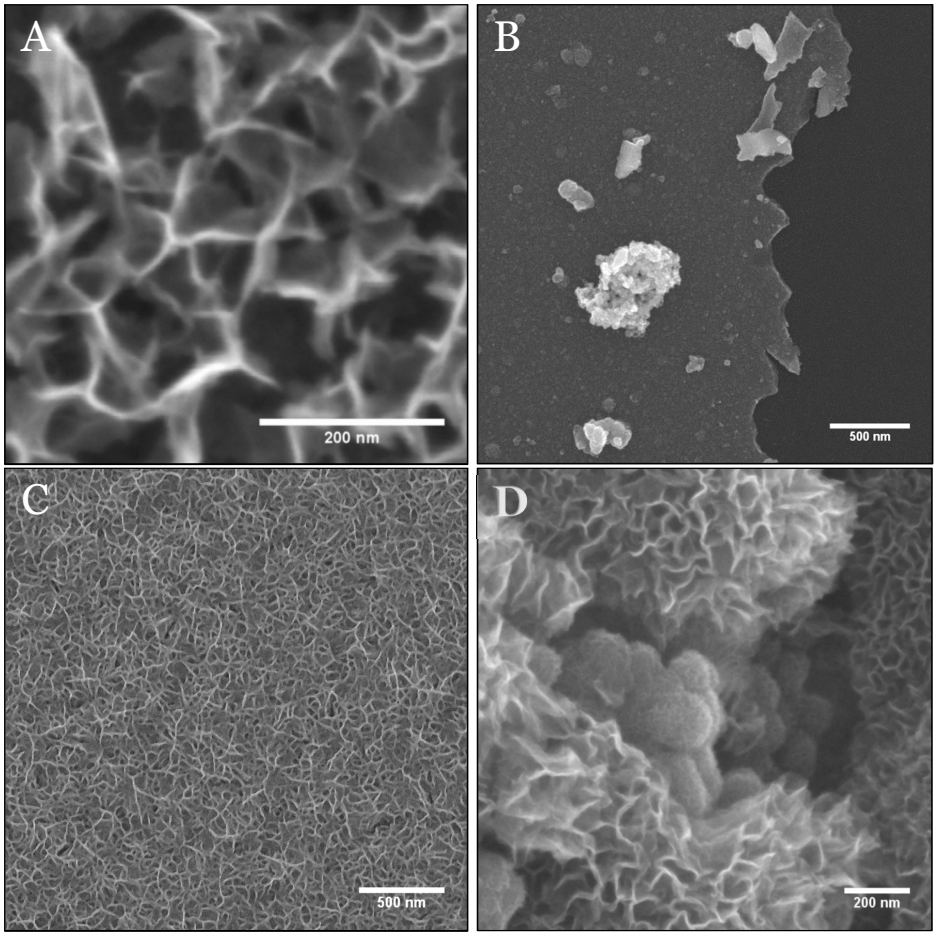

Figure A 9.6.15: Supplementary SEM images. A: Zoom of MnO_x structure as-deposited on IrO_x/GC. B: IrO_x/GC sample showing the 'smooth' IrO_x layer with nanosized IrO_x colloid clusters on top, and bare GC (right). C: Structure of MnO_x deposited on bare GC (no IrO_x present). D: MnO_x deposited onto IrO_x for extended deposition times (a 'thick' film). An IrO_x cluster is shown. Some IrO_x nanoparticles are still visible, covered by a thin layer of MnO_x sheets as described previously. Larger MnO_x formations with thicker sheets can also be seen, often completely obscuring the IrO_x underneath.

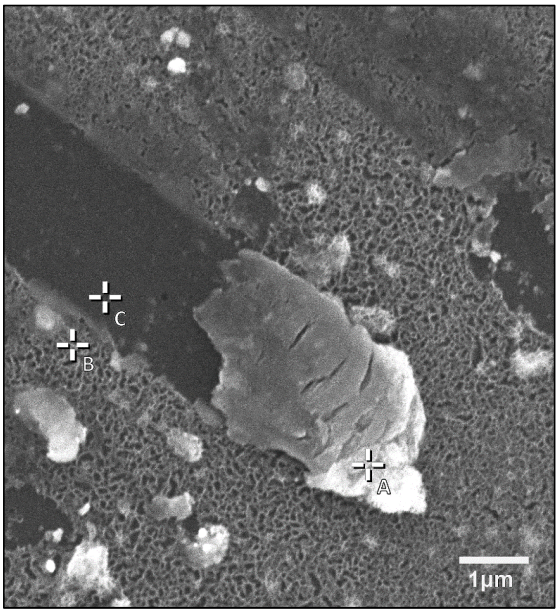

Figure A 9.6.16: MnO_x/IrO_x film used for EDS analysis.

Table A 9.6.1: EDS data from points in Figure A 9.6.16.

	Point A		Point B		Point C	
Element	mass%	Atom%	mass%	Atom%	mass%	Atom%
C	74.46	0.03	93.89	0.04	95.85	0.04
O	21.36	0.09	5.73	0.08	4.15	0.07
Mn	3.98	0.12	0.38	0.06	-	-
Ir	0.2	0.08	-	-	-	-

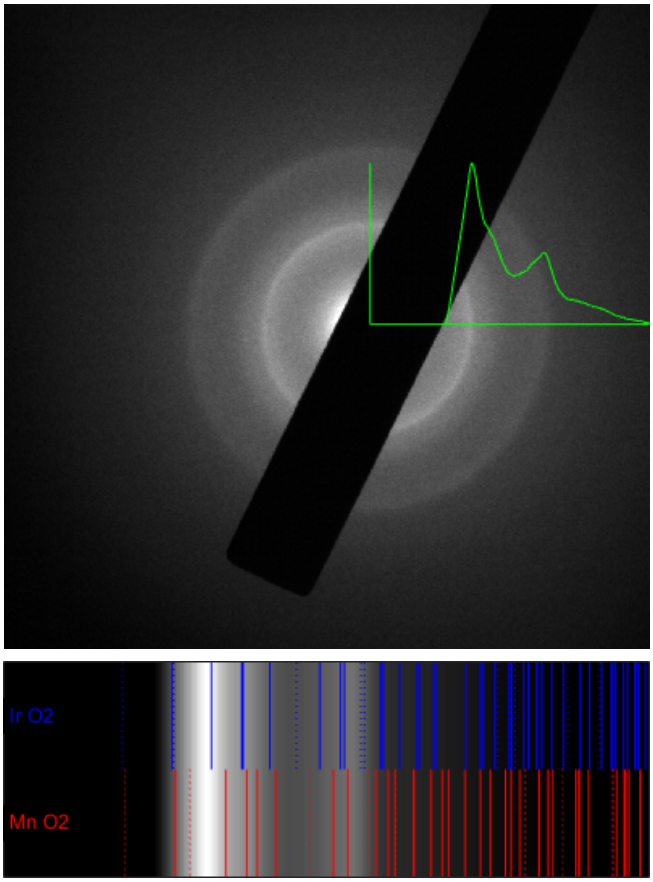

Figure A 9.6.17: SAED pattern and corresponding linear diffractogram of a MnO_x/IrO_x/GC sample (accelerating voltage of 120 kV). Predicted rutile-IrO_2 and β-MnO_2 (pyrolusite) patterns shown as reference.

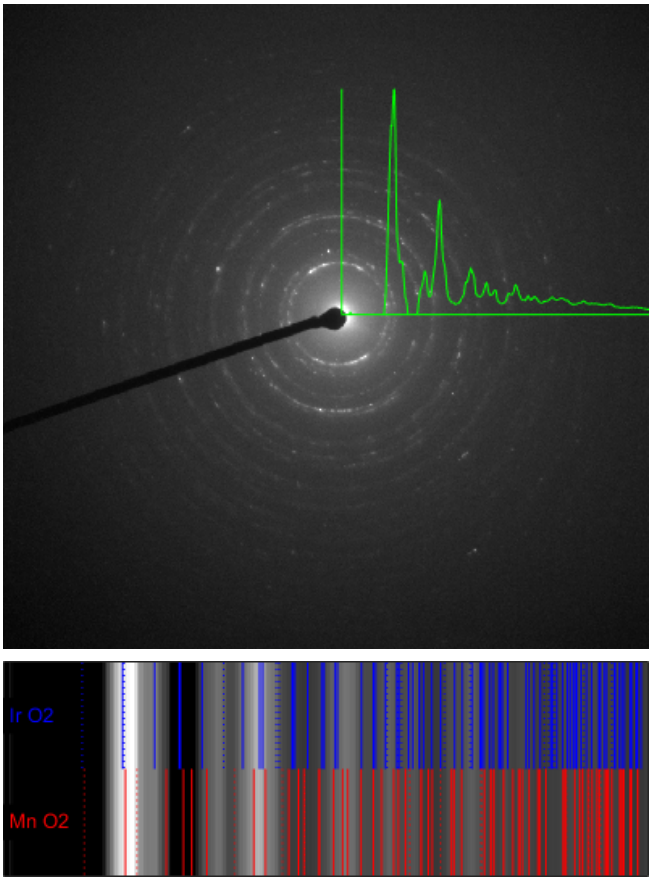

Figure A 9.6.18: SAED pattern and corresponding linear diffractogram of a MnO_x/IrO_x/GC sample at higher accelerating voltage (200 kV). Predicted rutile-IrO_2 and β-MnO_2 (pyrolusite) patterns shown as reference.

9.6.5. Supplementary XPS data

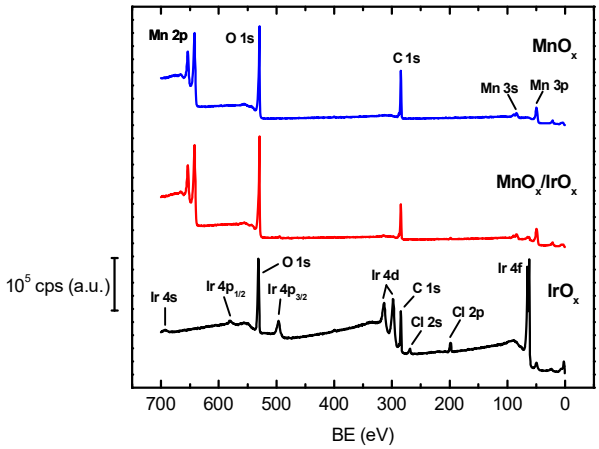

Figure A 9.6.19: Survey spectra of the of Mn and Ir MO_x/GC single oxides (top and bottom) and the mixed MnO_x/IrO_x/GC sample (middle).

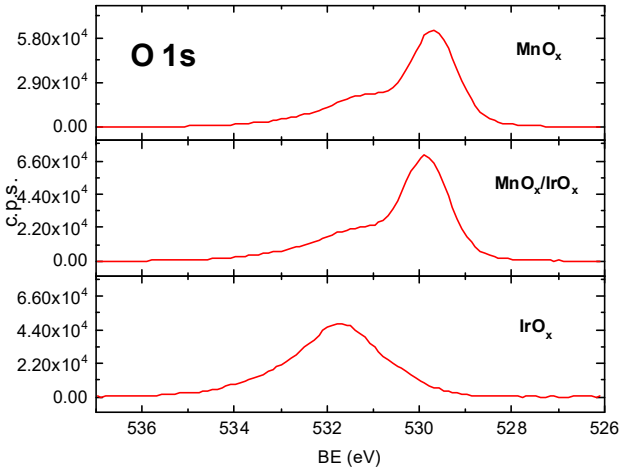

Figure A 9.6.20: Core-level XPS scans of the O 1s spectral peaks on an absolute intensity scale. Scans were made of Mn and Ir MO_x/GC single oxides (top and bottom) and the mixed MnO_x/IrO_x/GC sample (middle).

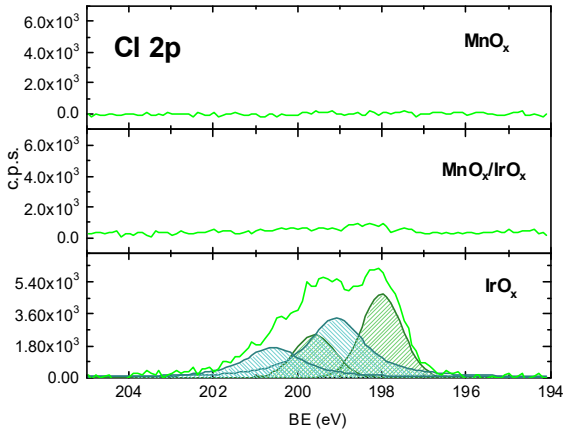

Figure A 9.6.21: Core-level XPS scans of the Cl 2p spectral peaks on an absolute intensity scale. Scans were made of Mn and Ir MO_x/GC single oxides (top and bottom) and the mixed MnO_x/IrO_x/GC sample (middle). The IrO_x/GC sample shows Cl contributions related to Ir-Cl (binding energy 199.1 eV) and alkali-metal chloride (binding energy 198.0 eV).

Table A 9.6.2: Mn:Ir atom ratios in the XPS MnO_x/IrO_x/GC sample, determined from XPS and from charge integration from the corresponding amperometry during sample preparation.

	XPS	Amperometry
Mn	**43**	**2**
Ir	**1**	**1**

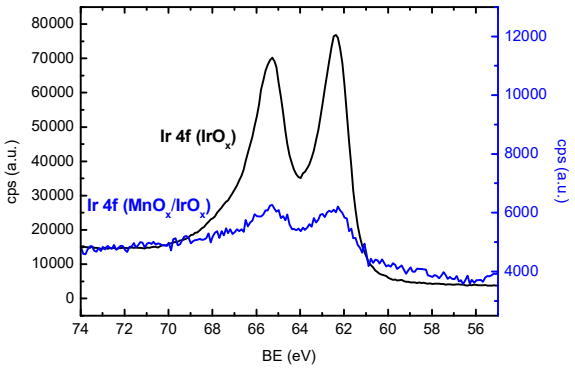

Figure A 9.6.22: Ir 4f core-level spectra without background correction, comparing IrO_x/GC and MnO_x/IrO_x/GC samples. The ratio (peak height) : (difference of background intensity) is ~0.16 and ~0.37 for IrO_x/GC and MnO_x/IrO_x/GC, respectively.

9.7. Supporting information for Chapter 7

9.7.1. Supplementary voltammetry data

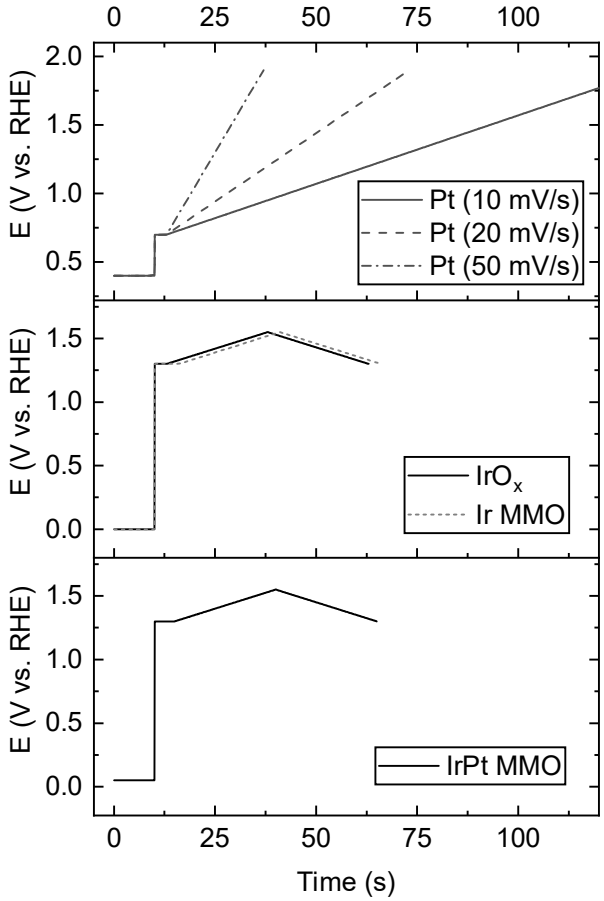

Figure A 9.7.1: E vs. t programs used during the various experiments involving parallel oxygen and chlorine evolution.

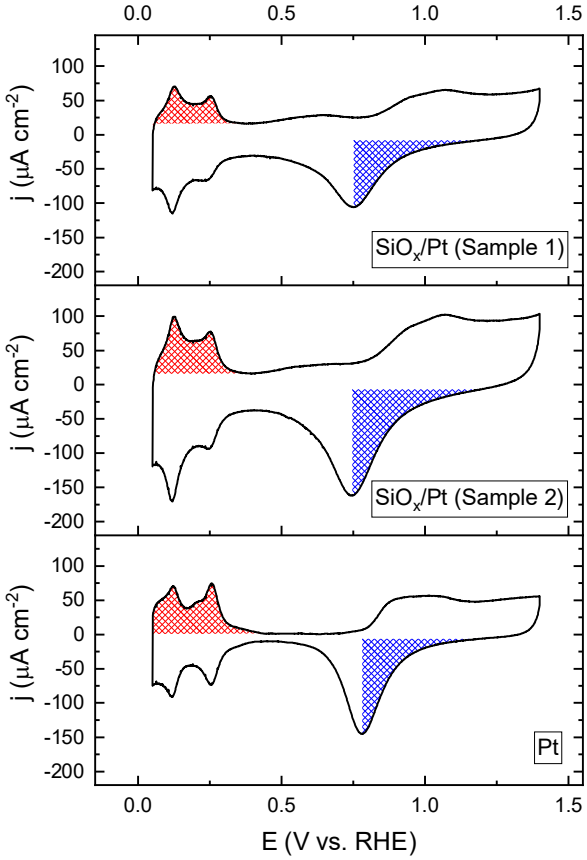

Figure A 9.7.2: Voltammetric characterizations of SiO_x/Pt and Pt electrodes, in 0.5 M $KHSO_4$, recorded at 50 mV s^{-1}. Charge regions used for comparing hydrogen desorption and PtO_x reduction are illustrated in red and blue, respectively.

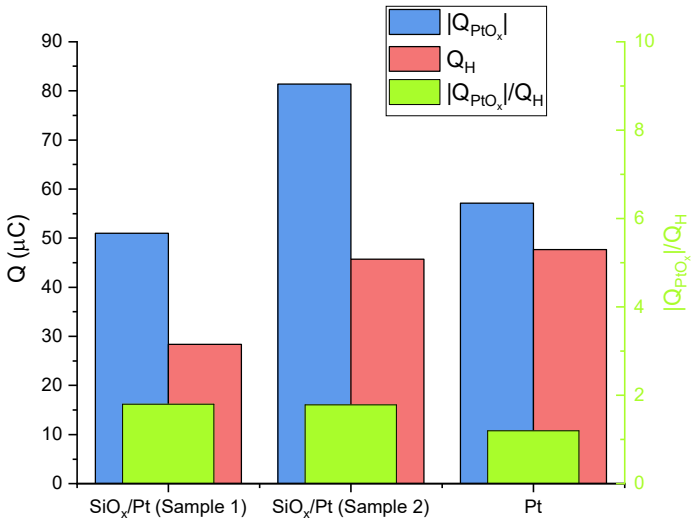

Figure A 9.7.3: Comparison of Q_H and Q_{PtO_x}, the charges corresponding to hydrogen desorption and PtO_x reduction, respectively. Green bars (values on right axis) show the charge ratios. Data derived from highlighted areas in Figure A 9.7.2.

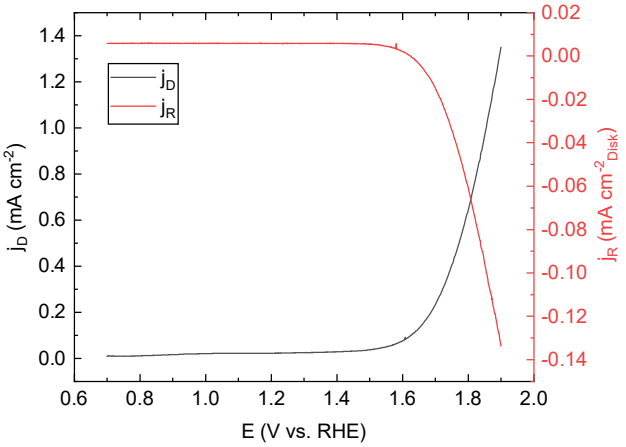

Figure A 9.7.4: Linear RRDE scan on a SiO_x/Pt/Ti/GC electrode (Sample 1), recorded at 10 mV s^{-1} in 0.5 M $KHSO_4$. The ring potential was fixed at 0.4 V, so that O_2 is detected.

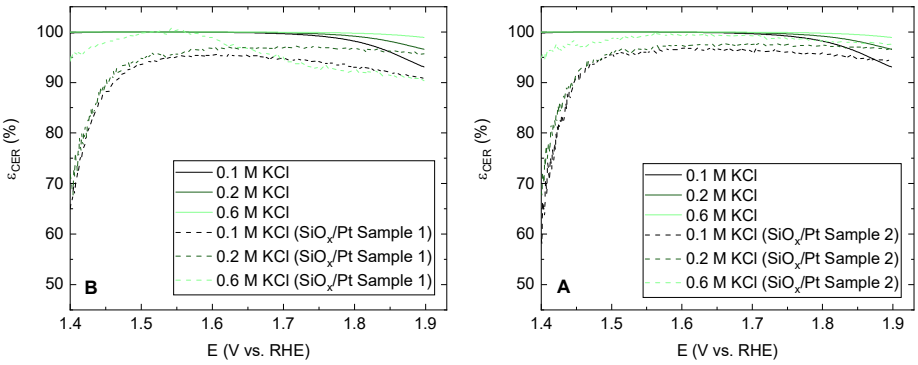

Figure A 9.7.5: Molar CER selectivities versus potential for two SiO_x/Pt/Ti/GC electrodes (dotted lines in A and B). Data is shown for three different chloride concentrations, and compared with the bare Pt surface (solid lines). Data for the bare Pt surface were estimated from OER data in absence of chloride.

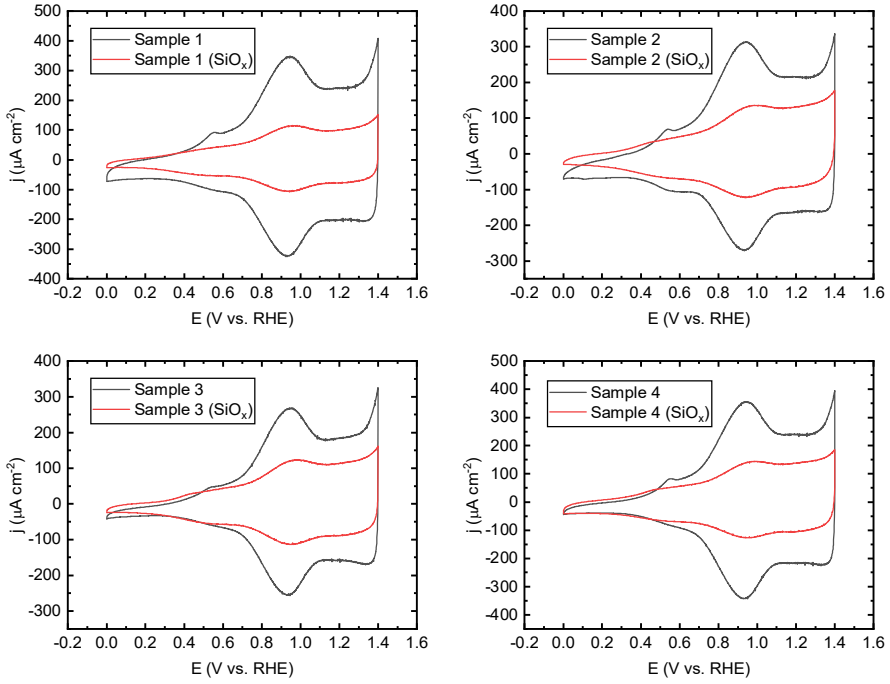

Figure A 9.7.6: Voltammetric characterization of IrO_x/GC samples, before and after the SiO_x coating.

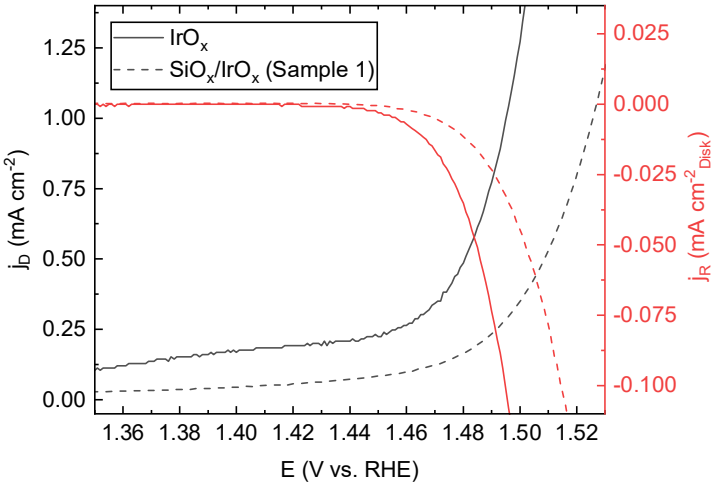

Figure A 9.7.7: Collection experiment of O_2 on an IrO_x/GC and an SiO_x/IrO_x/GC samples, as in Figure A 9.7.4.

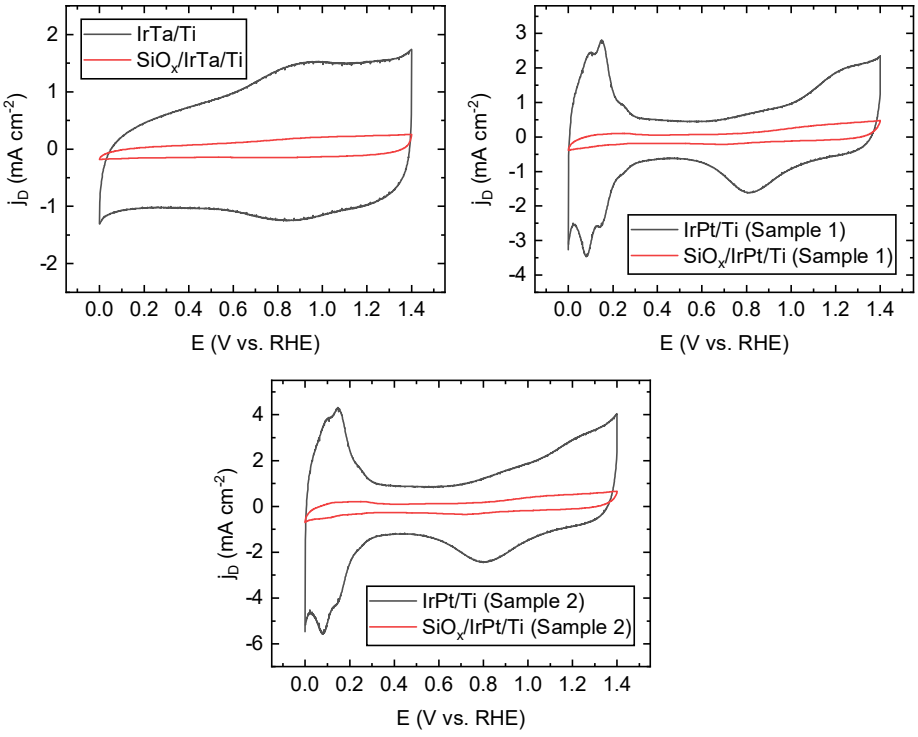

Figure A 9.7.8: Voltammetric characterization of Ti-based anodes, before and after the SiO_x coating.

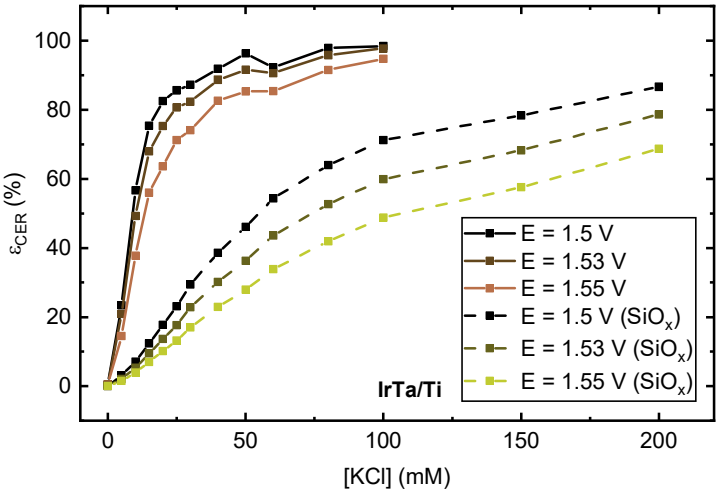

Figure A 9.7.9: Molar selectivity towards the CER as function of chloride concentration for an IrTa/Ti sample, similar to Figure 7.8 in the main text.

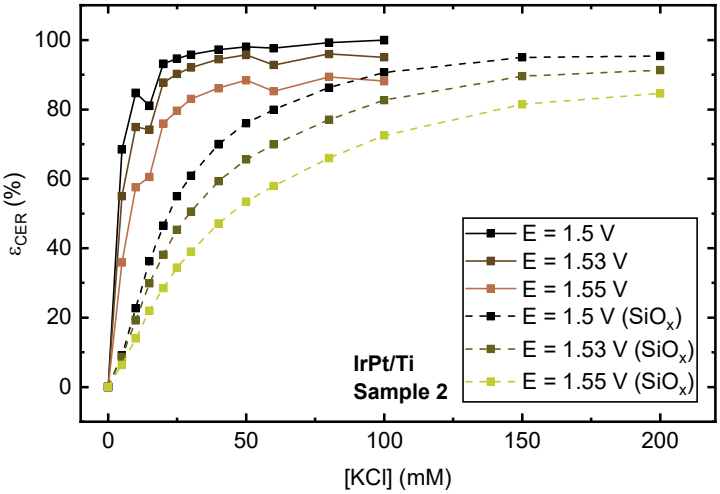

Figure A 9.7.10: Molar selectivity towards the CER as function of chloride concentration for an IrPt/Ti sample, similar to Figure 7.8 in the main text.

9.7.2. *Kinetic OER and CER data*

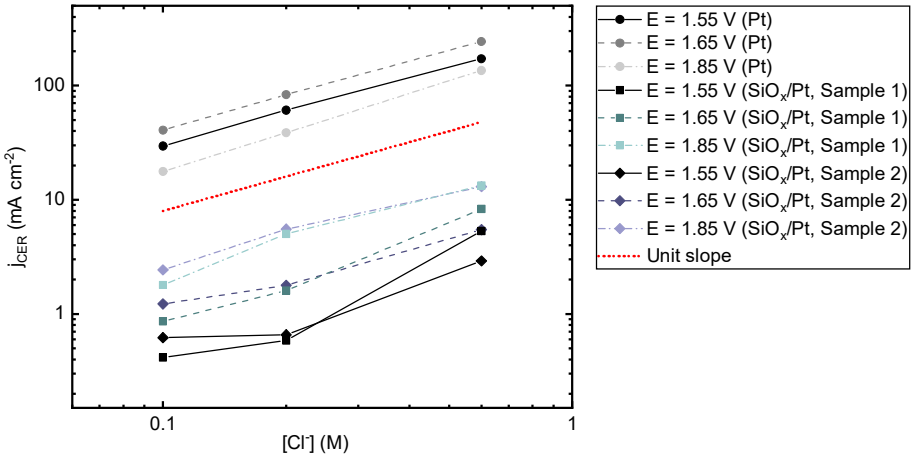

Figure A 9.7.11: Log-log plot of derived CER current densities on various Pt samples, as function of chloride concentration. Data is displayed for three different potentials. Red dotted line shows a reaction order of one (unit slope).

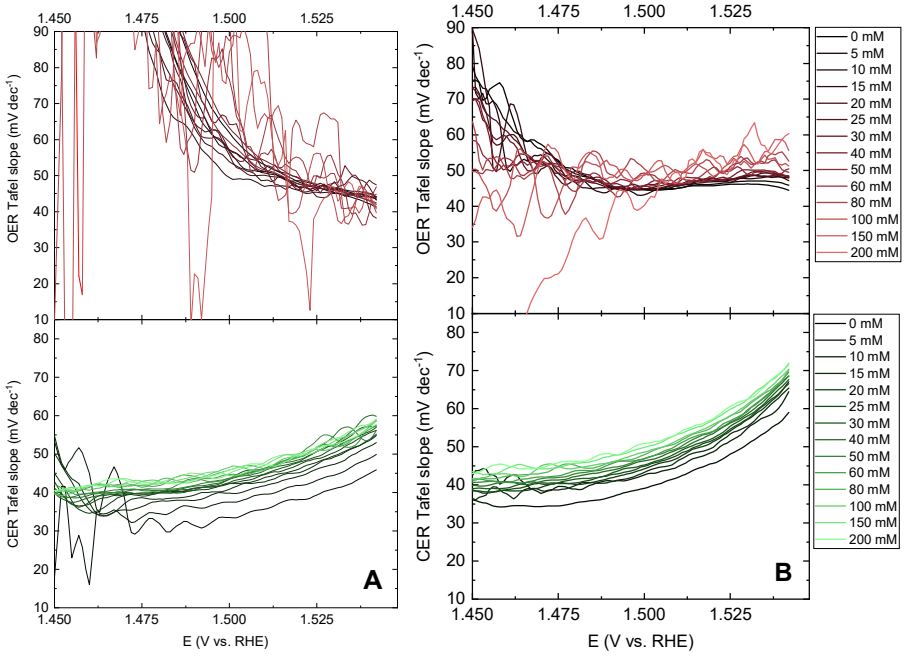

Figure A 9.7.12: Derived Tafel slopes of CER and OER current densities versus potential, on an IrO_x/GC sample and an SiO_x/IrO_x/GC sample (A and B respectively). Values are shown for KCl concentrations ranging between 0 – 200 mM.

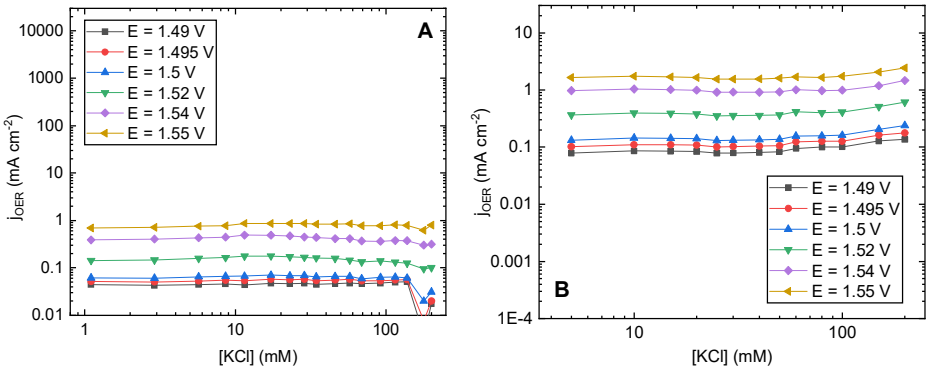

Figure A 9.7.13: Log-log plot of derived OER current densities on an IrO_x/GC sample and a SiO_x/IrO_x/GC sample (A and B respectively). Data is displayed for a series of different potentials.

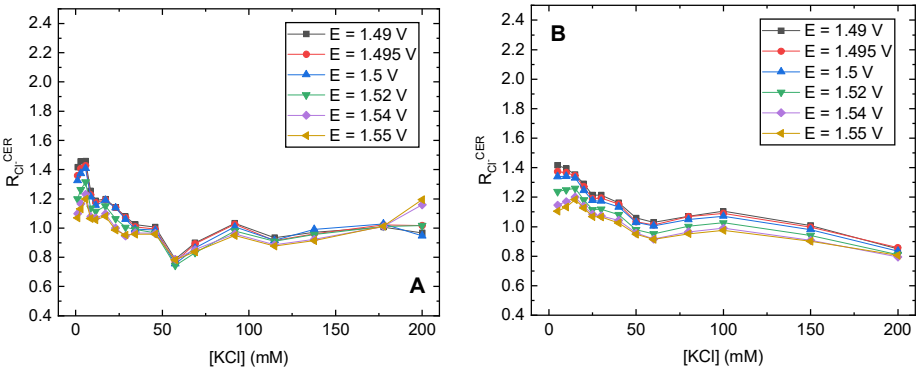

Figure A 9.7.14: CER chloride reaction orders (slopes of log-log plot) versus concentration, derived from an IrO_x/GC sample and a SiO_x/IrO_x/GC sample (A and B respectively). Data is displayed for a series of different potentials.

9.7.3. Supplementary SEM/EDS data

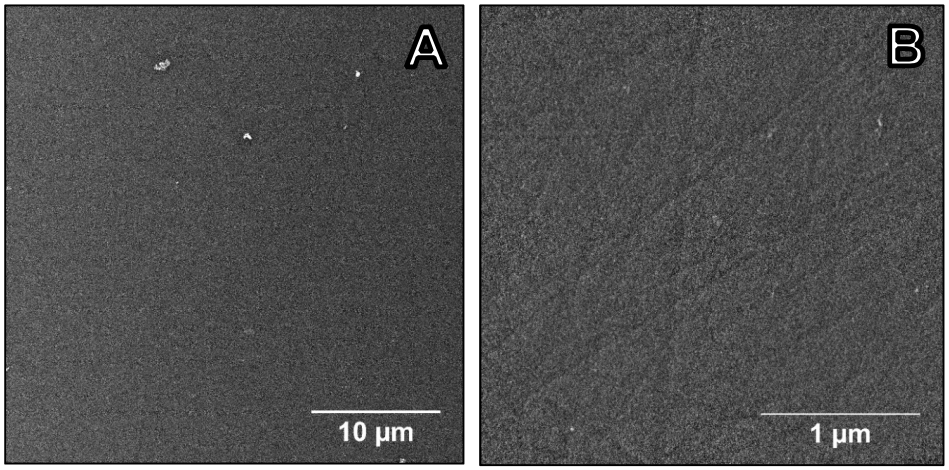

Figure A 9.7.15: SEM micrographs of a SiO_x/Pt/Ti/GC electrode surface (including some minor surface impurities in A).

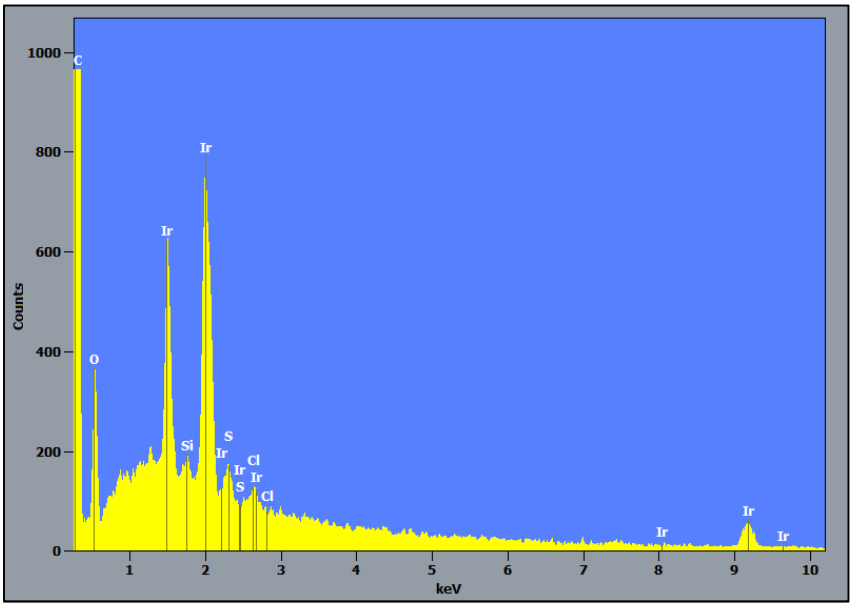

Figure A 9.7.16: EDS spectrum of a SiO_x/IrO_x/GC electrode surface, showing the peaks of commonly detected elements.

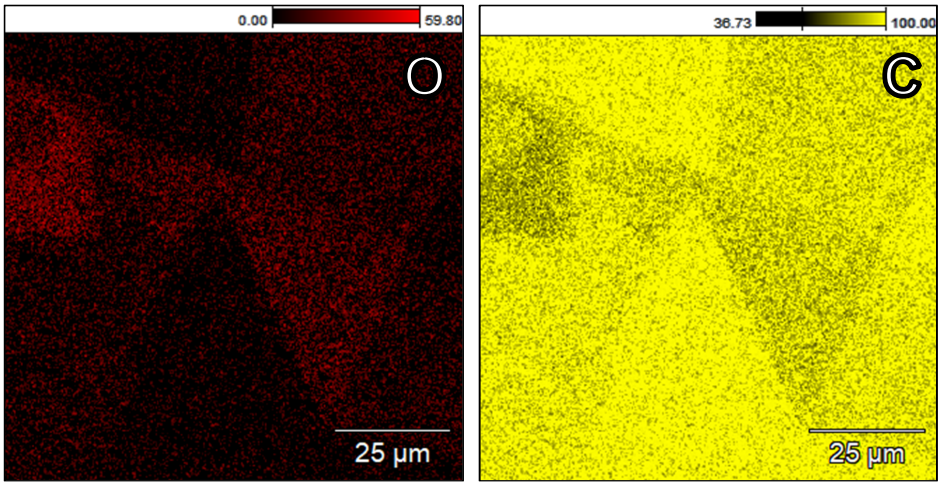

Figure A 9.7.17: Additional EDS elemental maps of O and C, corresponding to the micrograph in Figure 7.5 in the main text. The C signal is present in large amounts and originates from the bulk GC electrode.

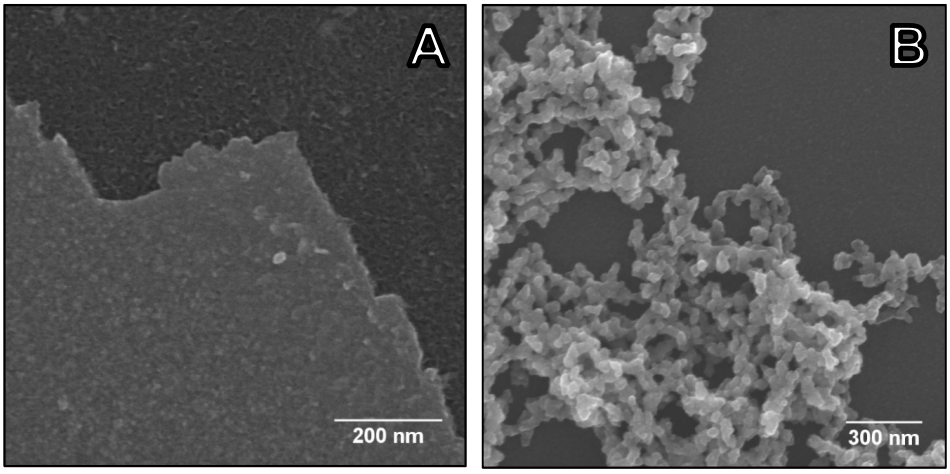

Figure A 9.7.18: Additional SEM electron images of an IrO_x /GC surface, after electrochemical experiments (no SiO_x overlayer present). A: Local edge of the 'smooth' IrO_x layer in light grey color, bottom left. The dark-colored bare GC substrate is visible in the top right. B: Close-up of an IrO_x nanoparticle cluster.

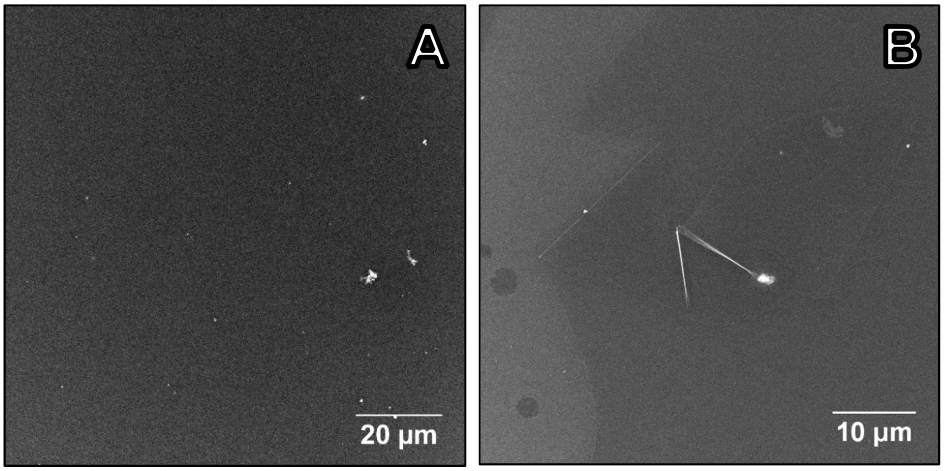

Figure A 9.7.19: Additional SEM electron images of a SiO_x / IrO_x /GC electrode, after electrochemical experiments.

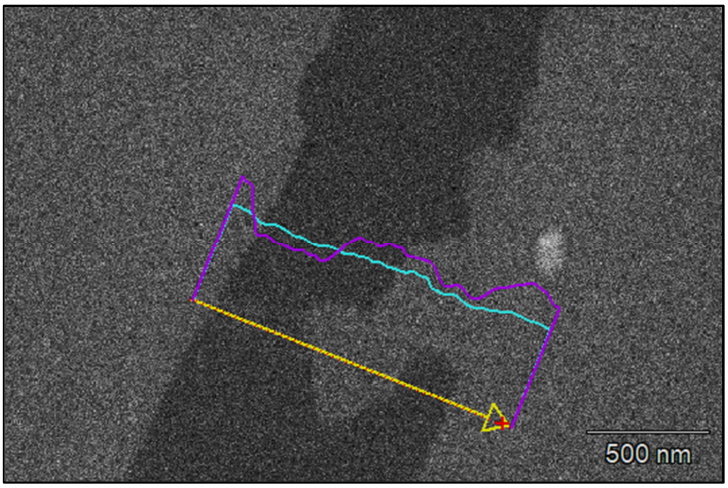

Figure A 9.7.20: SEM/EDS line scan analysis of a SiO_x / IrO_x /GC surface, after electrochemical experiments. Yellow arrows show scan trajectory with corresponding relative counts of Si (cyan) and Ir (purple). Along the scan, one can observe an inhomogeneous Ir distribution (purple) with an even distribution of Si (cyan) on top.

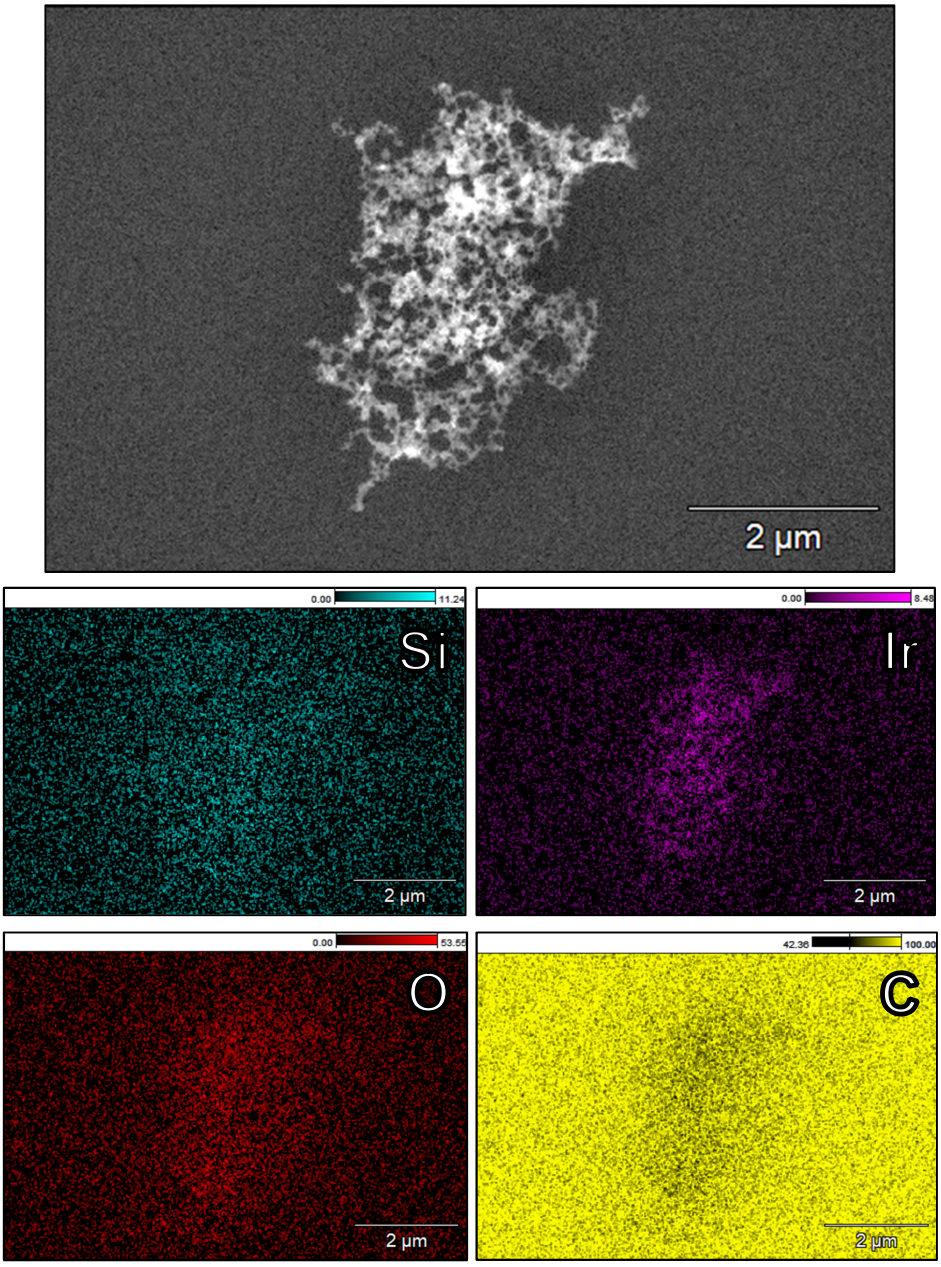

Figure A 9.7.21: Micrograph and EDS elemental mapping of an IrO_x cluster on a SiO_x/IrO_x/GC electrode, after electrochemical experiments.

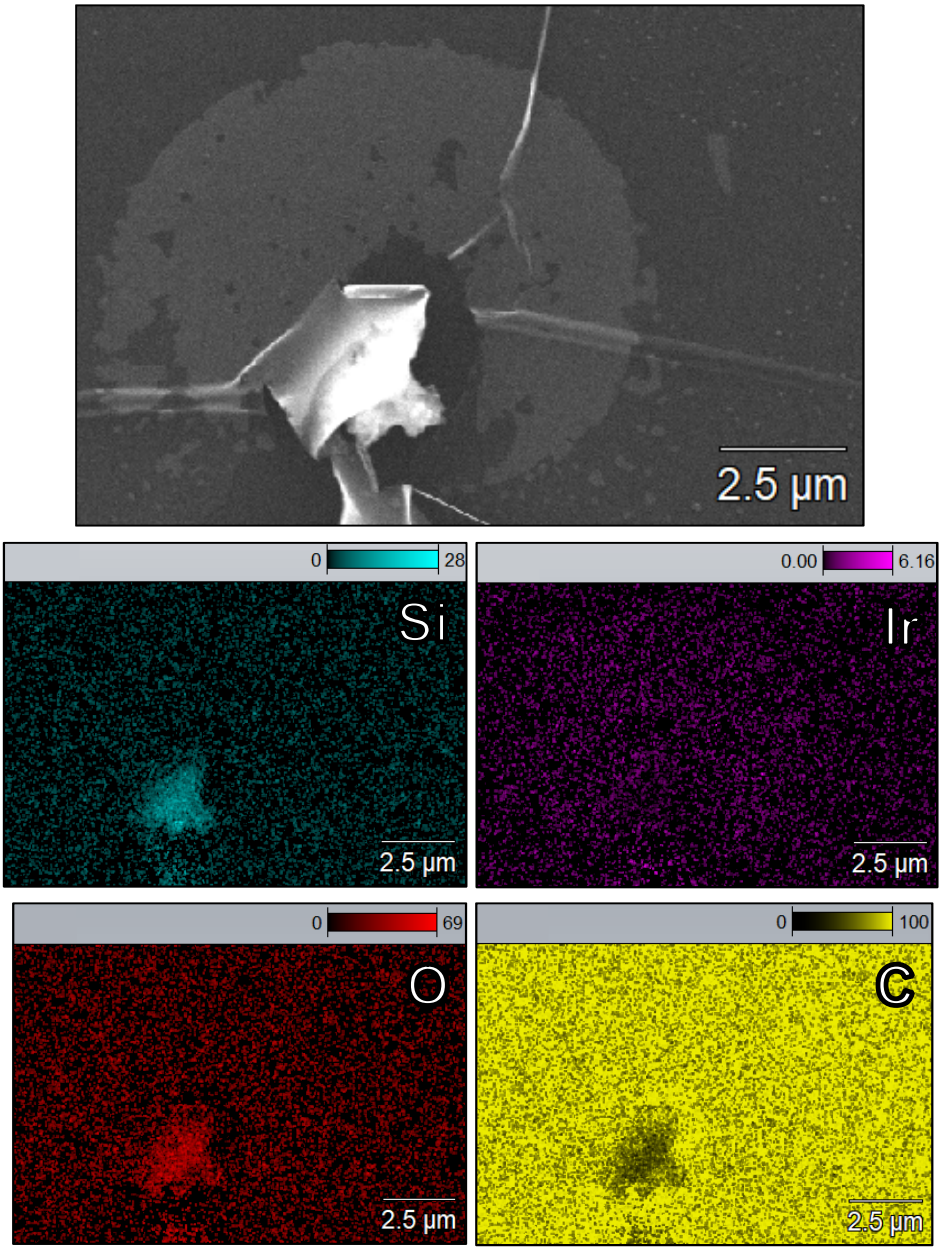

Figure A 9.7.22: Micrograph and EDS elemental mapping of a defect in the SiO_x overlayer on a SiO_x/IrO_x/GC electrode, after electrochemical experiments.

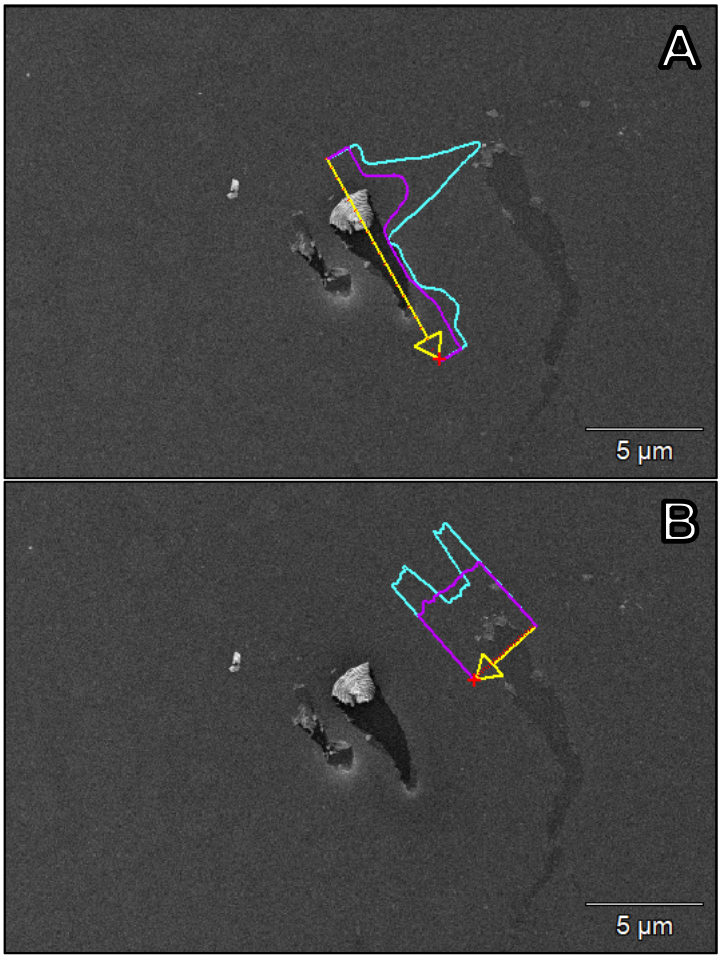

Figure A 9.7.23: SEM/EDS line scan analysis of a SiO_x/IrO_x/GC surface, similar to Figure A 9.7.20. Relative amounts of Si and Ir are show in cyan and purple, respectively. In line scan A, a location is investigated where the combined SiO_x/IrO_x film was damaged. Material has accumulated around the upper area of the scan trajectory, exposing the bare GC underneath. In B, only the SiO_x overlayer was damaged, as suggested by the even Ir distribution.

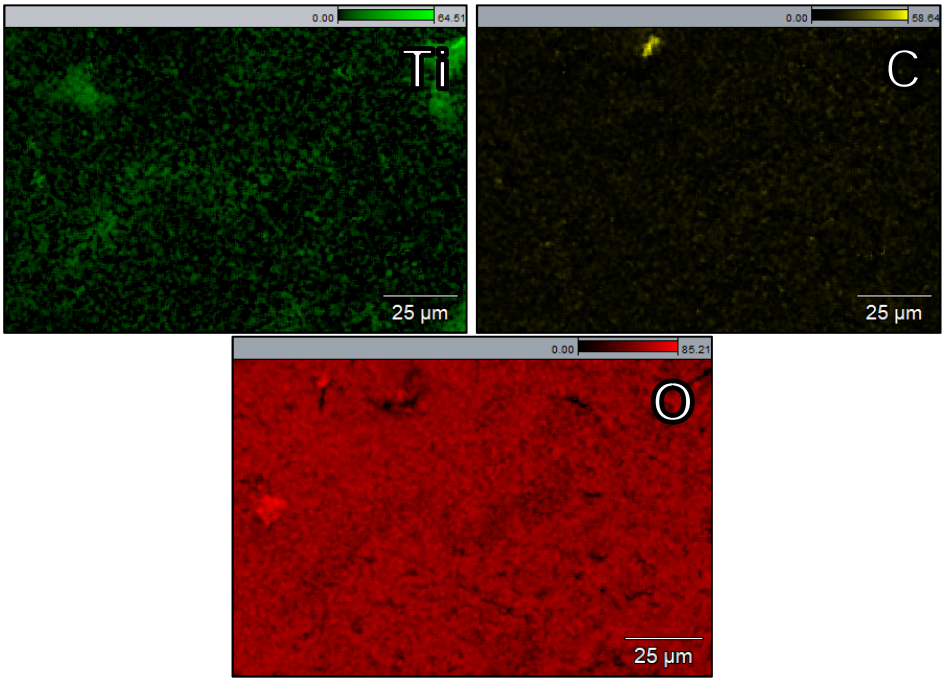

Figure A 9.7.24: Additional EDS elemental maps of Ti, C and O of the micrograph in Figure 7.7 in the main text.

9.8. Supporting information for Chapter 8

9.8.1. Supplementary data and figures

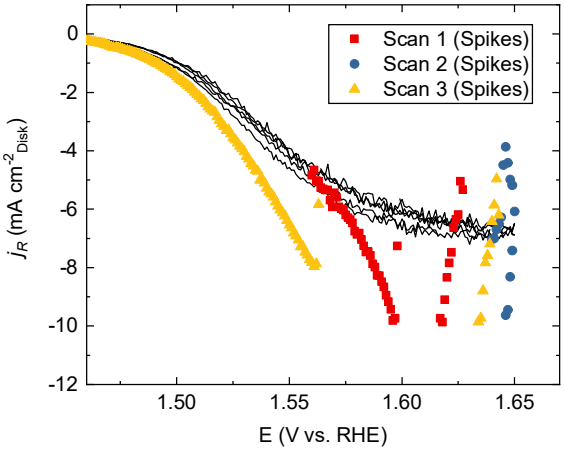

Figure A 9.8.1: Data points from three consecutive scans (red/blue/yellow) omitted from the ring current (black lines) and CER analysis in Figure 8.3.

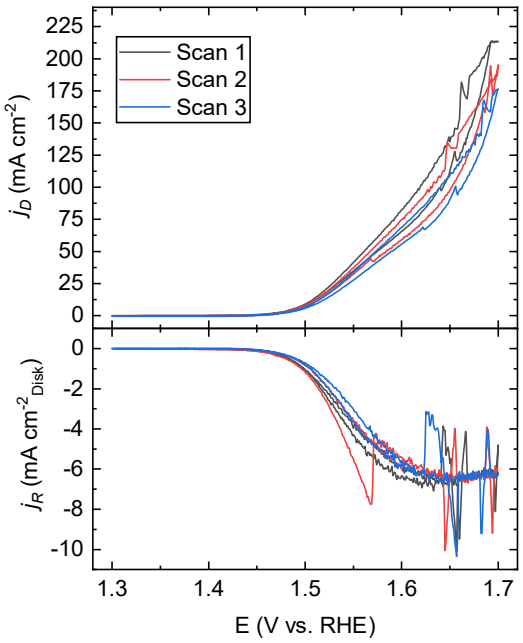

Figure A 9.8.2: RRDE gas evolution experiments under identical conditions as those in Figure 8.3A, but using a potential window extended to 1.70 V vs. RHE.

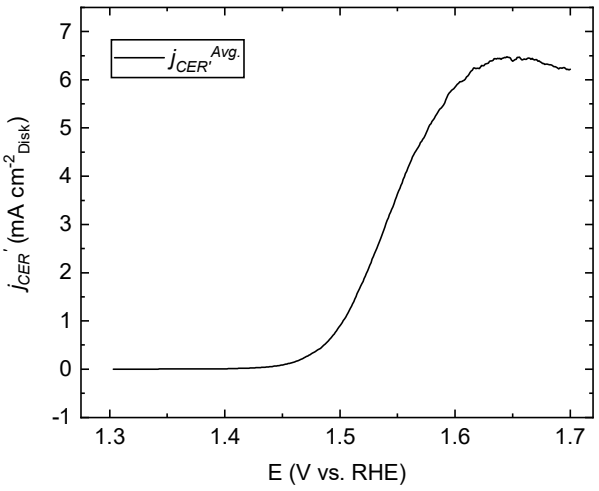

Figure A 9.8.3: Averaged, current spike-corrected forward and backward ring currents from Figure A 9.8.2, representing the CER rates during scanning, such as in the top panel of Figure 8.3.

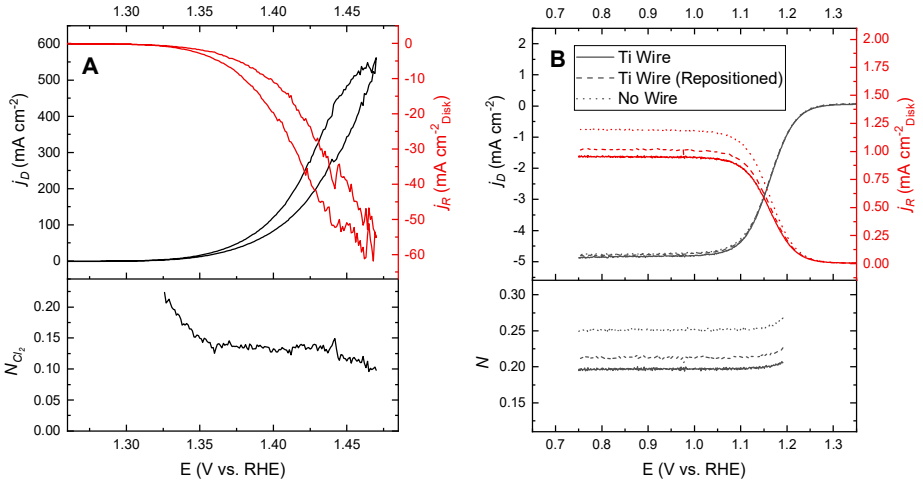

Figure A 9.8.4: Collection experiments on a Pt-Pt RRDE, comparing the collection of gaseous Cl_2 and dissolved $[Fe(CN)_6]^{-4}$ with a Ti wire mounted close to the tip surface. A: Averaged data from five repeated scans in 1 M HCl, such that vigorous Cl_2 evolution occurs on the Pt disk. The Pt ring at 0.95 V was used to detect Cl_2. Top panel shows disk (black trace) and ring current densities (red trace). Bottom panel shows the associated collection efficiency N_{Cl_2}. Scan rate: 10 mV s^{-1}, rotation rate 1500 RPM. B: Experiments involving the collection of $[Fe(CN)_6]^{-4}$. After completion of the CER experiments in A and thoroughly purging the solution to remove all traces of Cl_2, the exact same setup was made alkaline by (carefully) adding the equivalent of 1.1 M KOH. This prevented potentially dangerous situations from exposing $K_3[Fe(CN)_6]$ to strong acid, and served to suppress the HER on Pt while measuring the redox couple. Then, 10 mM $K_3[Fe(CN)_6]$ was added to the + 1 M KCl + 0.1 M KOH solution. This way, the effect of the Ti wire in a specific position could be compared for two different reactions. In the top panel of B, solid trace shows data recorded with the wire positioned in the same way as during experiments in A. Dashed trace shows results after moving the wire slightly further away (several 100 µm) from the tip surface. Dotted trace shows data with the wire removed. Red traces in the upper panel show the corresponding ring current density, black traces in the lower panel show N. Scan rate: 10 mV s^{-1}, rotation rate 1500 RPM.

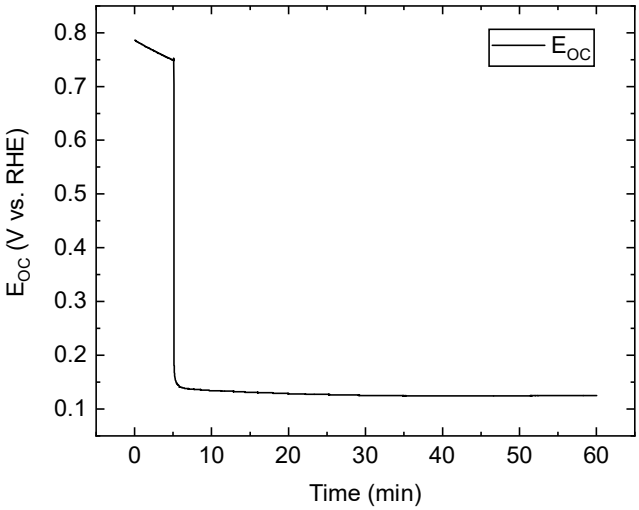

Figure A 9.8.5: Open-circuit potential (E_{OC}) of a Pt disk in a 10 mM NaH_2PO_4 + 10 mM Na_2HPO_4 solution during p-DA deposition, at a rotation rate of 300 RPM. An amount of 2 g/L DA was added to the phosphate buffer around t = 5 min. Solution exposed to air.

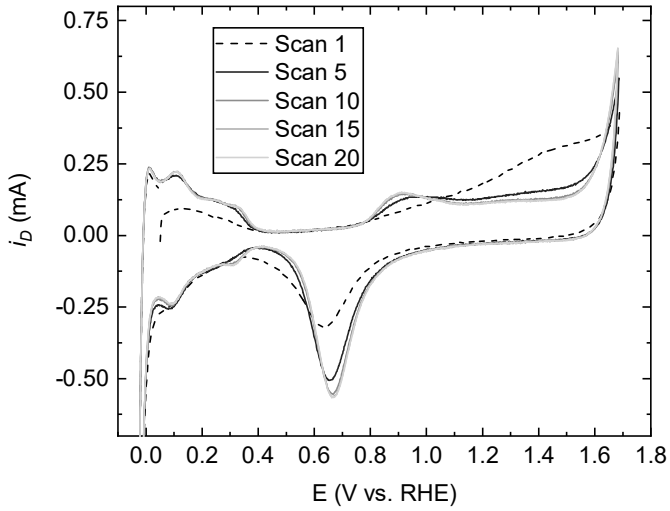

Figure A 9.8.6: Pt disk electropolishing after p-DA deposition on the RRDE tip at 1500 RPM, in a solution of 0.1 M $HClO_4$. Scan rate: 500 mV s^{-1}.